CONTENTS

	Page	
SUMMARY	1	1/A13
INTRODUCTION	2	1/A14
SYMBOLS	4	1/B2
IMPEDANCE TECHNIQUE	6	1/B4
Development of the Equations of Motion	6	1/B4
Analysis of the Titan Data	31	1/D4
Applications to STS Payload	93	2/A11
DISCUSSION OF RESULTS	122	2/C13
CONCLUSIONS	126	2/D3
APPENDICES	127	2/D4
A	127	2/D4
B	131	2/D8
REFERENCES	135	2/D12

JUL 11 1979

NAS 1.26:3143

COMPLETED

NASA Contractor Report 3143

An Impedance Technique for Determining Low-Frequency Payload Environments

Kenneth R. Payne

CONTRACT NAS1-14370
JUNE 1979

NASA

147

NASA Contractor Report 3143

An Impedance Technique for Determining Low-Frequency Payload Environments

Kenneth R. Payne
Martin Marietta Corporation
Denver, Colorado

Prepared for
Langley Research Center
under Contract NAS1-14370

National Aeronautics
and Space Administration

Scientific and Technical
Information Branch

1979

BLANK PAGE

CONTENTS

	Page
SUMMARY	1
INTRODUCTION	2
SYMBOLS	4
IMPEDANCE TECHNIQUE	6
Development of the Equations of Motion	6
Analysis of the Titan Data	31
Applications to STS Payload	93
DISCUSSION OF RESULTS	122
CONCLUSIONS	126
APPENDICES	127
A	127
B	131
REFERENCES	135

LIST OF FIGURES

Figure No.		Page
1	Schematic of Typical Payload/Booster System Showing Pertinent Accelerations and Loads	10
2	Schematic of Impedance Technique for Replacing One Payload Feedback with Another	16
3	Schematic of Three Mass Check Model	19
4	Decaying Sine Forcing Function with no Steady State	22
5	Decaying Sine Forcing Function with Steady State	23
6	Spectral Response of Mass No. 2 to Decaying Sine with no Steady State	25
7	Time Domain Comparisons of Impedance Technique Responses and Time Domain Responses to Decaying Sine with no Steady State	26
8	Fourier Spectrum of Response to Decaying Sine with Steady State but no Tukey Window	27
9	Fourier Spectrum of Response to Decaying Sine Steady State with a Tukey Window	28
10	Time Domain Comparisons of Impedance and Time Domain Solutions Without a Tukey Window	29
11	Time Domain Comparisons of Impedance and Time Domain Solutions With a Tukey Window	30
12	Titan/Centaur Configuration	32
13	Pressure Time History for TP3015 from E-1 Stage I Burnout with Front and End Ramps	34
14	Pressure Time History for TP3016 from E-1 Stage I Burnout with Front and End Ramps	35
15	Acceleration Time History for CM101A from E-1 Stage I Burnout with Front and End Ramps	36

Figure No.		Page

16 Pressure Time History for TP3015 from E-2 Stage I Burnout with Front and End Ramps 37

17 Pressure Time History for TP3016 from E-2 Stage I Burnout with Front and End Ramps 38

18 Acceleration Time History for CM101A from E-2 Stage I Burnout with Front and End Ramps . . . 39

19 Pressure Time History for TP3015 from E-3 Stage I Burnout with Front and End Ramps 40

20 Pressure Time History for TP3016 from E-3 Stage I Burnout with Front and End Ramps 41

21 Acceleration Time History for CM101A from E-3 Stage I Burnout with Front and End Ramps . . . 42

22 Pressure Time History for TP3015 from E-4 Stage I Burnout with Front and End Ramps 43

23 Pressure Time History for TP3016 from E-4 Stage I Burnout with Front and End Ramps 44

24 Acceleration Time History for CM101A from E-4 Stage I Burnout with Front and End Ramps . . . 45

25 Fourier Spectrum of TP3015 from E-1 Stage I Burnout 46

26 Fourier Spectrum of TP3015 from E-1 Stage I Burnout (10-100Hz). 47

27 Fourier Spectrum of TP3016 from E-1 Stage I Burnout 48

28 Fourier Spectrum of TP3016 from E-1 Stage I Burnout (10-100 Hz) 49

29 Fourier Spectrum of CM101A from E-1 Stage I Burnout 50

Figure No.		Page
30	Fourier Spectrum of CM101A from E-1 Stage I Burnout (10-100 Hz)	51
31	Fourier Spectrum of TP3015 from E-2 Stage I Burnout	52
32	Fourier Spectrum of TP3015 from E-2 Stage I Burnout (10-100 Hz)	53
33	Fourier Spectrum of TP3016 from E-2 Stage I Burnout	54
34	Fourier Spectrum of TP3016 from E-2 Stage I Burnout (10-100 Hz)	55
35	Fourier Spectrum of CM101A from E-2 Stage I Burnout	56
36	Fourier Spectrum of CM101A from E-2 Stage I Burnout (10-100 Hz)	57
37	Fourier Spectrum of TP3015 from E-3 Stage I Burnout	58
38	Fourier Spectrum of TP3015 from E-3 Stage I Burnout (10-100 Hz)	59
39	Fourier Spectrum of TP3016 from E-3 Stage I Burnout	60
40	Fourier Spectrum of TP3016 from E-3 Stage I Burnout	61
41	Fourier Spectrum of CM101A from E-3 Stage I Burnout	62
42	Fourier Spectrum of CM101A from E-3 Stage I Burnout (10-100 Hz)	63
43	Fourier Spectrum of TP3015 from E-4 Stage I Burnout	64

Figure No.		Page
44	Fourier Spectrum of TP3015 from E-4 Stage I Burnout (10-100 Hz)	65
45	Fourier Spectrum of TP3016 from E-4 Stage I Burnout	66
46	Fourier Spectrum of TP3016 from E-4 Stage I Burnout (10-100 Hz)	67
47	Fourier Spectrum of CM101A from E-4 Stage I Burnout	68
48	Fourier Spectrum of CM101A from E-4 Stage I Burnout (10-100 Hz)	69
49	Titan Modal Damping Curve	78
50	Longitudinal Payload Impedance for VDS	80
51	Longitudinal Payload Impedance for Helios	81
52	Longitudinal Payload Impedance for Viking A	82
53	Longitudinal Payload Impedance for Viking B	83
54	Comparison of CM101A Flight Data Spectrum with Impedance Analytical Predictions for E-1 Stage I Burnout	85
55	Comparison of CM101A Flight Data Spectrum with Impedance Analytical Predictions for E-2 Stage I Burnout	86
56	Comparison of CM101A Flight Data Spectrum with Impedance Analytical Prediction for E-3 Stage I Burnout	87
57	Comparison of CM101A Flight Data Spectrum with Impedance Analytical Predictions for E-4 Stage I Burnout	88

Figure No.		Page
58	Comparison of CM101A E-1 Spectrum with Impedance Ratio Response from E-2	90
59	Comparison of CM101A E-3 Spectrum with Impedance Ratio Response from E-2	91
60	Finite Element Representation of LDEF	94
61	Fourier Spectrum of X Response at Forward Attach Point Right Hand Side for Lift-off	96
62	Fourier Spectrum of Z Response at Forward Attach Point Right Hand Side for Lift-off	97
63	Fourier Spectrum of X Response at Forward Attach Point Left Hand Side for Lift-off	98
64	Fourier Spectrum of Z Response at Forward Attach Point Left Hand Side for Lift-off	99
65	Fourier Spectrum of KEEL Response for Lift-off	100
66	Fourier Spectrum of Aft Z Response for Lift-off	101
67	Response X Forward Attach Right Hand Side for Lift-off	102
68	Response Z Forward Attach Right Hand Side for Lift-off	103
69	Response X Forward Attach Left Hand Side for Lift-off	104
70	Response Z Forward Attach Left Hand Side for Lift-off	105
71	Response at KEEL for Lift-off	106
72	Response Z Aft for Lift-off	107

Figure No.		Page
73	Fourier Spectrum of X Response at Forward Attach Point Right Hand Side for Landing Due to Strut Forces Only	110
74	Fourier Spectrum of Z Response at Forward Attach Point Right Hand Side for Landing Due to Strut Forces Only	111
75	Fourier Spectrum of X Response at Forward Attach Point Left Hand Side for Landing Due to Strut Forces Only	112
76	Fourier Spectrum of Z Response at Forward Attach Point Left Hand Side for Landing Due to Strut Forces Only	113
77	Fourier Spectrum of KEEL Response for Landing Due to Strut Forces Only	114
78	Fourier Spectrum of Aft Z Response for Landing Due to Strut Forces Only	115
79	Response X Forward Attach Right Hand Side for Landing Due to Strut Forces Only	116
80	Response Z Forward Attach Right Hand Side for Landing Due to Strut Forces Only	117
81	Response X Forward Attach Left Hand Side for Landing Due to Strut Forces Only	118
82	Response Z Forward Attach Left Hand Side for Landing Due to Strut Forces Only	119
83	Response at KEEL for Landing Due to Strut Forces Only	120
84	Response Z Aft for Landing Due to Strut Forces Only	121

LIST OF TABLES

Table No.		Page
1	Longitudinal Weight Summary for Booster Stage I Burnout Models	71
2	Lateral Weight Summary for Booster Stage I Burnout Model	72
3	Slosh Weight Summary for Booster Stage I Burnout Models	73
4	Longitudinal Modal Frequencies for Stage I Burnout Booster Models	74
5	Roll Modal Frequencies for Stage I Burnout Models	75
6	Pitch Modal Frequencies for Stage I Burnout Booster Models	76
7	Yaw Modal Frequencies for Stage I Burnout Booster Models	77
8	Comparison of Payload Total Weights and C. G. Locations	84

SUMMARY

The purpose of this study was to investigate an impedance approach for determining low-frequency environments.

The study consisted of four major tasks:

1. development of the equations of motion used in the impedance technique;
2. demonstration of the technique using flight data from Titan launch vehicles;
3. application of the technique to an existing Shuttle payload;
4. development of the criteria and philosophy of the use of the technique for future payloads.

Results indicate that the method investigated is very promising. It gives good results in the frequency domain as an initial output and transformed time domain results are also good. Its use in certain phases of the payload development cycle could substantially reduce both the time and cost required in current payload loads integration cycles.

INTRODUCTION

Analysis of various payload configurations is a very lengthy and expensive task. Extensive individual models of the payload and booster must be mathematically coupled for the final system models and then elaborate time domain response analyses conducted. The task of the analysis integration for all the organizations involved as well as the manpower and schedule devoted to model coupling and loads computations drive these costs skyward. In reusable launch vehicles, payloads are expected to exhibit numerous variations in configurations, combinations, and experiments, and the detailed approach of the past will not be a viable cost-effective technique.

A preferable technique would eliminate the necessity for detailed coupled models as well as the need for an integration task. If possible, the technique would allow the payload organization of designers and dynamicists to generate, with model information from the booster organization, their own payload response and loads predictions.

This study was conducted to determine the feasibility of a new impedance technique for determining payload low frequency environments. By accounting for the dynamic coupling of the payload and booster in the equation of motion in the frequency domain, the analytical effort is diminished by eliminating the final eigensolutions as well as reducing the equations to simple complex transfer function multiplications. In addition, the model requirements of the booster consist of free-free unloaded interface modal characteristics. Therefore, the task of integrating the loads analysis can be accomplished by

obtaining a set of "standard" booster model data and the payload organizations computing their own loads analysis cycles.

The information presented in this report includes results of the use of the impedance technique on Titan flight data as well as predictions of the low frequency environments for a proposed Shuttle payload. The requirements for implementing the impedance technique and it's feasibility are discussed.

SYMBOLS

[C]	discrete damping matrix
DFI	development flight instrumentation
FFT	fast Fourier transform
$\{F_E\}$	external force/torque vectors
{f}	interface force/torque vectors
[I]	unity matrix
[IMP]	complex impedance matrix
j	square root of negative one
[K]	discrete stiffness matrix
LDEF	Long Duration Exposure Facility
LRC	Langley Research Center
[M]	discrete mass matrix
[PADM]	complex point admittance matrix
$[\phi]$	matrix of modal vectors normalized to unity generalized mass
S	Laplace variable
SRB	Solid Rocket Booster
STS	Shuttle Transportation System
SP	Spacelab single pallet
[T]	discrete static reduction matrix

$[TADM]$	complex transfer admittance matrix
λ	input frequency to modal frequency ratio
ω	modal radial frequencies
ζ	damping coefficient
Ω	input radial frequencies
$\{\ddot{q}\}$, $\{\dot{q}\}$, $\{q\}$	discrete motion of a flexible body
$\{\ddot{\xi}\}$, $\{\dot{\xi}\}$, $\{\xi\}$	modal degree of freedom motions of a booster model due to external forces
$\{\ddot{\xi}'\}$, $\{\dot{\xi}'\}$, $\{\xi'\}$	modal degree of freedom motions of a booster model due to interface forces
$\{\ddot{\bar{\xi}}\}$, $\{\dot{\bar{\xi}}\}$, $\{\bar{\xi}\}$	modal degree of freedom motion for a constrained model

Subscripts:

B	booster
E	external
I	interface
IB	booster mode shapes at the interface
i	frequency increment
FB	booster mode shapes at the external force points
fb	booster mode shapes at the interface force points
P	payload
1	payload number one
2	payload number two

IMPEDANCE TECHNIQUE

Development of the Equations of Motion

The current direction in analytical technique improvements include efforts in developing low-cost, low frequency (100 Hz and below) payload environment prediction techniques. These improvements are aimed at taking advantage of the reusable or repeated boost vehicle concept. It is hoped that better preductions of the expected payload environments based on previous flight data will eliminate a major portion of the conservatism in payload design and test. Most design or test specifications have unnecessary margin due to uncertainties in these environments. The cost of generating extensive response analyses necessary to define the environments fully are becoming prohibitive as well as still containing a few areas of concern with respect to true vehicle excitation. Not all future payloads will be extremely concerned with extensive loads analyses. Depending on the weight margins involved, large margins of safety could be used in some payload designs to insure payload survivability. Primary and/or secondary structure in these "light-weight" payloads can be stiffened to force the payload modes above the areas of maximum gain in the booster transfer characteristics. Areas of concern in the coupled response to vehicle dynamics can be analyzed with large margins of safety in design to cover uncertainties.

It is expected, however, that there will still be payloads that can be classified as weight critical. These payloads must be designed with a goal of optimizing the size of structural members with a desired result of demonstrating with analysis and/or test the smallest acceptable design margin. Payload

loads analysis of this category generally go through approximately three phases of analysis. Preliminary loads are calculated for initial sizing of members. The next two phases are iterative on the design since the analysis lags the detailed member design. Considering the magnitude of analyses necessary for weight critical payloads as well as the number of launch and/or landing events required to be considered, it is evident that any technique shown to be able to reduce analysis cost could have a major impact on design costs.

Standard techniques used for integrated loads analyses include tasks of compiling and coupling the math models from all the organizations having primary structural responsibilities. For example, in the case of a Titan III-E launch analysis, this coupling requires data from at least three organizations: two boost vehicles and a payload. A majority of the cost associated with this procedure lies in two categories. Large expenditures are necessary to:

1. coordinate information necessary for the analysis; and
2. create the coupled models and perform the required loads predictions.

The magnitude of these efforts is probably most evident when late program design changes are necessary. Too often at this point projects have expended analytical apportioned budgets and it becomes either a guessing game of what impact the design change has, or the project is forced into a late program costly test series.

The analytical approach studied in this contract is called an impedance technique because it deals with frequency domain analysis. The objectives considered when developing the technique were based on three major points:

1. a desire to take advantage of standardization of boost vehicles in low frequency environment prediction;
2. a preference for spectral analysis to gain insight into the frequency content of the environment; and
3. a requirement for cost reduction in the areas of analysis and model integration using a comprehensive payload user's guide.

These original objectives were based on the assumption that flight data from previous flights, sufficiently describing the low frequency environments during those flights, would be available and could be used to predict the low frequency environments for the following flights. This method relies on the ability to extract the feedback characteristics of the previous payload and add the effects of the payload of interest, with the assumption that the booster transfer characteristics don't change. With previous flight data and the developed impedance technique, payload designers can eliminate cost by not only generating low cost environment predictions but save additional effort by eliminating an enormous integration effort. The desired result of this approach is to rewrite the equations of motion of a physically coupled structural system in such a manner as to be able to isolate the dynamic feedback characteristics of either physical body. When analyzing payload/booster systems, the task involves resolving the coupled system into the equivalent payload and booster. Once the equations have been resolved in this manner, the dynamic feedback of one payload can be easily replaced by another without solving for a new set of coupled eigensolutions.

The key to the approach can be found in the description of the interface forces between the payload and booster. (In the following development, the forces and accelerations referred to

are shown schematically in Figure 1.) The first step is to develop the equations of motion of the booster alone. Consider the interface accelerations for this free-free body $\{\ddot{q}_I\}$, as being the sum of the accelerations due to the external forces, $\{F_E\}$, and those due to the interface forces, $\{f\}$.

Or,

$$\{\ddot{q}_I\} = \{\ddot{q}_I\}_E + \{\ddot{q}_I\}_F \tag{1}$$

By substituting appropriate expressions for the accelerations on the right-hand side of (1), the total interface accelerations will account for both the external forces being transferred through the booster and the dynamic feedback of the payload.

Evaluating the term for the accelerations due to the external forces first, consider the following general equations of motion for the booster with no payload (free-free).

$$[M_B]\{\ddot{q}_B\} + [C_B]\{\dot{q}_B\} + [K_B]\{q_B\} = \{F_E\} \tag{2}$$

This set of discrete coupled equations for the booster can be simplified by modal substitution to yield a set of uncoupled differential equations, or

$$[I]\{\ddot{\xi}_B\} + [2\zeta_B\omega_B]\{\dot{\xi}_B\} + [\omega_B^2]\{\xi_B\} = [\phi_{FB}]^T\{F_E\} \tag{3}$$

To solve the differential equations in (3) in the frequency domain, first assume zero initial conditions and take the Laplace Transform of both sides:

$$([I]S^2 + [2\zeta_B\omega_B]S + [\omega_B^2])\{\xi_B(s)\} = [\phi_{FB}]^T\{F_E(s)\} \tag{4}$$

By taking advantage of diagonal property of the generalized mass, damping and stiffness, equation (4) reduces to

$$[S^2 + 2\zeta_B\omega_B S + \omega_B^2]\{\xi_B(s)\} = [\phi_{FB}]^T\{F_E(s)\} \tag{5}$$

Equation (5) would serve as a start for a displacement transformation, however, one further substitution yields acceleration as a function of the Laplace variable, S.

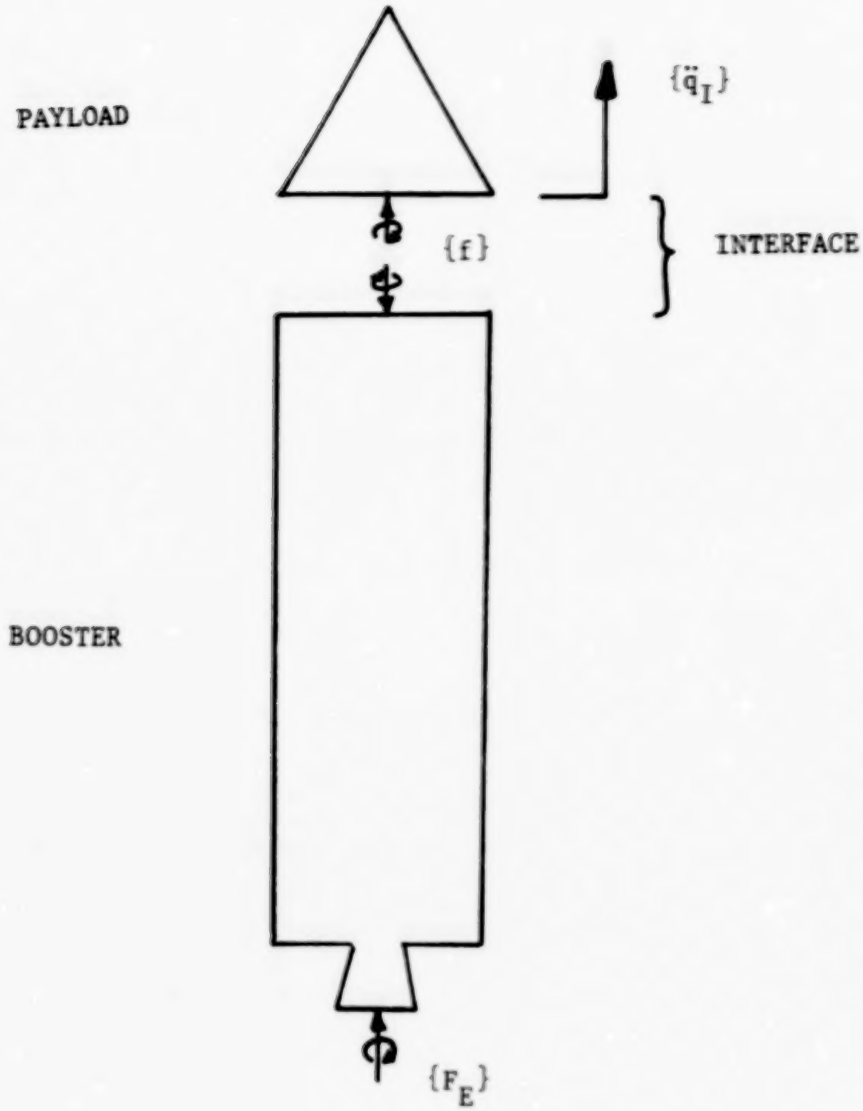

Figure 1. Schematic of Typical Payload/Booster System Showing Pertinent Accelerations and Loads.

$$\left[\frac{S^2 + 2\zeta_B\omega_B S + \omega_B^2}{S^2}\right]\{\ddot{\xi}_B(s)\} = [\phi_{FB}]^T\{F_E(s)\} \tag{6}$$

Or,

$$\{\ddot{\xi}_B(s)\} = \left[\frac{S^2}{S^2 + 2\zeta_B\omega_B S + \omega_B^2}\right][\phi_{FB}]^T\{F_E(s)\} \tag{7}$$

To convert to the frequency domain, now substitute $S = j\Omega$.

$$\{\ddot{\xi}_B\}_i = \left[\frac{-\Omega_i^2}{(\omega_B^2 - \Omega_i^2) + j(2\zeta_B\omega_B\Omega_i)}\right][\phi_{FB}]^T\{F_E\}_i \tag{8}$$

$i = 1,2,3,\ldots$ no. of inputs frequencies

Again substituting,

$$\lambda_i = \Omega_i/\omega_B \tag{9}$$

$i = 1,2,3,\ldots$ no. of input frequencies

Equation (8) becomes

$$\{\ddot{\xi}_B\}_i = \left[\frac{-\lambda_i^2}{(1 - \lambda_i^2) + j(2\zeta_B\lambda_i)}\right][\phi_{FB}]^T\{F_E\}_i \tag{10}$$

$i = 1,2,3,\ldots$ no. of input frequencies

Substituting back to the discrete coordinates expressed in equation (2), the final expression for the interface accelerations, as a function of the input frequency, will be

$$\{\ddot{q}_I\}_{E_i} = [\phi_{IB}]\left[\frac{-\lambda_i^2}{(1 - \lambda_i^2) + j(2\zeta_B\lambda_i)}\right][\phi_{FB}]^T\{F_E\}_i \tag{11}$$

$i = 1,2,3,\ldots$ no. of input frequencies

Or,

$$\{\ddot{q}_I\}_{E_i} = [TADM]_i\{F_E\}_i \tag{12}$$

$i = 1,2,3,\ldots$ no. of input frequencies

The coefficients matrix, $[TADM]_i$, represents the complex transfer admittance from the point of application of the

external forces, e.g. engine thrust time histories, to the interface degrees of freedom accelerations.

Next, to derive the expression for the interface accelerations due to the interface forces, $\{f\}$, a set of differential equations similar to equation (3) can be written as

$$[I]\{\ddot{\xi}_B'\} + [2\zeta_B\omega_B]\{\dot{\xi}_B'\} + [\omega_B^2]\{\xi_B'\} = -[\phi_{fB}]^T\{f\} \tag{13}$$

Here the distinction in the booster modal responses is to separate those from the external forces (equation 10), and those from the interface forces. Following the previous procedure for solving and simplifying the equations of motion, the modal accelerations as a function of input frequency will be

$$\{\ddot{\xi}_B'\}_i = \left[\frac{\lambda_i^2}{(1 - \lambda_i^2) + j(2\zeta_B\lambda_i)}\right][\phi_{fB}]^T\{f\}_i \tag{14}$$

$i = 1,2,3,\ldots$ no. of input frequencies

Then the discrete accelerations at the interface are written as

$$\{\ddot{q}_I\}_{f_i} = [\phi_{IB}]\left[\frac{\lambda_i^2}{(1 - \lambda_i^2) + j(2\zeta_B\lambda_i)}\right][\phi_{fB}]^T\{f\}_i \tag{15}$$

$i = 1,2,3,\ldots$ no. of input frequencies

Or,

$$\{\ddot{q}_I\}_{f_i} = [PADM]_i\{f\}_i \tag{16}$$

$i = 1,2,3,\ldots$ no. of input frequencies

As in equation (12), $[PADM]_i$, is the matrix of coefficients for the complex point admittance for the booster at the interface and is the expression for the acceleration response at the interface due to the interface forces.

Substituting equation (12) and (16) into (1) yields

$$\{\ddot{q}_I\}_i = [TADM]_i\{F_E\}_i + [PADM]_i\{f\}_i \tag{17}$$

$i = 1,2,3,\ldots$ no. of input frequencies

The effect of the payload on these interface accelerations comes through from interface forces, $\{f\}_i$, which in most cases are the reactions to the inertial loads of the payload. With this in mind, the final step in the derivation involves expressing these interface forces in terms of the accelerations of the payload (Figure 1). To accomplish this, consider the equations of motion of the payload (free-free).

$$[M_P]\{\ddot{q}_P\} + [C_P]\{\dot{q}_P\} + [K_P]\{q_P\} = \{f\} \tag{18}$$

In equation (18), the degrees of freedom for the payload include, again, the interface attach point degrees of freedom as well as those for points throughout the structure. The following substitution can be made to write the motions of the payload in terms of the sum of those relative to the interface and the interface motions themselves.

$$\{q_P\} = \{\overline{q}_P\} + [T]\{q_I\} \tag{19}$$

If the substitution is made for modal coordinates then (19) becomes

$$\{q_P\} = [\phi_P]\{\overline{\xi}_P\} + [T]\{q_I\} \tag{20}$$

Limiting for the moment, the constraints of the payload model at the interface to those resulting in a statically determinate interface, the equations of motion from equation (18) can now be shown to be

$$\left[\begin{array}{c|c} I & \phi_P^T M_P T \\ \hline T^T M_P \phi_P & M_I + T^T M_P T \end{array}\right] \begin{Bmatrix} \ddot{\overline{\xi}}_P \\ \ddot{q}_I \end{Bmatrix} + \left[\begin{array}{c|c} 2\zeta_P \omega_P & 0 \\ \hline 0 & 0 \end{array}\right] \begin{Bmatrix} \dot{\overline{\xi}}_P \\ \dot{q}_I \end{Bmatrix}$$

$$+ \left[\begin{array}{c|c} \omega_P^2 & 0 \\ \hline 0 & 0 \end{array}\right] \begin{Bmatrix} \overline{\xi}_P \\ q_I \end{Bmatrix} = \begin{Bmatrix} 0 \\ f \end{Bmatrix} \tag{21}$$

Separating the upper set of equations in (21),

$$[I]\{\ddot{\bar{\xi}}_P\} + [2\zeta_P\omega_P]\{\dot{\bar{\xi}}_P\} + [\omega_P^2]\{\bar{\xi}_P\} = -[\phi_P]^T[M_P][T]\{\ddot{q}_I\} \quad (22)$$

from the lower set,

$$[T]^T[M_P][\phi_P]\{\ddot{\bar{\xi}}_P\} + ([M_I] + [T^T M_P T])\{\ddot{q}_I\} = \{f\} \quad (23)$$

It is obvious that a substitution for the interface forces, $\{f\}_i$, in equation (17) can be obtained.

Taking the Laplace transformation of equation (22) and simplifying as before, we have

$$\{\ddot{\bar{\xi}}_P\}_i = \left[\frac{\lambda_{Pi}^2}{(1-\lambda_{Pi}^2) + j(2\zeta_P\lambda_{Pi})}\right][\phi_P]^T[M_P][T]\{\ddot{q}_I\}_i \quad (24)$$

$i = 1,2,3,\ldots$ no. of input frequencies

Now substituting (24) into (23)

$$\left([T]^T[M_P][\phi_P]\left[\frac{\lambda_{Pi}^2}{(1-\lambda_{Pi}^2) + j(2\zeta_P\lambda_{Pi})}\right][\phi_P]^T[M_P][T] + [M_I] + [T]^T[M_P][T]\right)\{\ddot{q}_I\}_i = \{f\}_i \quad (25)$$

$i = 1,2,3,\ldots$ no. of input frequencies

or

$$[IMP]_i\{\ddot{q}_I\}_i = \{f\}_i \quad (26)$$

$i = 1,2,3,\ldots$ no. of input frequencies

Here, the complex coefficients matrix $[IMP]_i$ represents the impedance or "complex inertia" of the payload at the payload/booster interface.

Now all of the complex transfer function characteristics have been derived that are necessary to fully describe the vehicle coupled response and the final form of the coupled impedance can be generated. Substituting (26) into (17) yields

$$\{\ddot{q}_I\}_i = [TADM]_i\{F_E\}_i + [PADM]_i[IMP]_i\{\ddot{q}_I\}_i \tag{27}$$

$i = 1,2,3,\ldots$ no. of input frequencies

Or, rearranging

$$\left([I] - [PADM]_i[IMP]_i\right)\{\ddot{q}_I\}_i = [TADM]_i\{F_E\}_i \tag{28}$$

$i = 1,2,3,\ldots$ no. of input frequencies

This is now the final form for the impedance equation where the matrix of complex coefficients for the interface accelerations represents the coupled impedance of the payload/booster combination, and the right hand side of (28) represents the complex "psuedo" generalized force. Since the external forces, $\{F_E\}$, are in complex spectral form, and the coefficient matrices are complex as well, the desired spectral interface acceleration can be obtained with equation (28) using nothing more than complex multiplication. This simplicity greatly reduces the cost of generating the low frequency environmental predictions.

If we now consider some new payload for the same booster with the exact same set of external force/torque vectors (Figure 2), then the interface accelerations for the new payload will be

$$\{\ddot{q}_I\}_{2i} = ([I] - [PADM]_i[IMP]_{2i})^{-1}([I] - [PADM]_i[IMP]_{1i})\{\ddot{q}_I\}_{1i} \tag{29}$$

$i = 1,2,3,\ldots$ no. of input frequencies

given the same arrangement of interface tie-down points.

The advantages of analyzing the interface environments in this manner appear to be significant. The resultant set of coefficients for $\{\ddot{q}_I\}_1$ in equation (29) act as a coupled analytical filter that modifies the environment for payload number 1 to arrive at an environment for payload number 2.

BLANK PAGE

BLANK PAGE

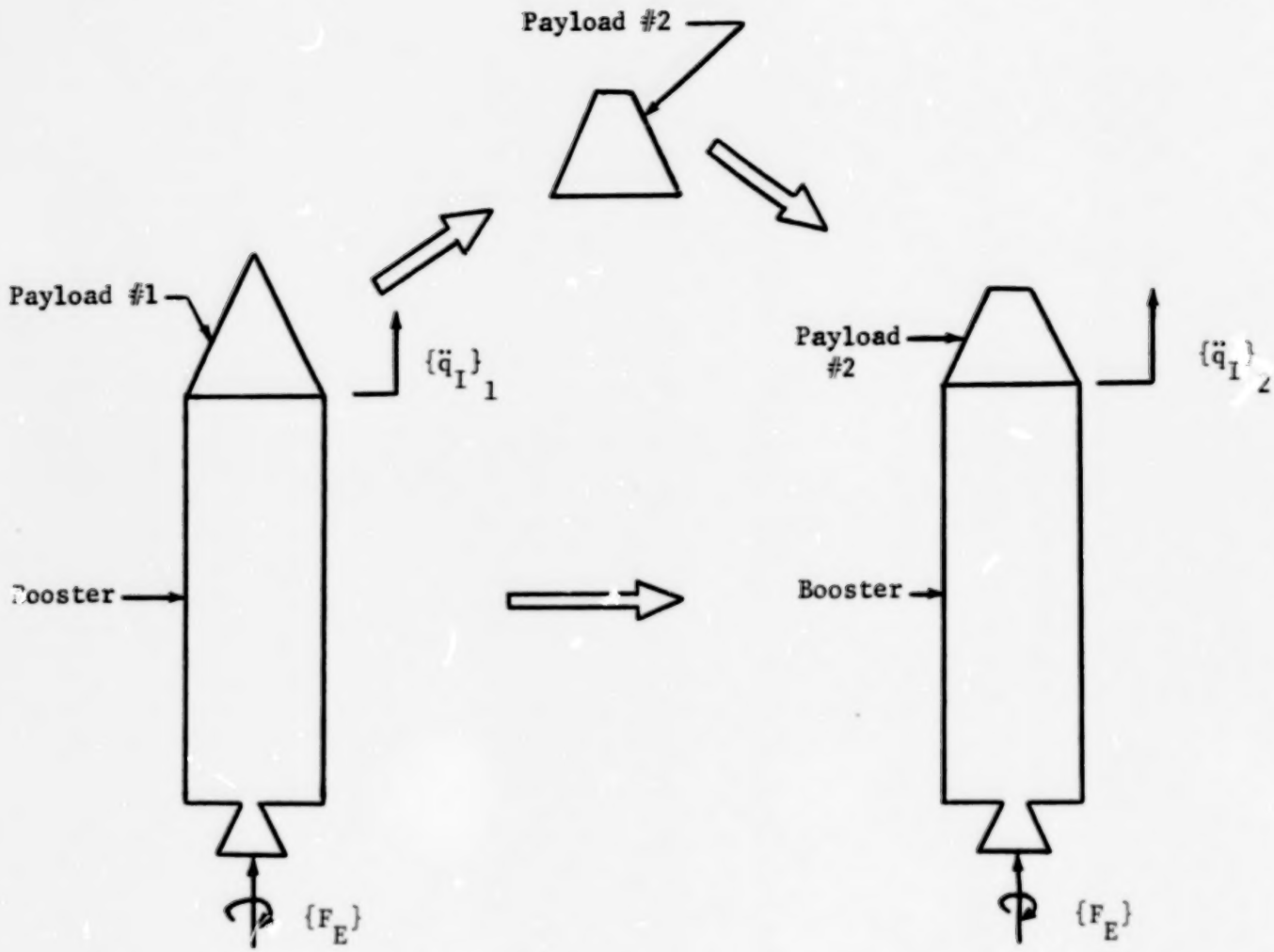

Figure 2. Schematic of Impedance Technique for Replacing One Payload Feedback with Another.

A payload organization could obtain the complex impedance from the proposed data bank that corresponds to the previous interface accelerations and generate new flight predictions for the desired interface. Another possibility could be to synthesize the necessary transfer characteristics from flight data rather than relying solely on analytical model representations. A third possibility is to use equation (29) to evaluate design changes on a particular payload at a particular set of attachment locations. Thus, it appears that either equation (28) or (29) could be utilized to significantly reduce the life-cycle cost of loads analyses.

At this point, a brief review of the limiting assumptions that were used to derive the final equations (28) and (29) is important. In generating the payload impedance characteristics the assumption used was a statically determinate interface. This was done to simplify the complexity of describing the force distributions at the interface. This need not be done, however, for a set of equations similar to (21) can be derived that are somewhat more complex and cumbersome. The velocities and displacements at the interface degrees of freedom must be tracked in this case in order to solve for the interface forces. However, the majority of interface configurations are statically determinate by design, therefore, this study considered only this case.

The assumptions with the most impact on the technique affect the use of equation (29) more than equation (28). Neither are the forcing functions applied to the vehicle exactly repeatable nor are the transfer characteristics the same for all booster configurations. In the case of a booster system like the Shuttle Transportation System (STS), these characteristics change for each location in the Orbiter bay

and for different combinations of payloads in multiple payload flights.

Therefore, the effort during this study was directed primarily at determining the feasibility of a practical use of the technique. Discovery of pitfalls in flight data analysis and assessment of the impact of the assumption made were necessary goals.

To assess the accuracy of the technique, specifically the calculated results of equation (28), time domain response results were compared with those from the impedance technique for a simple system (Figure 3). This evaluation proved beneficial in a number of areas.

The degree of freedom describing the motion of mass M_2 is considered the interface motion for this check case, with the external forces, F_E, applied at M_3.

One discrepancy became apparent from the beginning pertaining to the modal damping. Various techniques have been tried to obtain the correct damping for a modally coupled model. For example, one technique tried on the Viking Program involved calculating the triple matrix product of the coupled set of modes and the uncoupled diagonal damping matrices and discarding the resulting off-diagonal terms to maintain an uncoupled set of equations. This assumption does force the coupled damping to be a function of the coupled modes but throws away, in essence, the coupling effect from mode to mode. The problem lies in the manner in which the damping is measured and assumed for a payload and booster. If the damping is measured for a typical payload in a modal survey, the recorded damping is a function of the boundary conditions, for these set the relative motions for each degree of freedom. When the payload is physically attached to the booster, a new set of

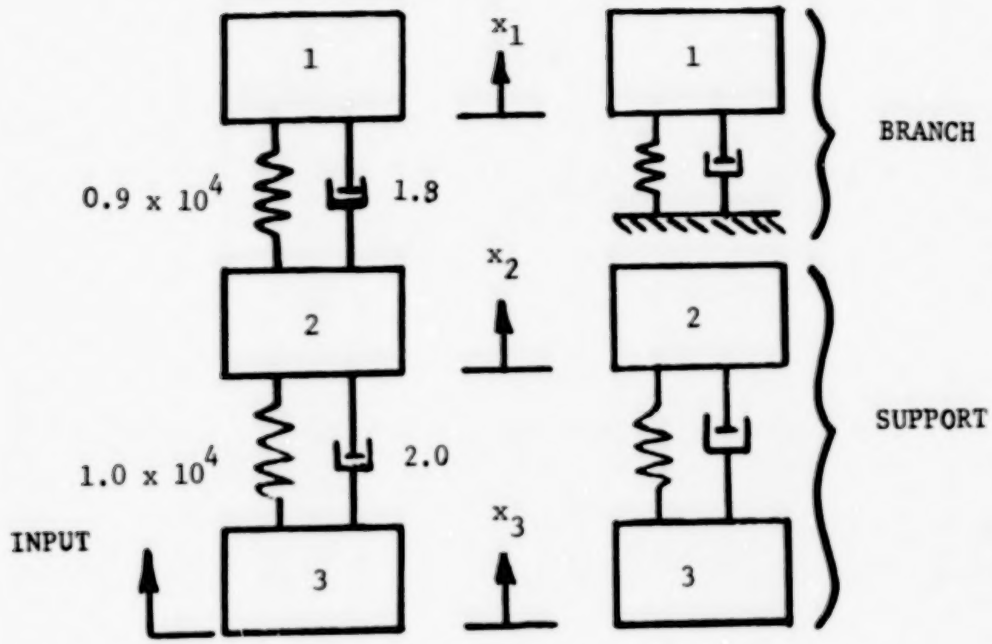

Figure 3. Schematic of Three Mass Check Model

boundary conditions exist and, therefore, a new set of relative motions or mode shapes also exist. For small damping, less than 1%, the previous philosophies about how to generate coupled damping may be adequate for determining payload loads and environments, but the impedance technique, equations (28) and (29), just exemplifies the discrepancy. Since the technique, when accounting for the payload feedback in the equations for the interface acceleration, is merely replacing the need for the coupled eigensolutions, the modal damping used in generating the complex impedance of the payload must be one that will result in the expected coupled analyses. If the impedances are generated assuming 1% damping for all payload and booster modes, for example, and the equivalent coupled model has coupled the damping and discarded all off-diagonal terms, there will be differences in the two transfer functions since some of the resulting diagonals of the coupled damping will be larger than 1%. It should be noted that these large discrepancies due to the damping differences may be evident only in the frequency domain. In the time domain these differences may make only minute errors in the response.

In order to get comparable transfer functions for both the impedance check and the coupled time domain check, the discrete dampings were assumed as shown in Figure 3, thus the transfer functions were the same regardless. This point is important in light of future comparisons of existing loads analysis techniques and those similar to that developed above. There are, however, possible solutions (Reference 1) and the point will not be labored further here.

Use of the Fast Fourier Transform (FFT) in obtaining the spectral data also presents some problems as discovered by experimenting with the sample problem. The FFT is more commonly

used for spectral analysis, e.g., auto-spectral densities, coherence, etc., of random data (References 2 and 3). Certain errors are introduced by signal truncation of time histories. In random data analysis, these errors are usually minimized by taking a number of averages or statistical degrees of freedom (Reference 3). The effects of truncation on transient or complex signals cannot be averaged out since the signals are of finite length and do not repeat themselves. These truncation errors can be significant in generating Fourier spectra, expecially when these spectra are used to drive a system. The system transfer function has a certain value at a certain frequency and thus responds to the input at that frequency regardless of the error of that input.

This problem first manifested itself in the analysis of the Titan data discussed in the following section. A parallel effort with the three mass check case shed some insight on the effects of truncation. For example, two separate force time histories were applied to the model depicted in Figure 3. One force time history consisted of a decaying sine wave shown in Figure 4. The same decaying sine function with a superimposed steady-state value is shown in Figure 5. These two forcing functions characterize one of the most common truncation effects (Reference 4). Figure 4 could represent a lateral force at a payload/booster interface extracted from recorded flight data. Figure 5 could be obtained in a like manner and represent a longitudinal interface load, i.e., in the direction of thrust.

The forcing function shown in Figure 4 was used to drive the 3 mass check model and obtain the acceleration as a function of time for the middle mass at degree of freedom number 2 (see Figure 3). In addition, the Fourier transform of the forcing

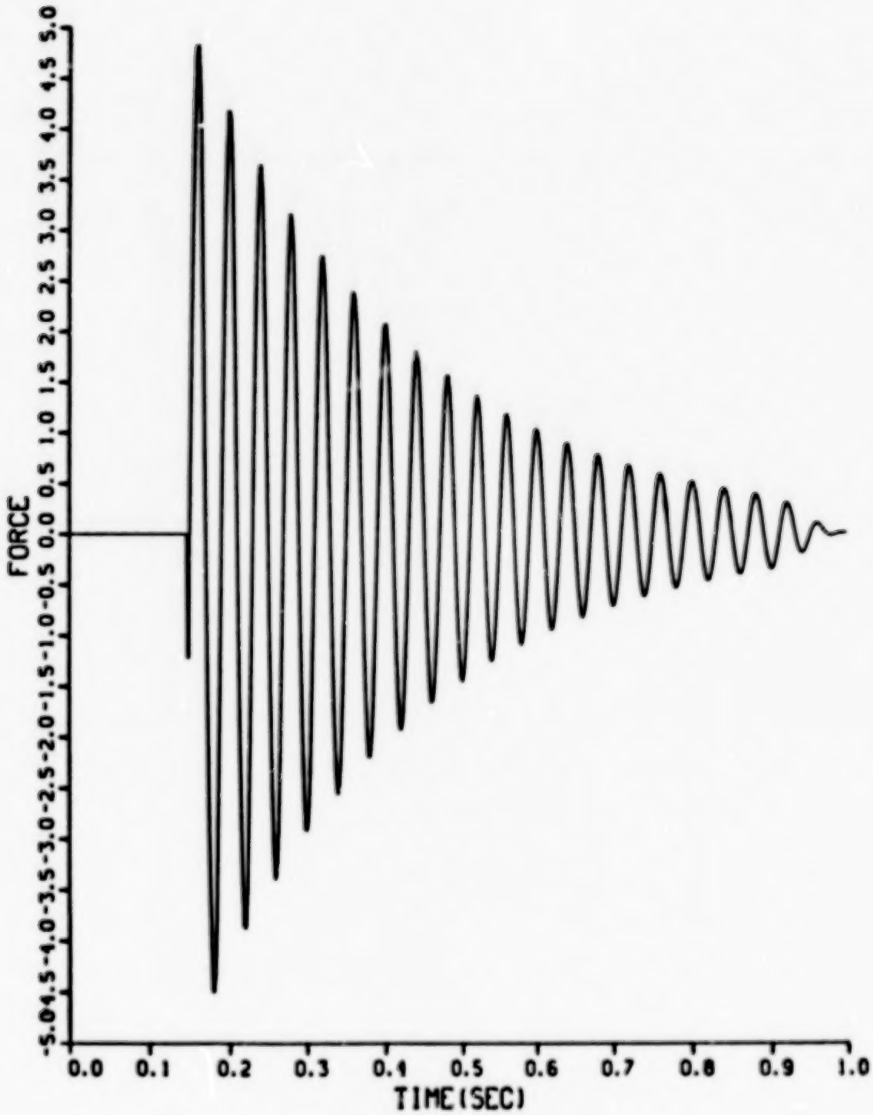

Figure 4. Decaying Sine Forcing Function with no Steady State

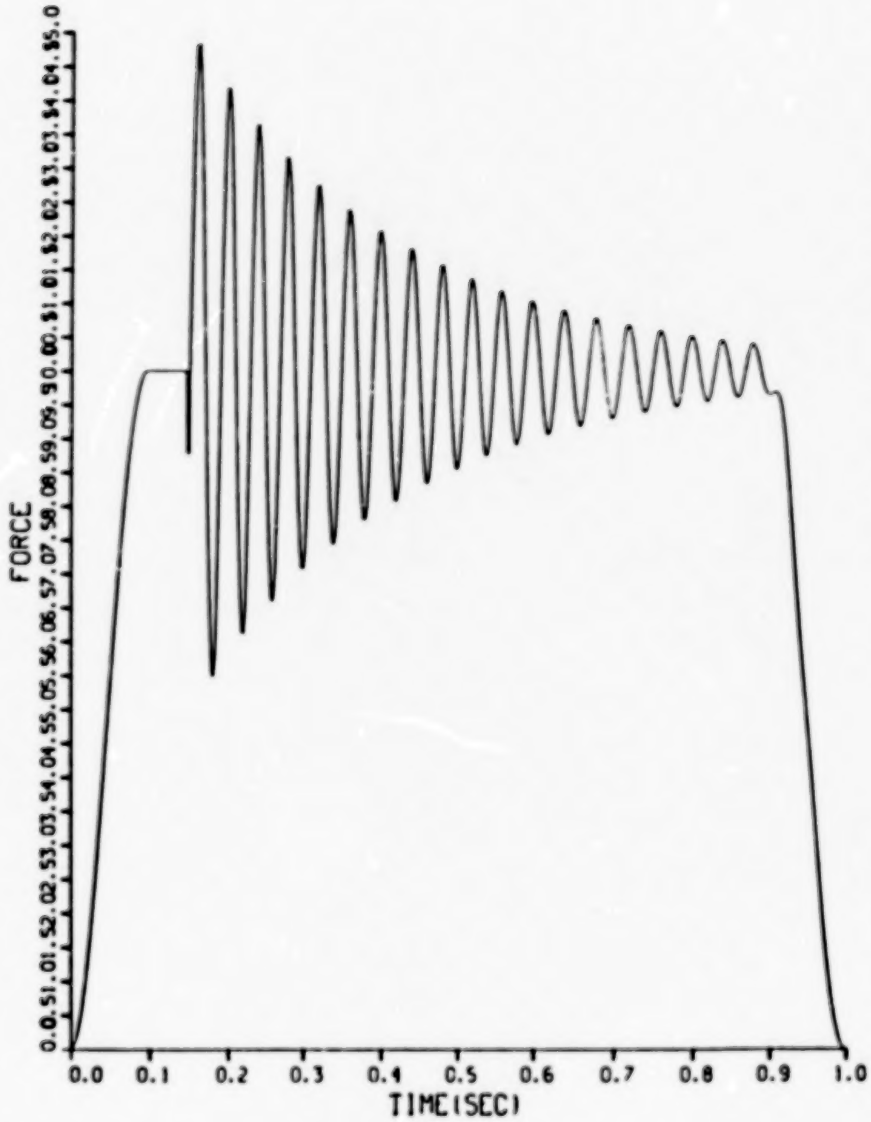

Figure 5. Decaying Sine Forcing Function with Steady State

function in Figure 4 was generated using an FFT after the time history was "windowed" by a Tukey window (Reference 4). Note that the time history in Figure 5 shows the results of the Tukey window application. This Fourier transform was then used to drive the model using equation (28) to calculate the response of degree of freedom number 2. The spectral results of the impedance analysis is shown in Figure 6. But for the true comparison this spectral response was inverse Fourier transformed to obtain a time history to correlate with the time domain response. This correlation is shown in Figure 7.

The effect of the window is shown perhaps more in driving the model in the frequency domain with the force in Figure 5. Figures 8 and 9 show the Fourier spectral response of degree of freedom 2 with and without a Tukey window. Figures 10 and 11 again depict a comparison of both sets of frequency domain response to the time domain response. It is obvious from these plots that for this case the Tukey window improves the response correlations.

It is apparent from the results obtained that the low frequency environments can be predicted with the impedance technique. Better correlation with the time domain solutions could possibly be made with a different window or increasing the frequency resolution, however, enough correlation is apparent to attempt to use the technique for more complicated systems.

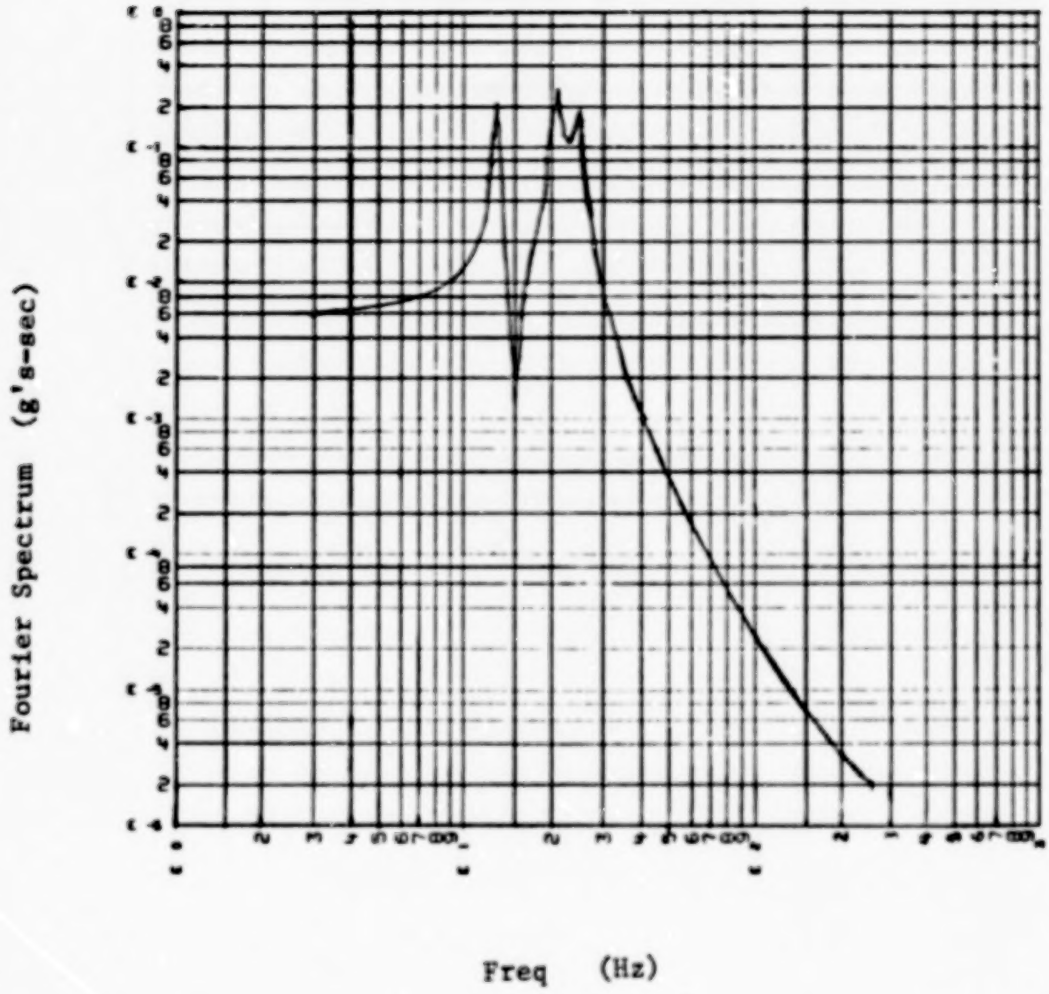

Figure 6. Spectral Response of Mass No. 2 to Decaying Sine with no Steady State.

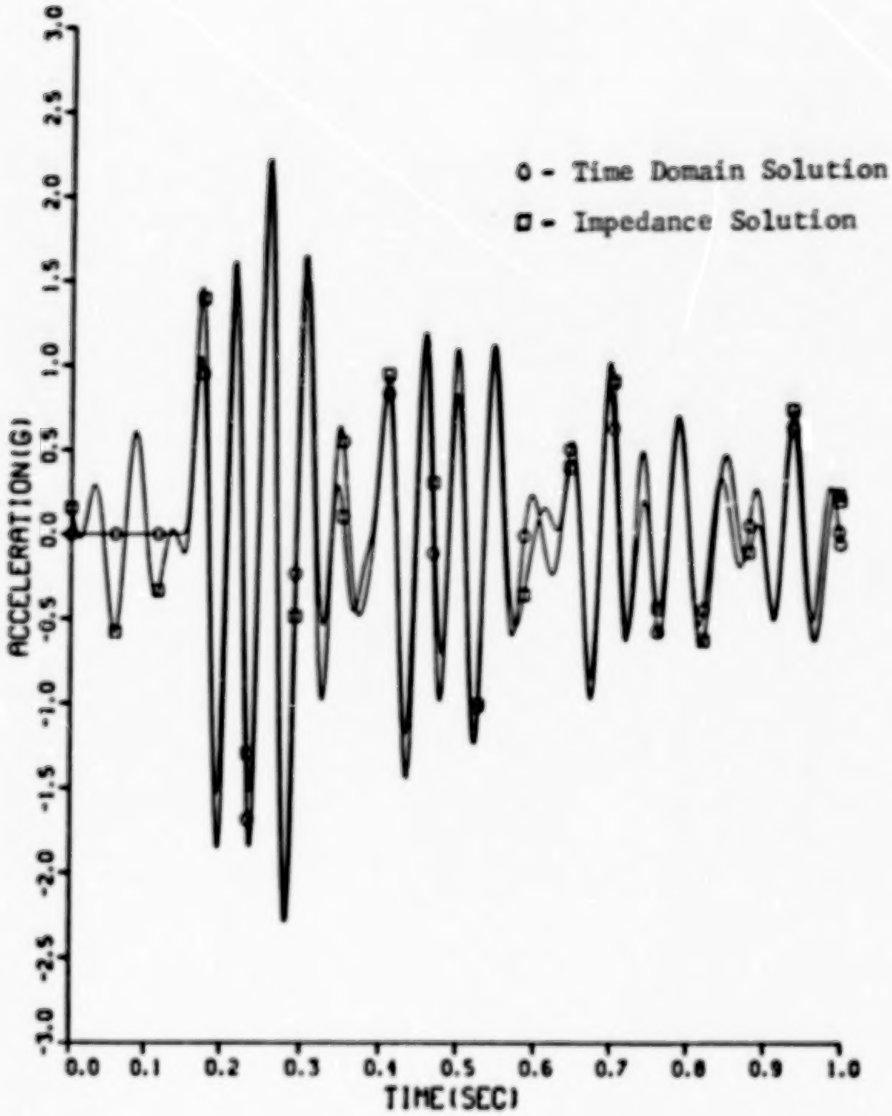

Figure 7. Time Domain Comparisons of Impedance Technique Responses and Time Domain Responses to Decaying Sine with no Steady State.

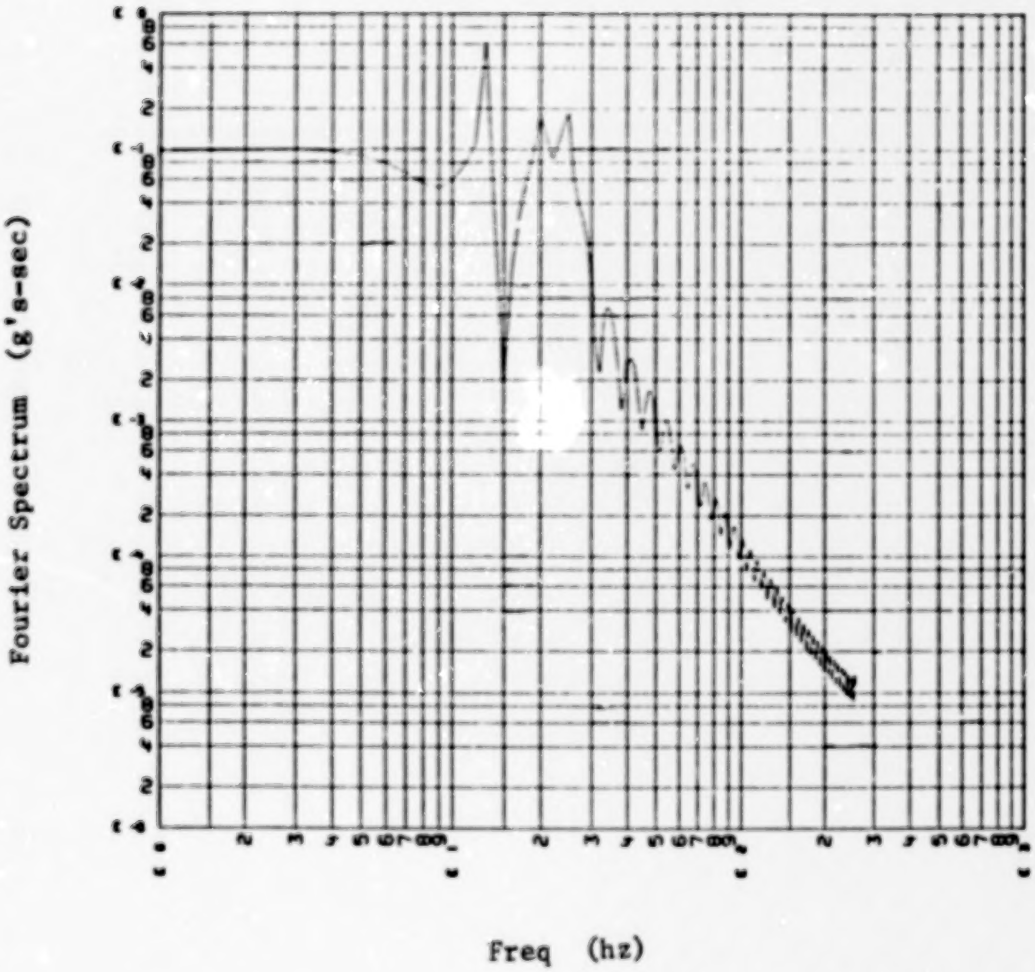

Figure 8. Fourier Spectrum of Response to Decaying Sine with Steady State but no Tukey Window.

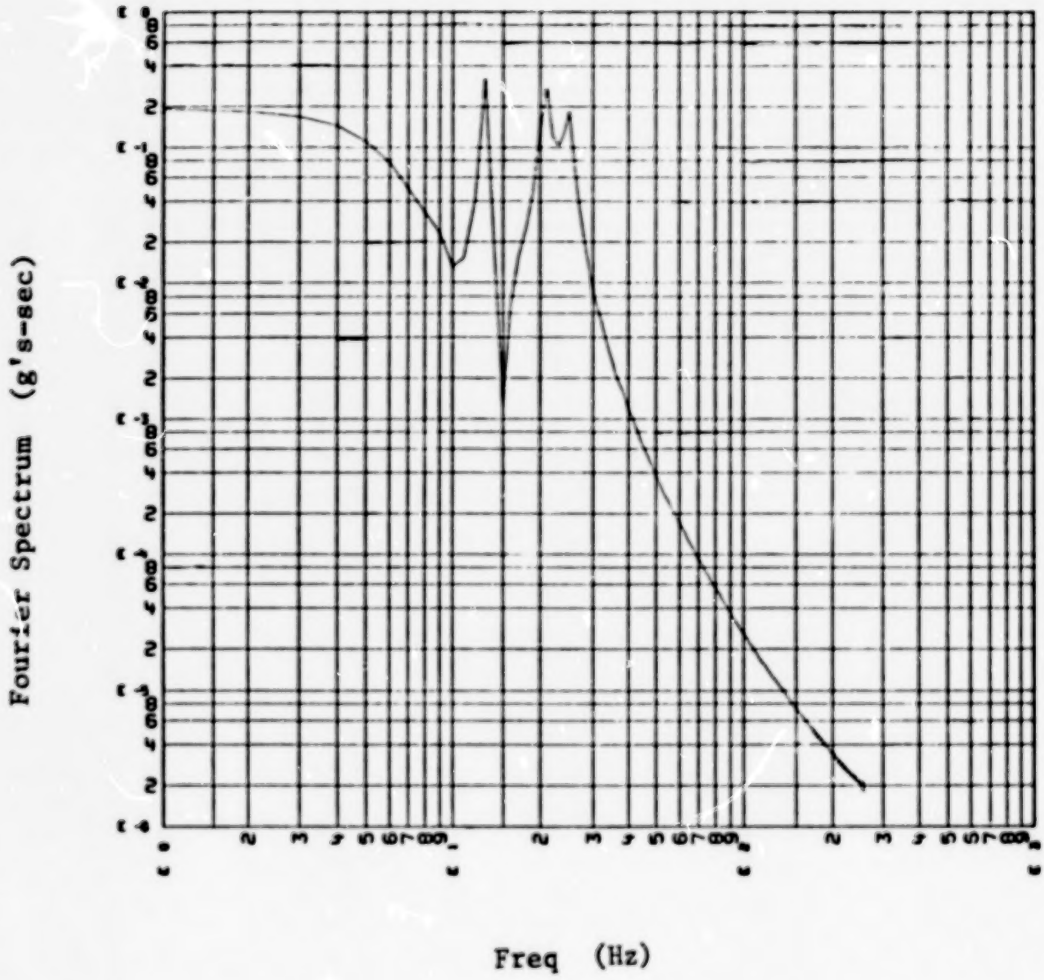

Figure 9. Fourier Spectrum of Response to Decaying Sine with Steady State with a Tukey Window.

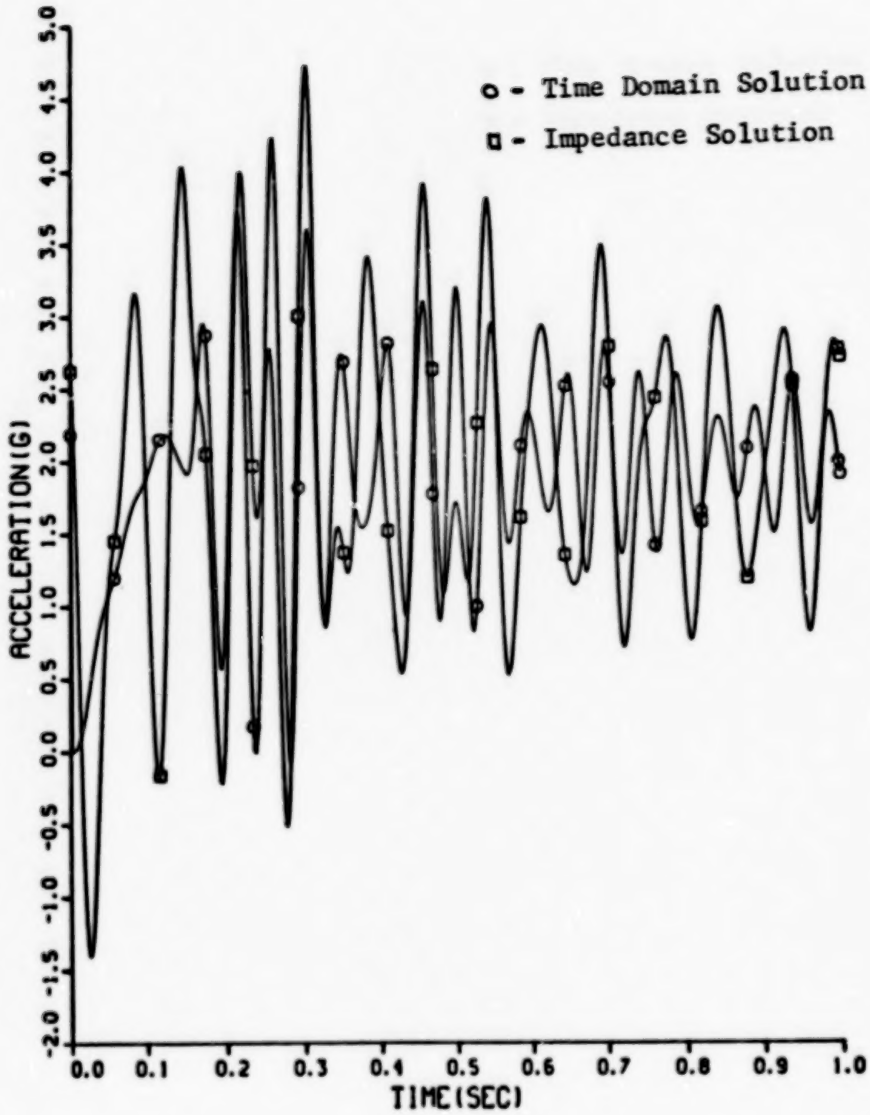

Figure 10. Time Domain Comparisons of Impedance And Time Domain Solutions Without A Tukey Window.

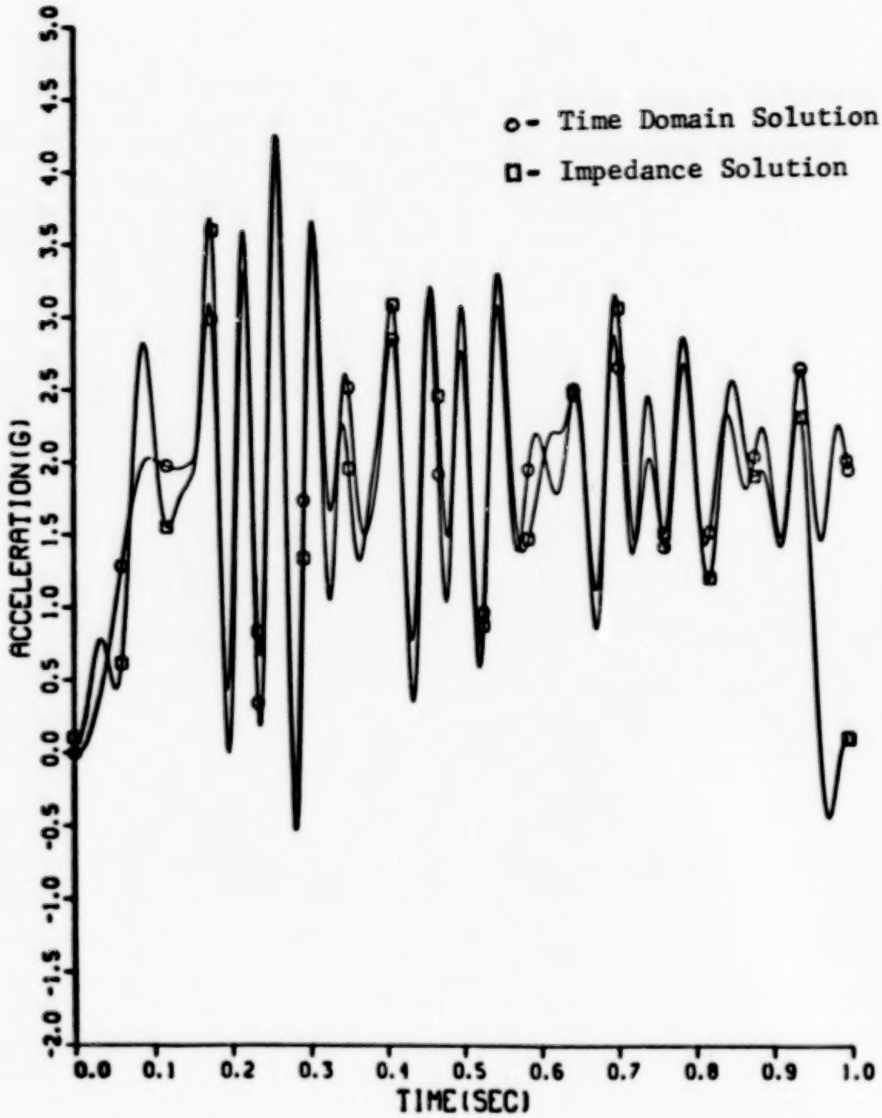

Figure 11. Time Domain Comparisons of Impedance And Time Domain Solutions With A Tukey Window.

Analysis of the Titan Data

The true test of the impedance technique was to analyze real available flight data. The objectives of this evaluation included discovering any pitfalls in the practicality of the overall impedance approach and to identify key items necessary for a payload user's guide.

Available telemetered flight data from the first four Titan Centaur Launch Vehicle flights were digitized for use in this evaluation. Briefly, these flights can be described as follows:

1. E-1 generally consisted of a two stage Titan, solid rocket strap-ons, Centaur upper stage and Dynamic Simulator of the Viking payloads, with shroud;
2. E-2, same as E-1 with a Helios payload; and
3. E-3 and E-4 were the same as described above with Vikings A and B as payloads.

The necessary information for solving the impedance equations (28) and (29) included the external forces for driving the analytical models and interface accelerations for comparison with the results.

All recorded flight data, including the pulse code modulated (PCM) diagnostic data for the boost-vehicle as well as the FM/FM payload data were digitized at four hundred samples per second, and furnished by Langley Research Center. A further description of these flights and telemetered data can be found in Reference 5.

Not all of the digitized data channels were used in this analysis. The transducers that were used measured chamber pressures for Stage I of Titan and acceleration (accelerometer number CM101A) near the Centaur/payload interface in the longitudinal axes (see figure 12). These measurements were

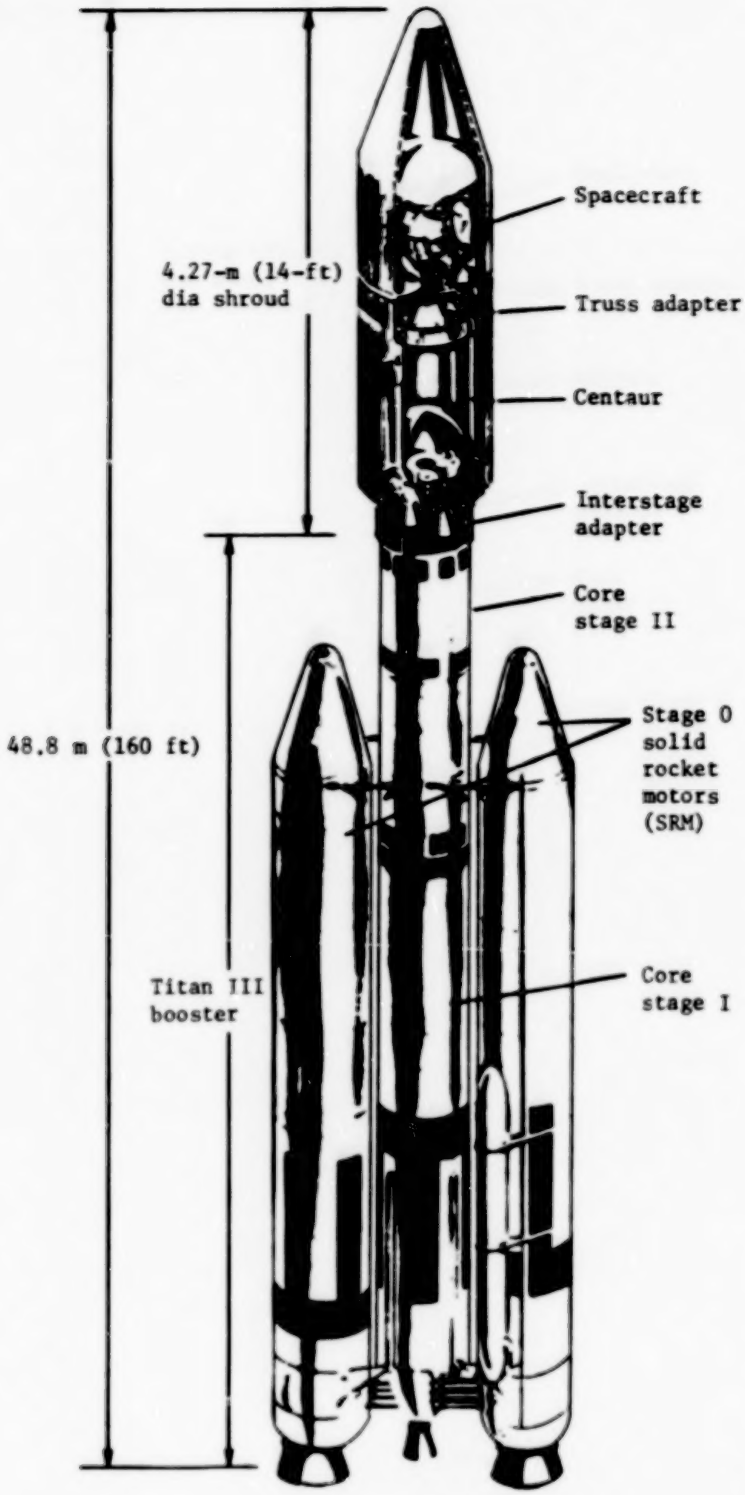

Figure 12. Titan/Centaur Configuration

representative of the applied external forces and interface accelerations for some of the transient events. In that regard, the event chosen for the impedance technique demonstration was the Titan Stage I burnout. This event by definition had fewer externally applied forces than say the liftoff event and it was past the major aerodynamic environments. Thus, the assumption that the engine pressure time histories describe sufficiently the external force/torque vector seems good for this event.

As discussed in the previous section, some data manipulation is necessary for the flight data in order to obtain meaningful spectra. However, the windows discussed were not applied to the Titan data (they were developed later) although a similar technique was used. Linear ramps were multiplied with the data for fixed increments at the beginning and end of each extracted time history. The result was a reduction in the truncation errors much like using a "filter" type window. Figures 13 through 24 show the resulting time histories for engine pressure (denoted by TP sensor numbers) and acceleration for CM101A. The length of the time histories was 5.12 sec which corresponds to 2048 samples at 400 samples per sec. It can be seen in reviewing, say the pressure transducer TP3015, that slight differences exist from one flight versus another in not only amplitude but signature as well, a point which will be discussed in more detail later. Fourier spectra of these signals were calculated using an FFT routine and are shown in Figures 25 through 48. Notice each spectrum is plotted twice, the first showing the spectrum up to the Nyquist frequency 200 Hz, and the second one on one cycle log-log for more visual resolution in the lower frequencies. Here again, reviewing the spectra of any one transducer

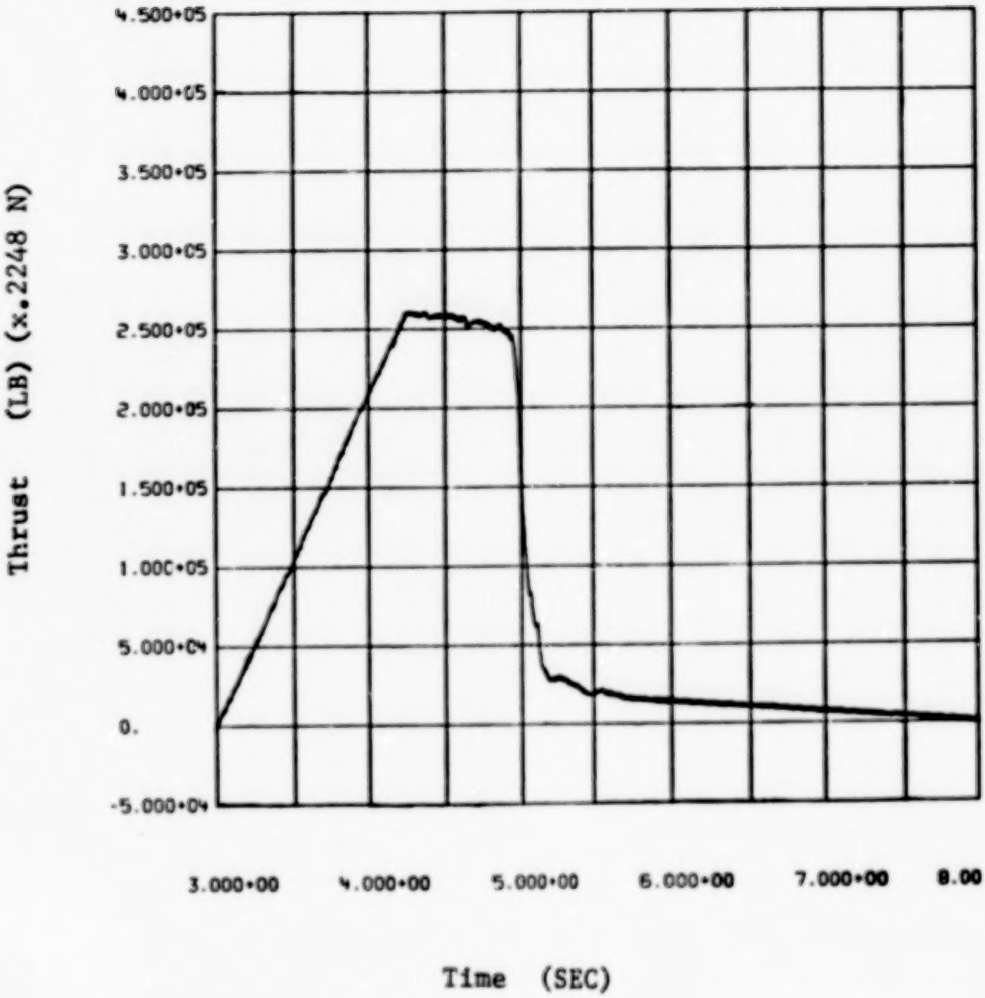

Figure 13. Pressure Time History for TP3015 From E-1 Stage I Burnout With Front and End Ramps

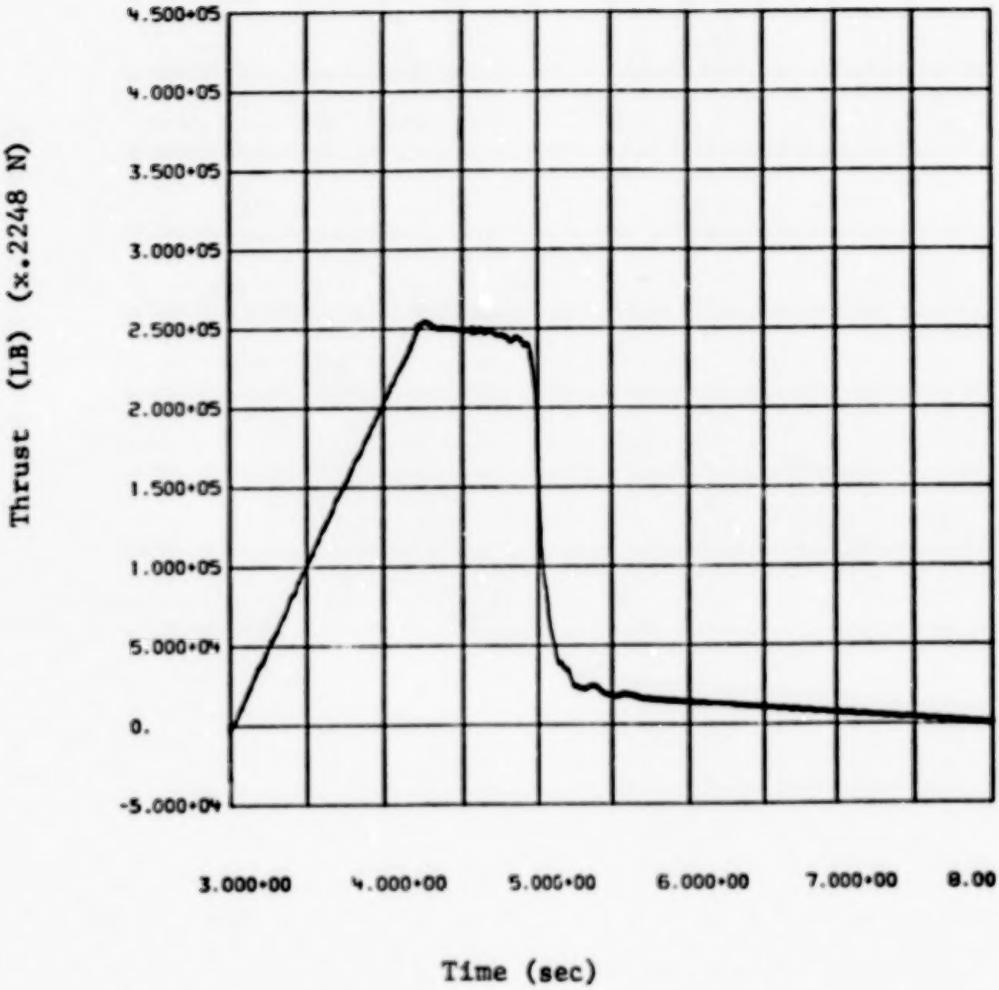

Figure 14. Pressure Time History for TP3016 From E-1 Stage I Burnout With Front and End Ramps

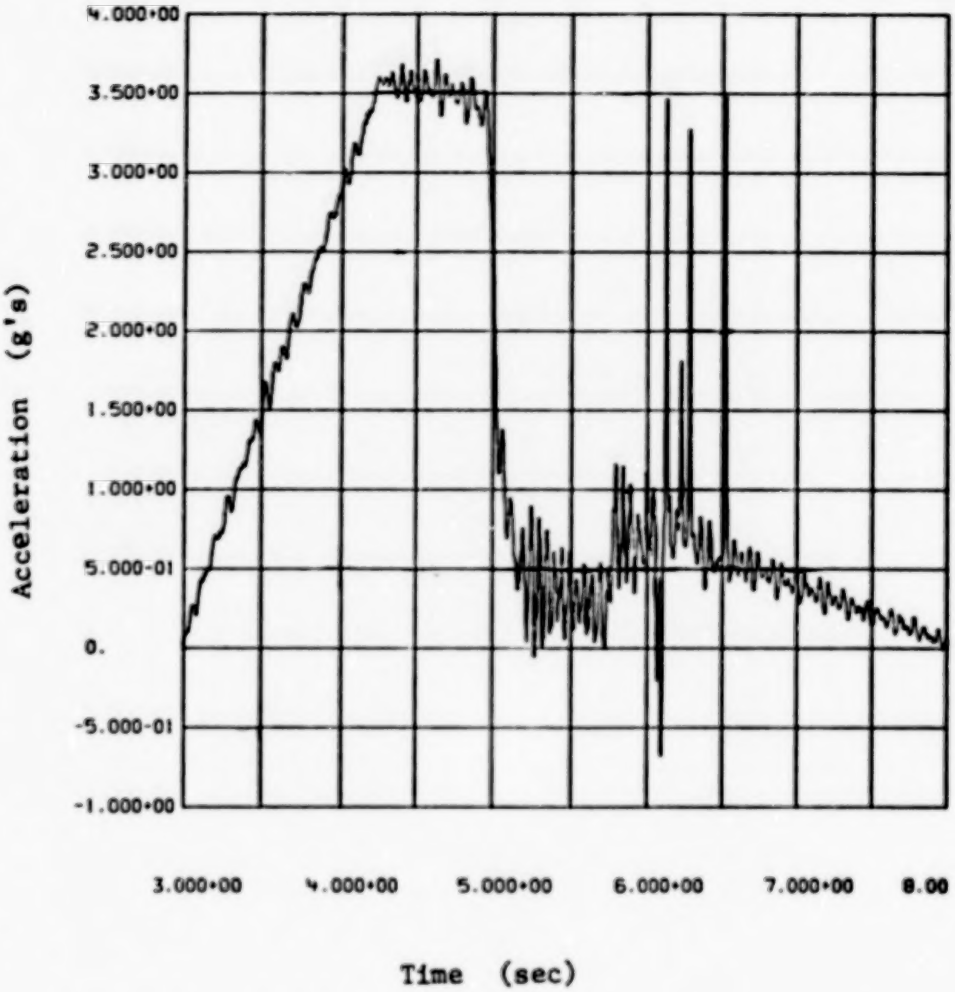

Figure 15. Acceleration Time History for CM101A From E-1 Stage I Burnout With Front and End Ramps

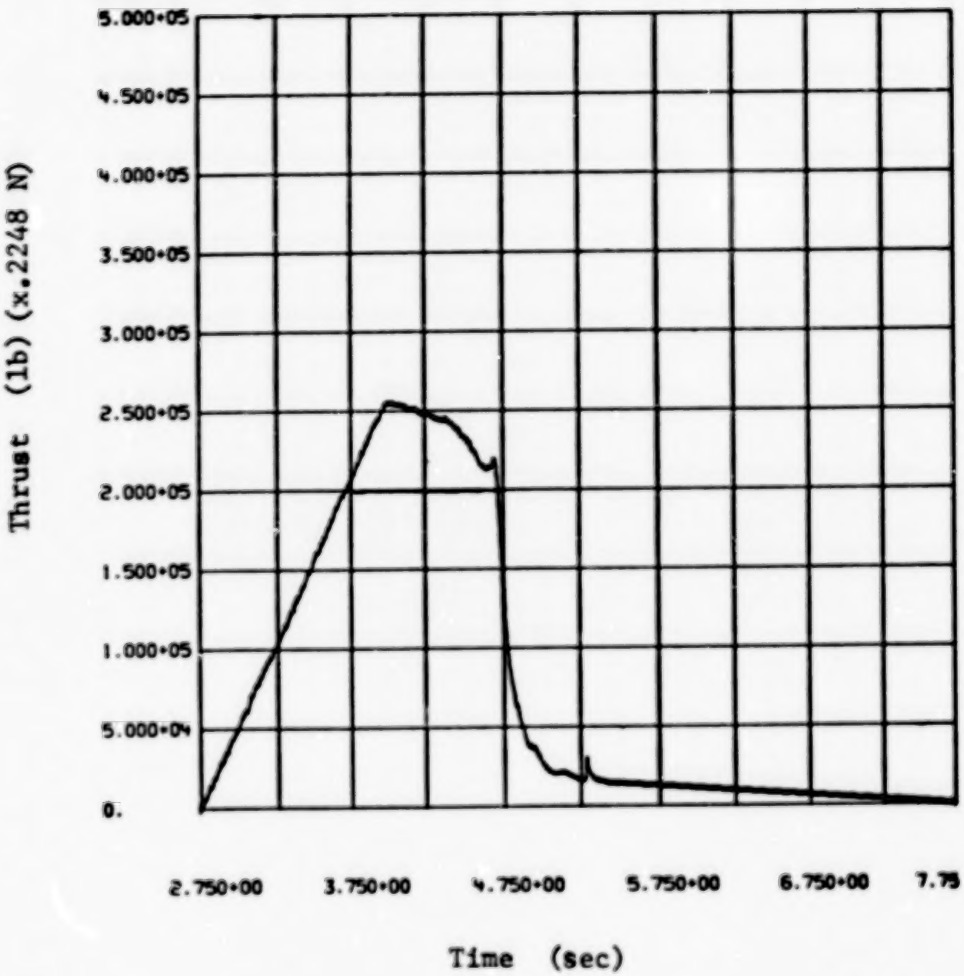

Figure 16. Pressure Time History for TP3015 From E-2 Stage I Burnout With Front and End Ramps

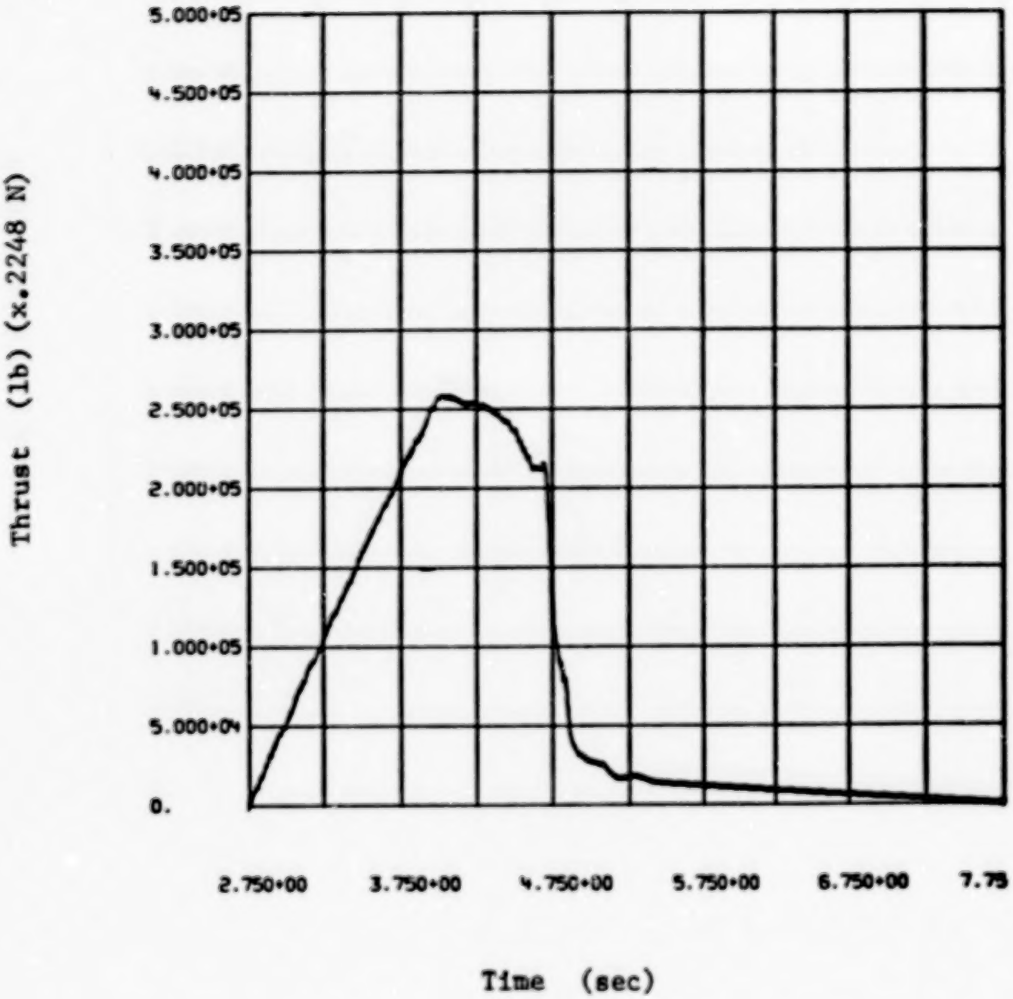

Figure 17. Pressure Time History for TP3016 From E-2 Stage I Burnout With Front and End Ramps

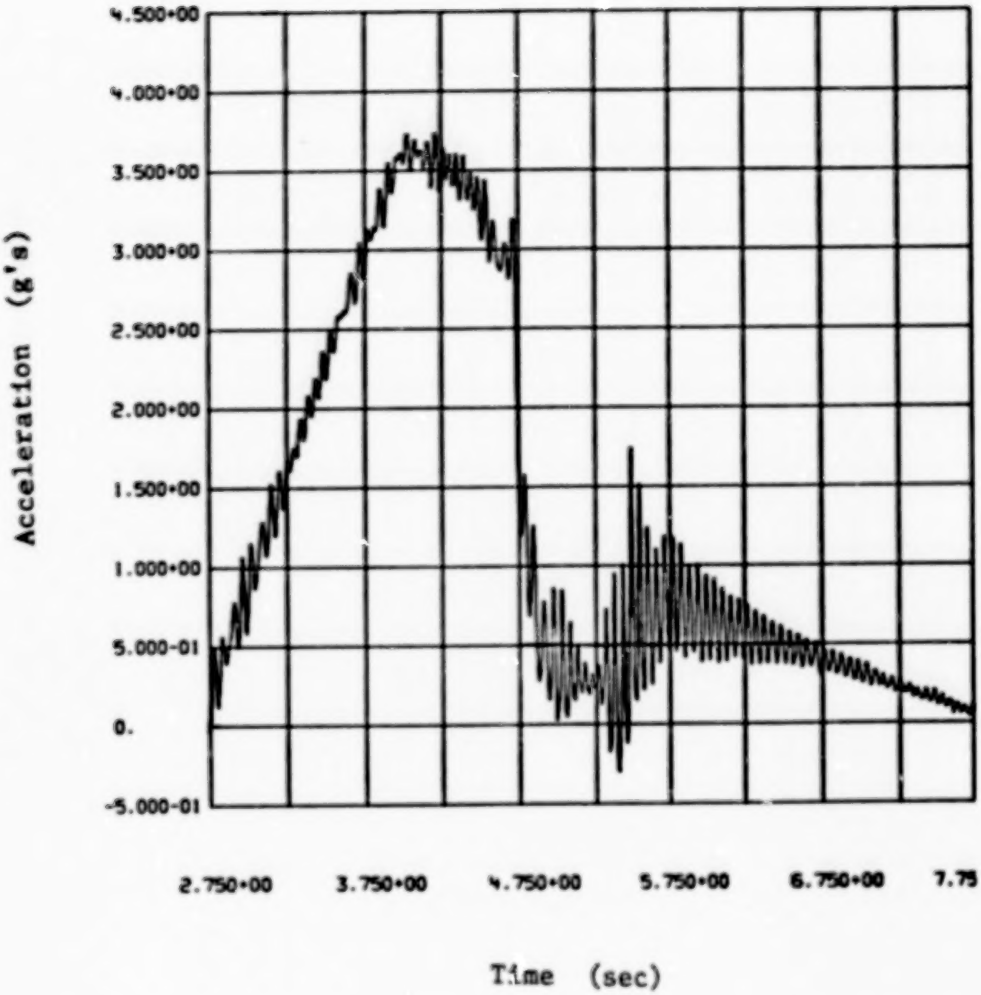

Figure 18. Acceleration Time History for CM101A From E-2 Stage I Burnout With Front and End Ramps

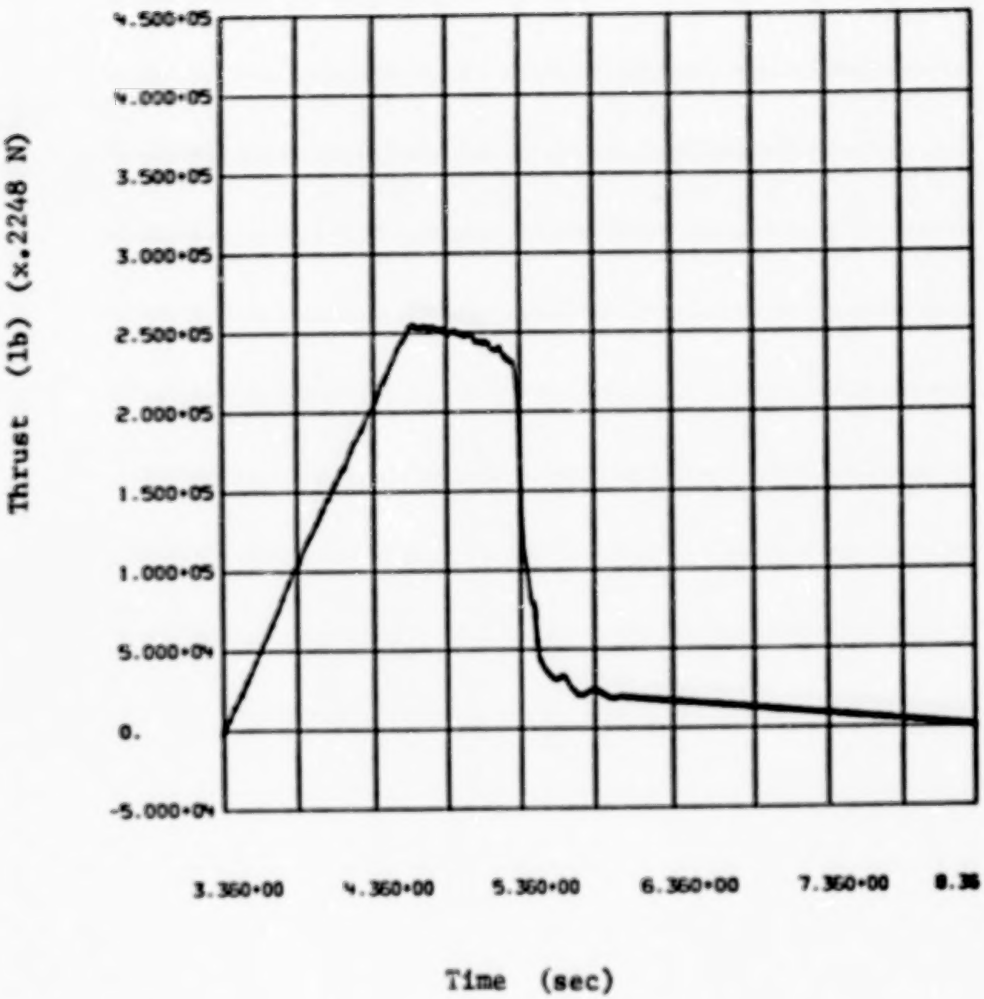

Figure 19. Pressure Time History for TP3015 From E-3 Stage I Burnout With Front and End Ramps

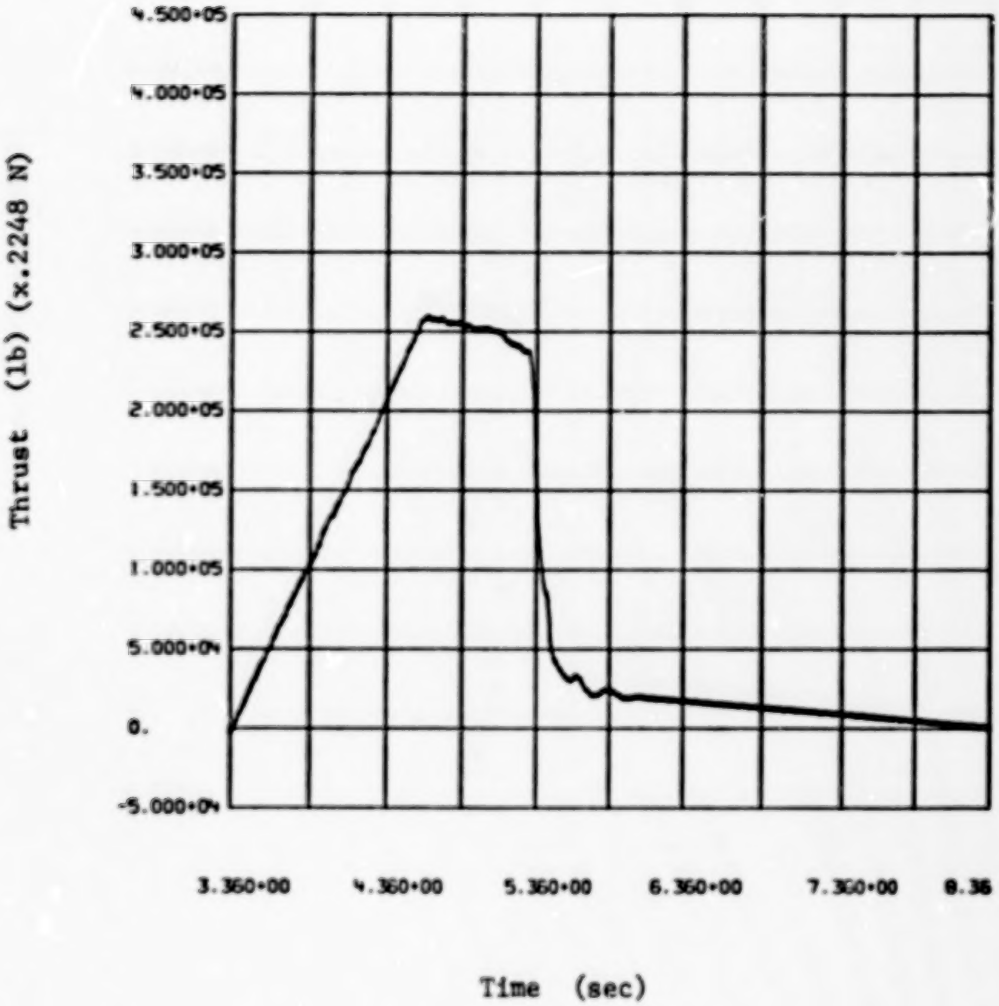

Figure 20. Pressure Time History for TP3016 From E-3 Stage I Burnout With Front and End Ramps

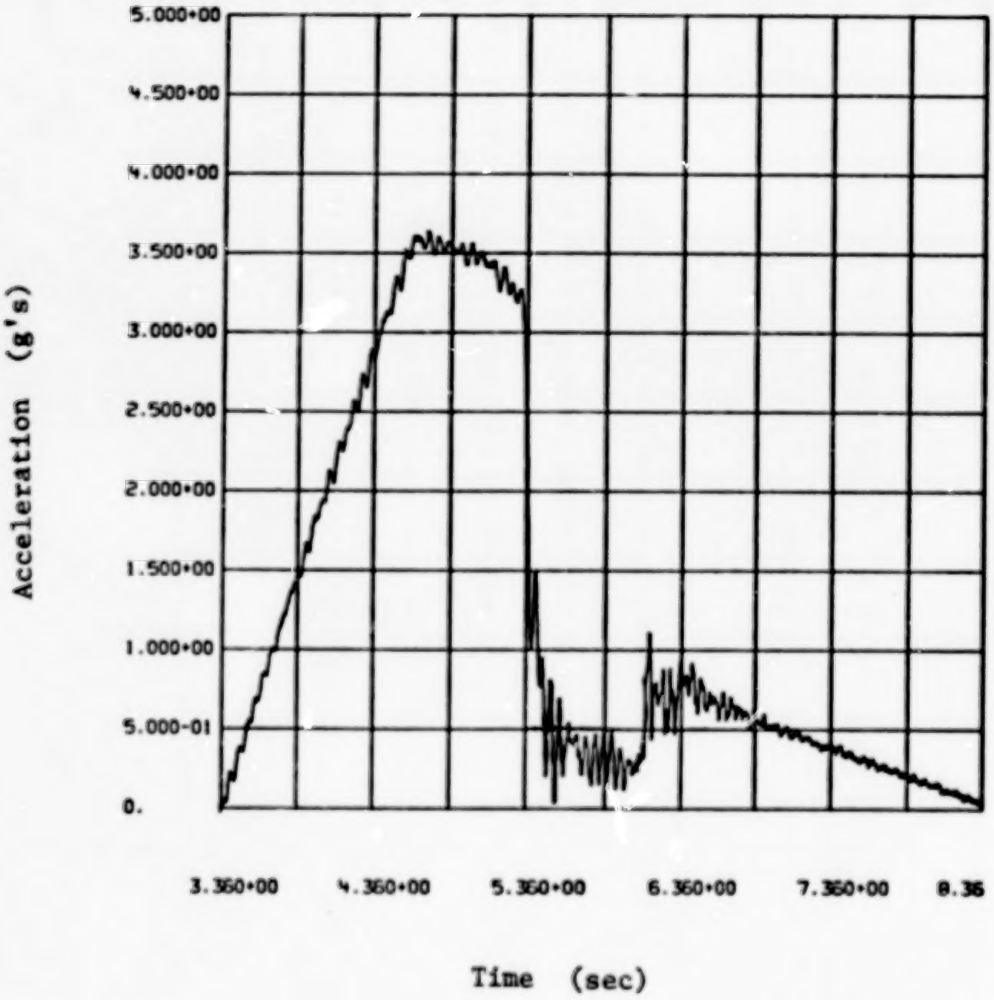

Figure 21. Acceleration Time History for CM101A From E-3 Stage I Burnout With Front and End Ramps

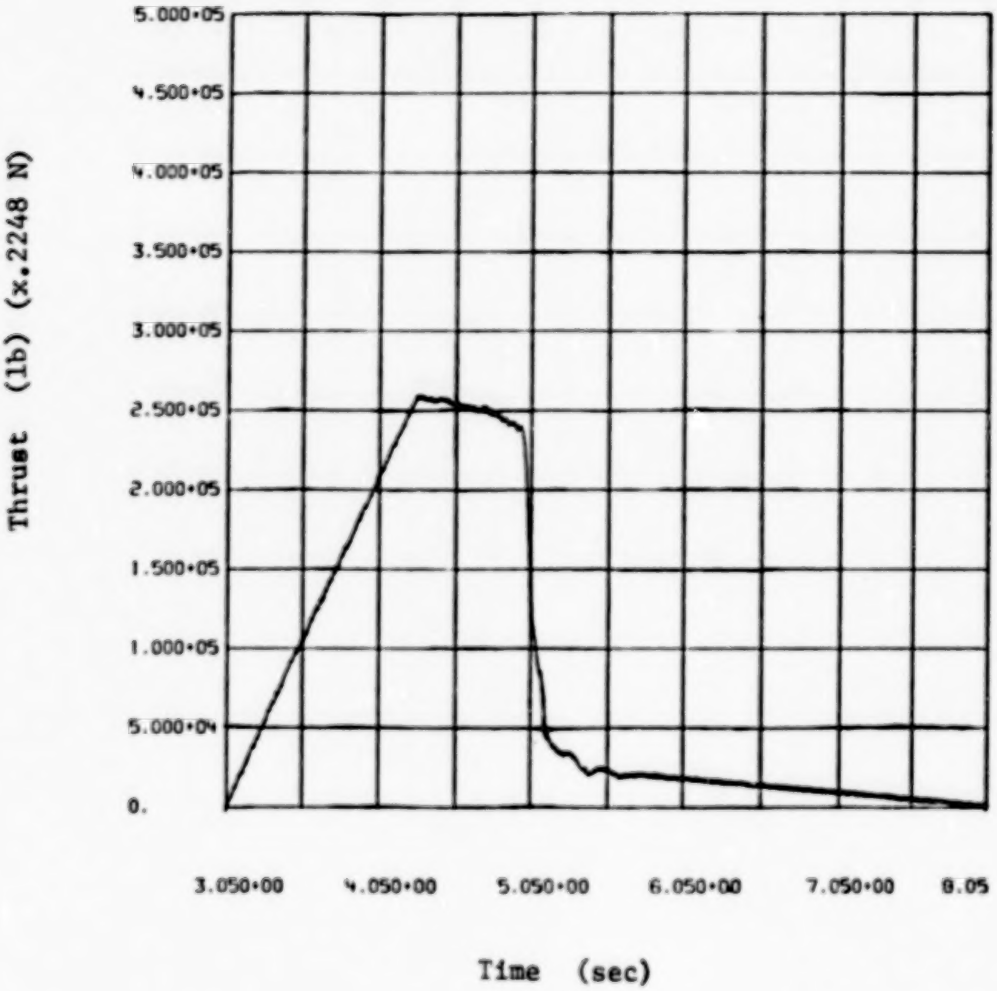

Figure 22. Pressure Time History for TP3015 From E-4 Stage I Burnout With Front and End Ramps

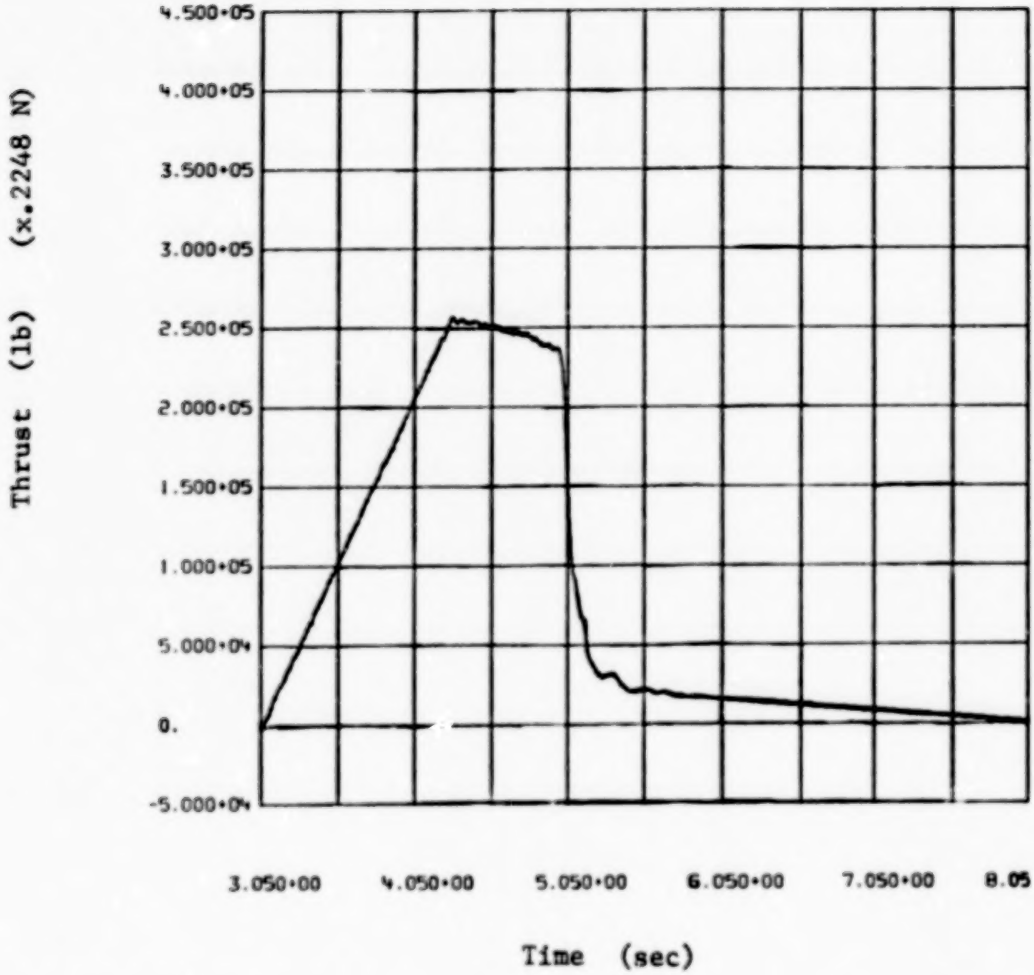

Figure 23. Pressure Time History for TP3016 From E-4 Stage I Burnout With Front and End Ramps

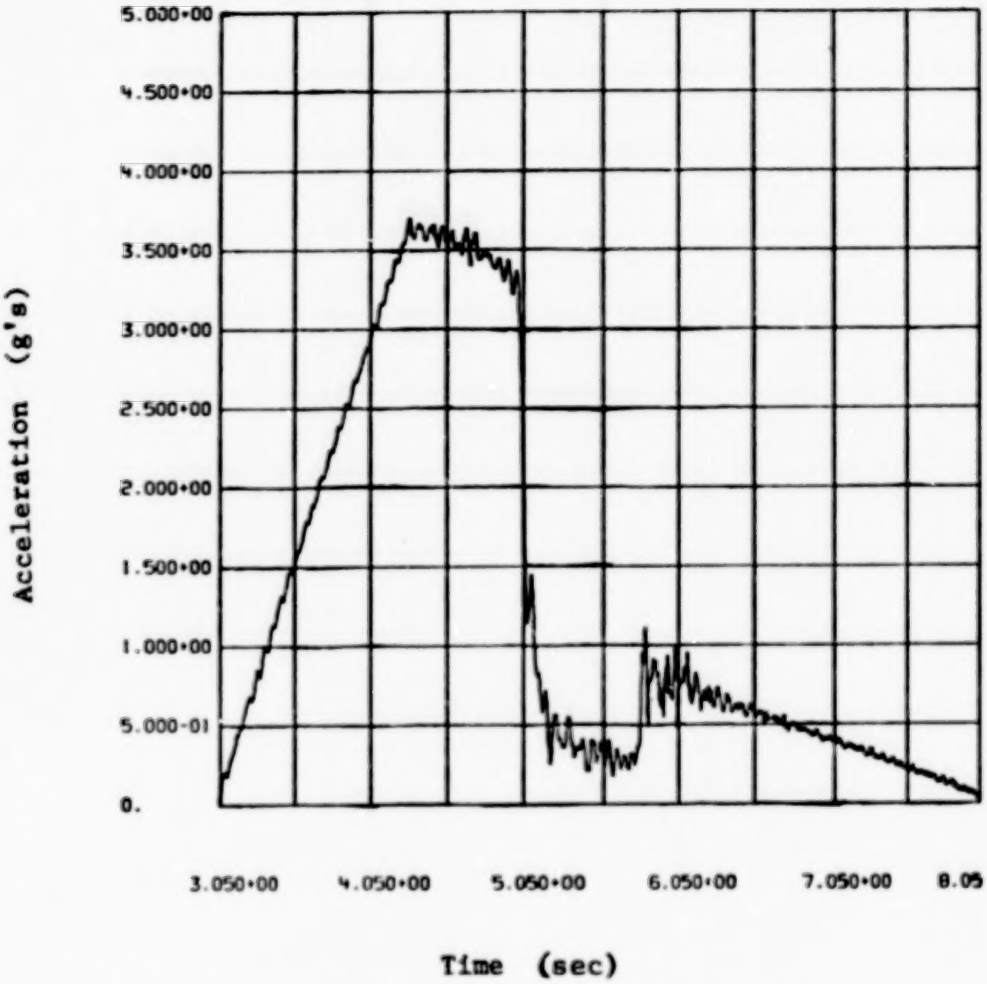

Figure 24. Acceleration Time History for CM101A From E-4 Stage I Burnout With Front and End Ramps

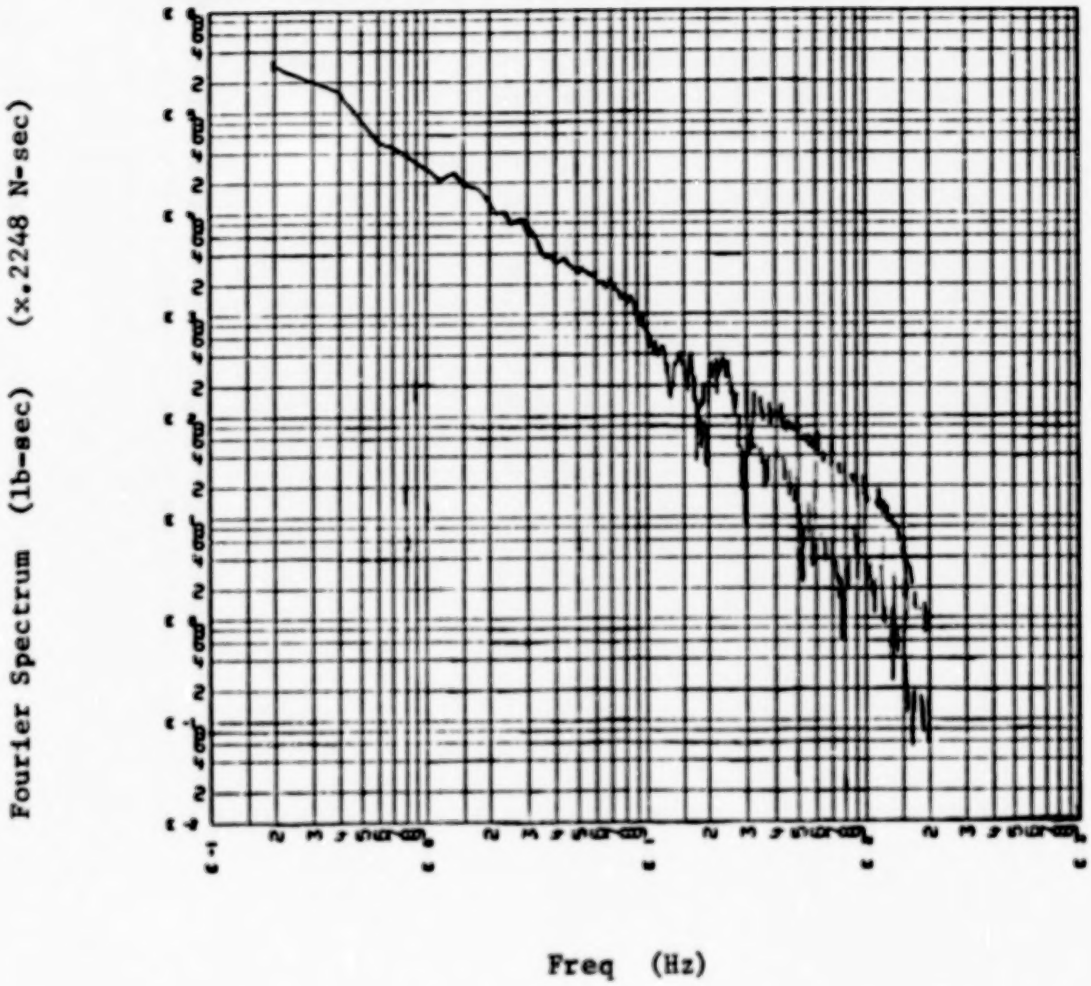

Figure 25. Fourier Spectrum of TP3015 From E-1 Stage I Burnout

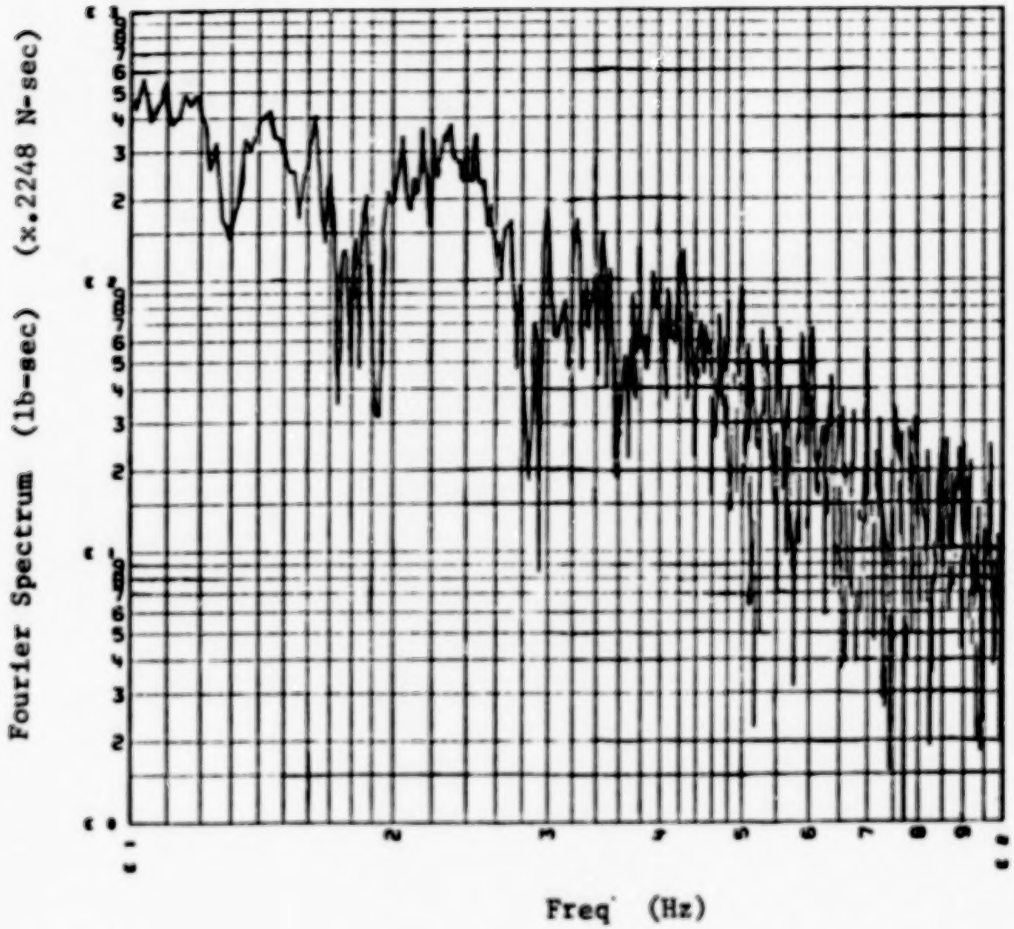

Figure 26. Fourier Spectrum of TP3015 From E-1 Stage I Burnout (10-100 Hz)

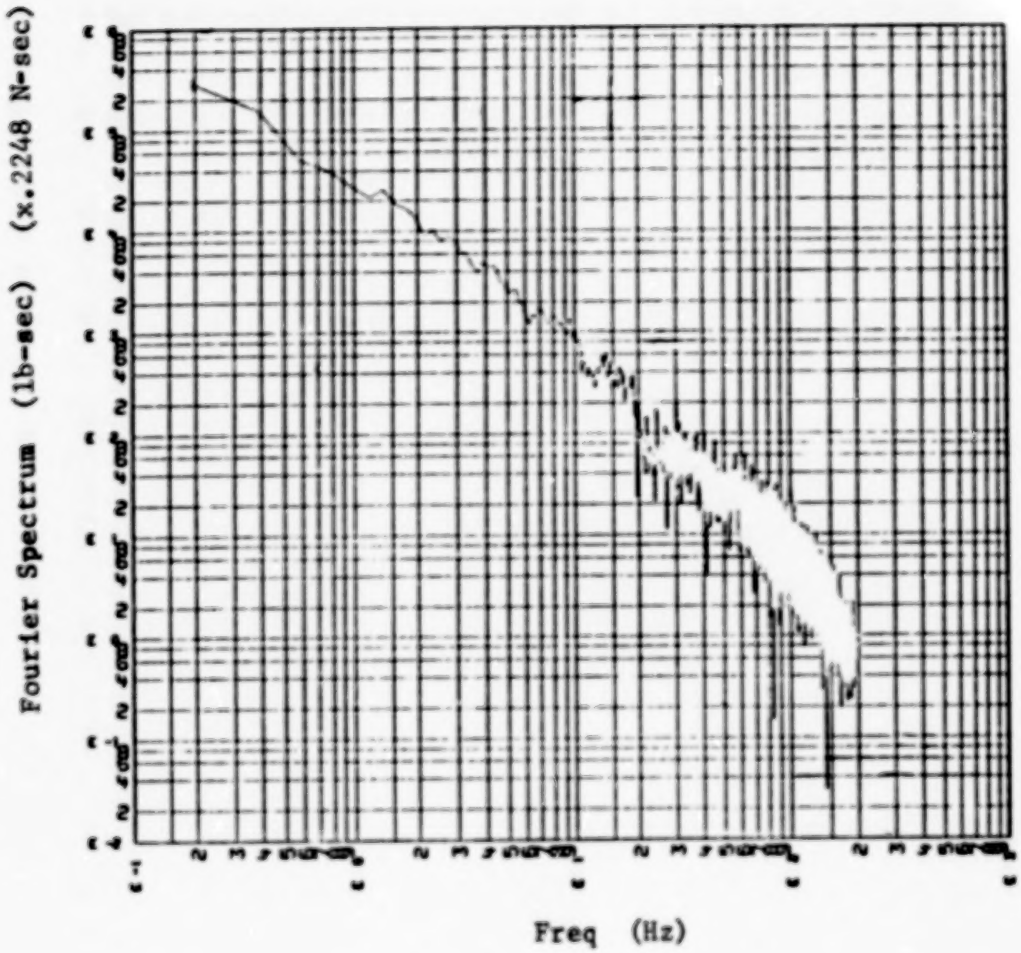

Figure 27. Fourier Spectrum of TP3016 From E-1 Stage I Burnout

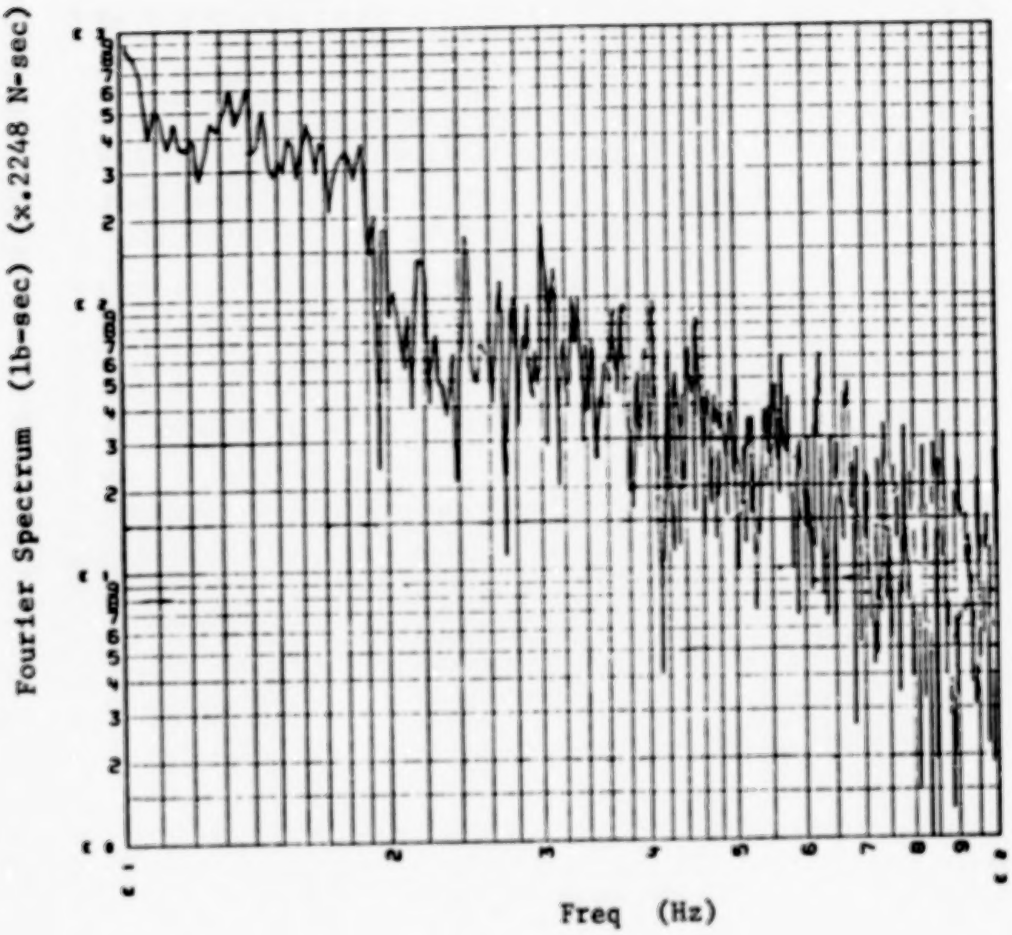

Figure 28. Fourier Spectrum of TP3016 From E-1 Stage I Burnout (10-100 Hz)

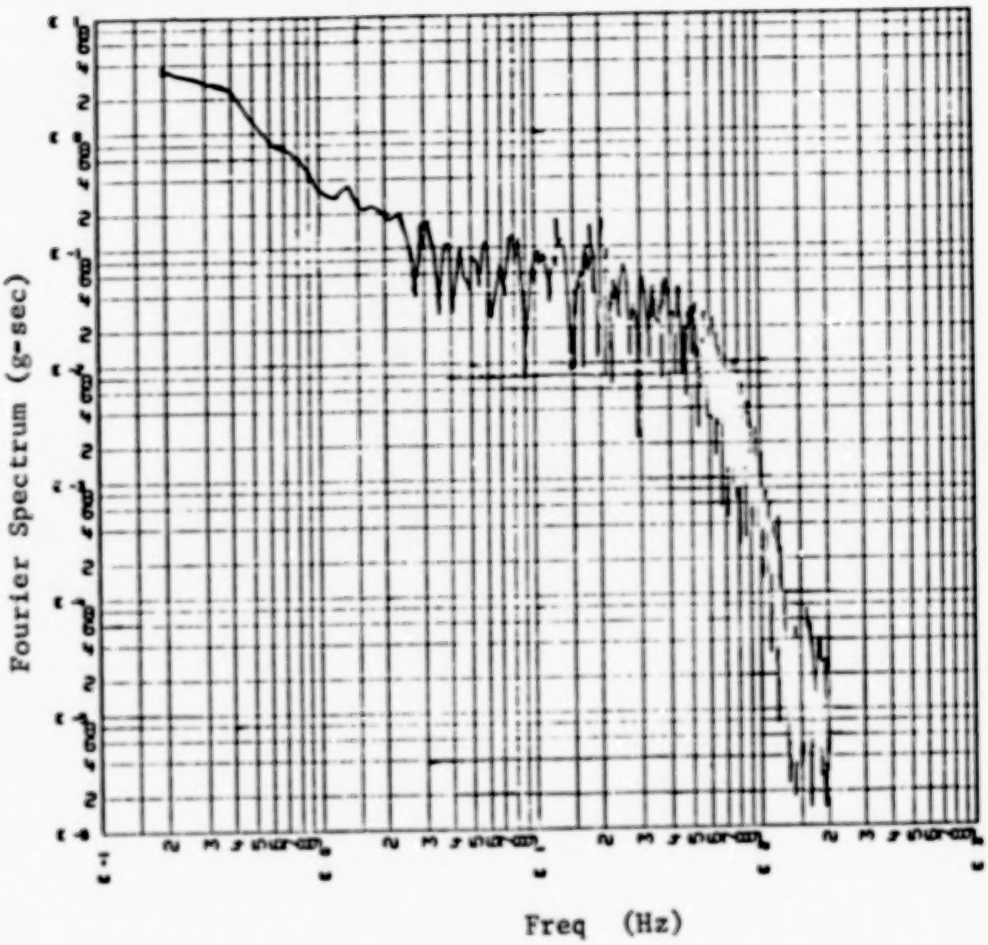

Figure 29. Fourier Spectrum of CM101A From E-1 Stage I Burnout

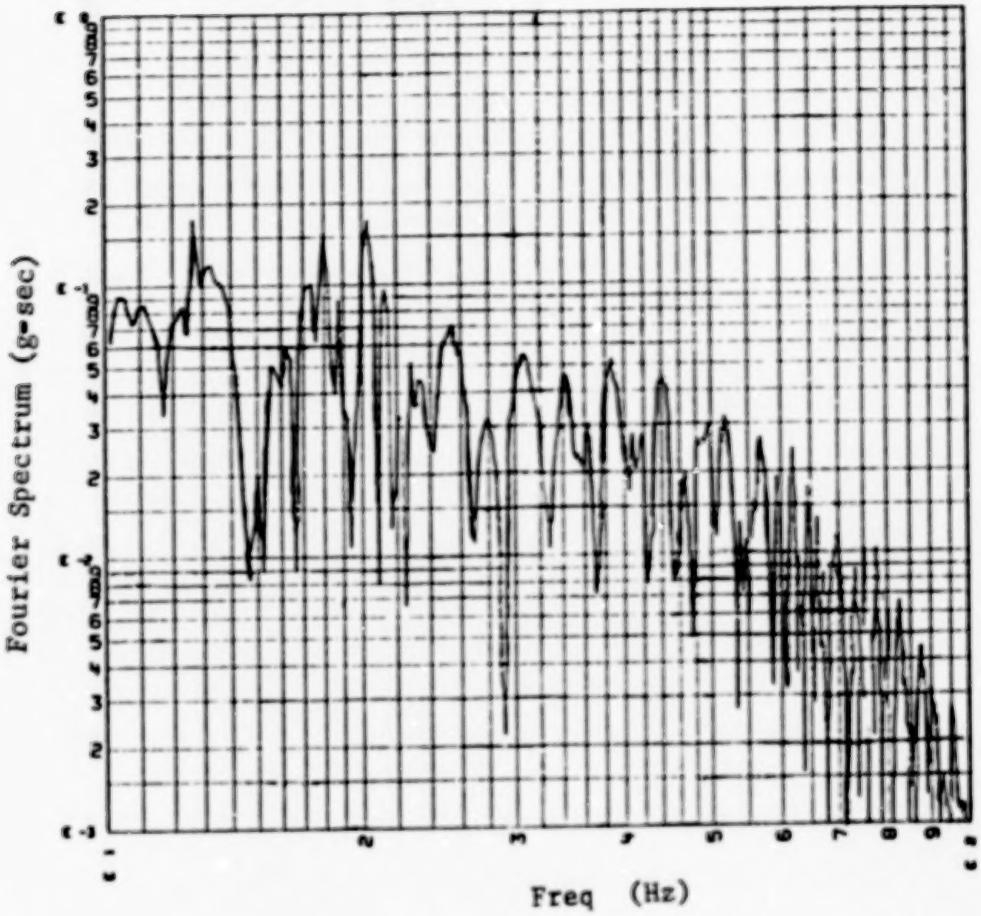

Figure 30. Fourier Spectrum of CM101A From E-1 Stage I Burnout (10-100 Hz)

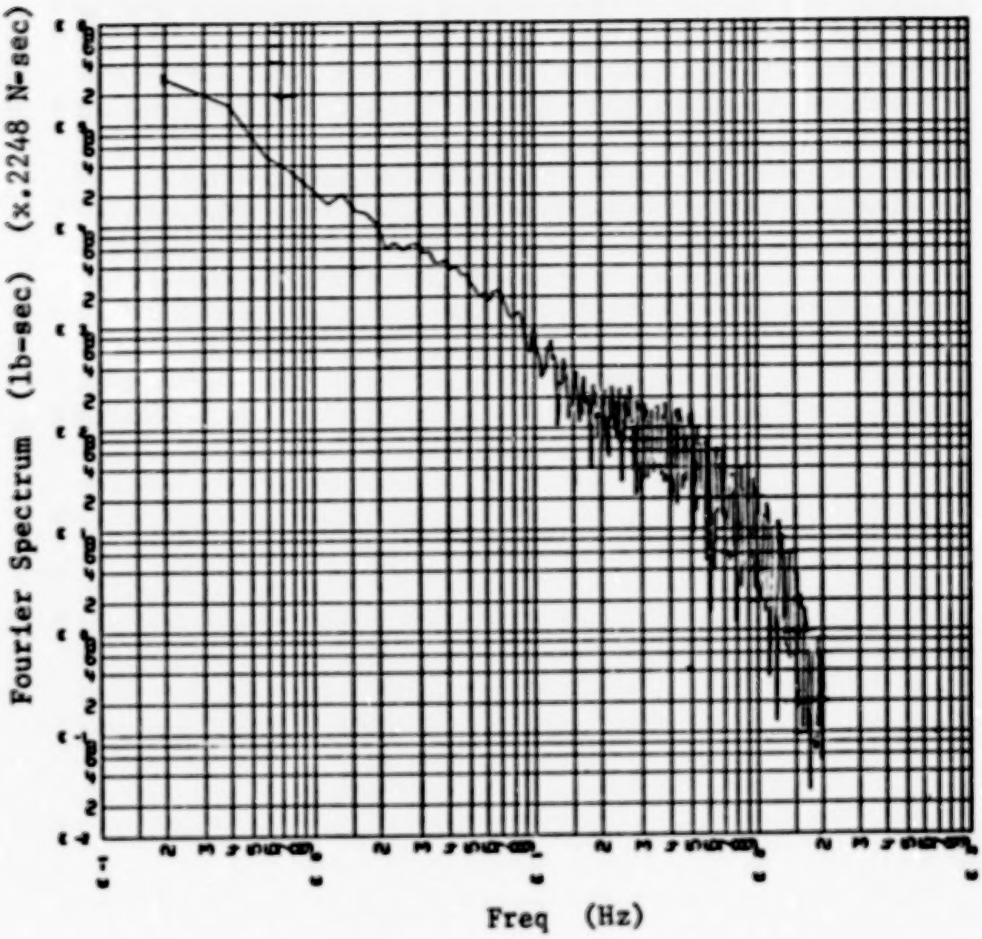

Figure 31. Fourier Spectrum of TP3015 From E-2 Stage I Burnout

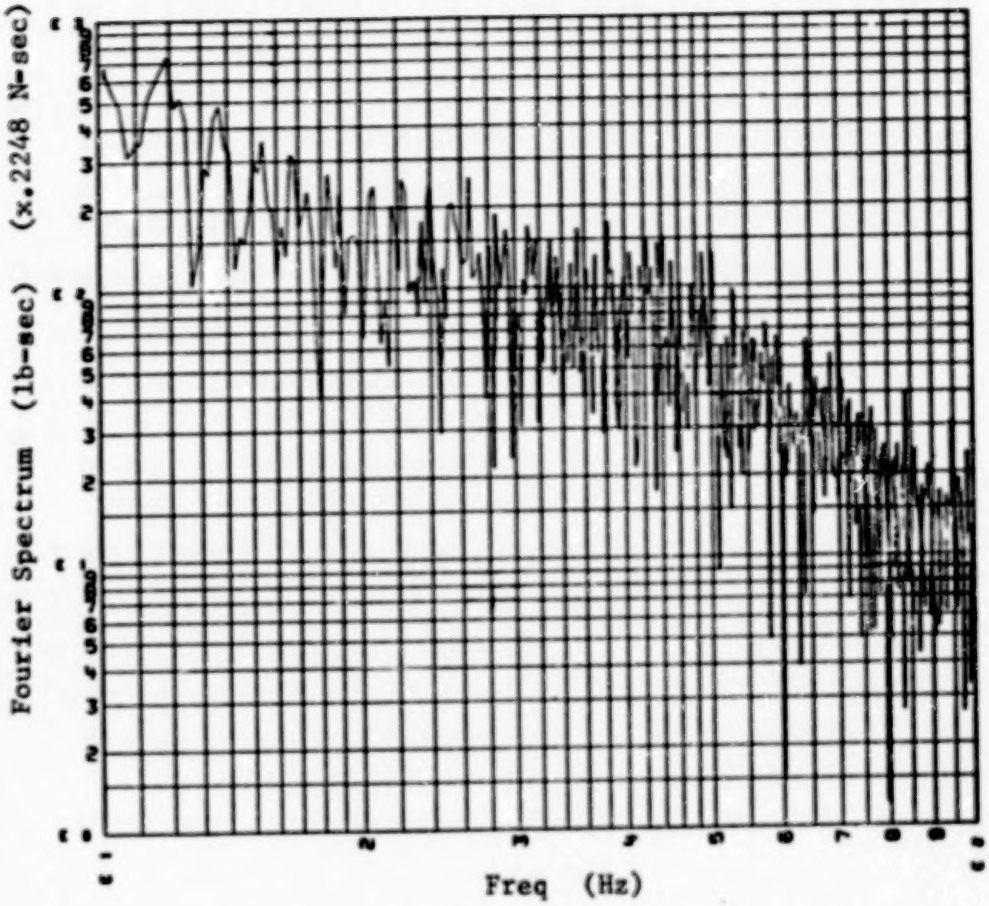

Figure 32. Fourier Spectrum of TP3015 From E-2 Stage I Burnout (10-100 Hz)

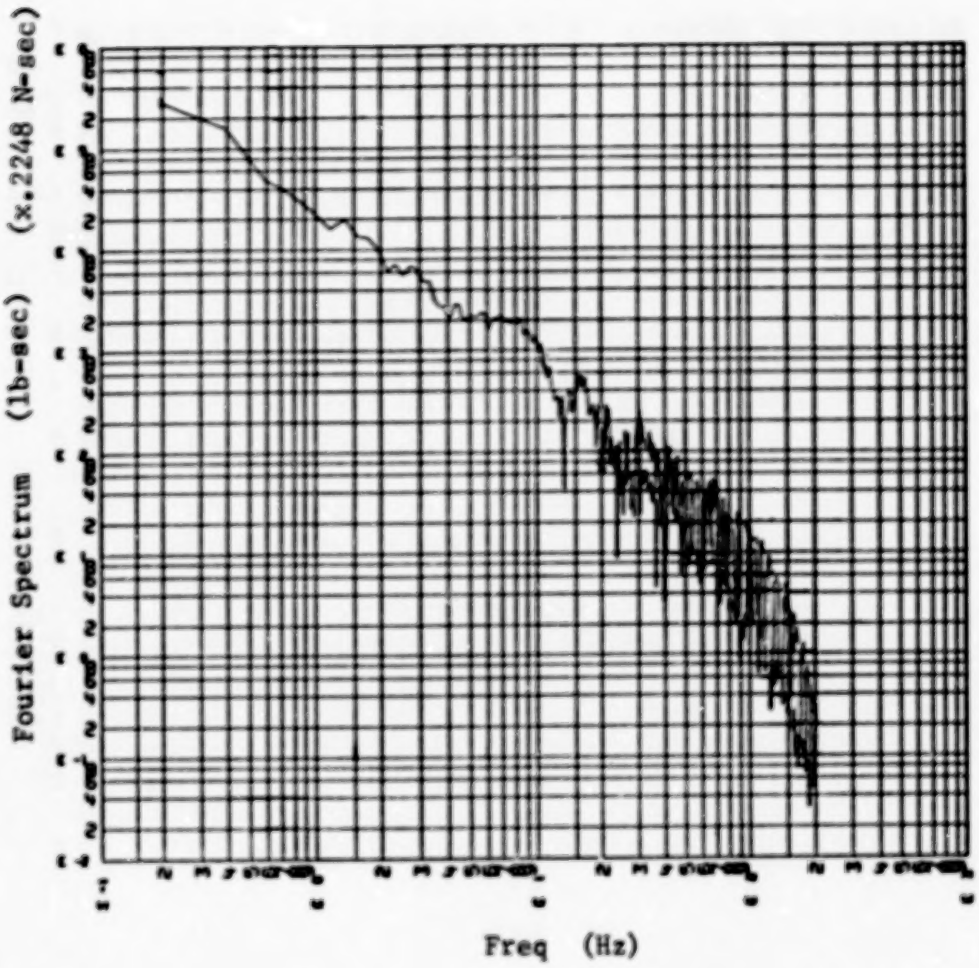

Figure 33. Fourier Spectrum of TP3016 From E-2 Stage I Burnout

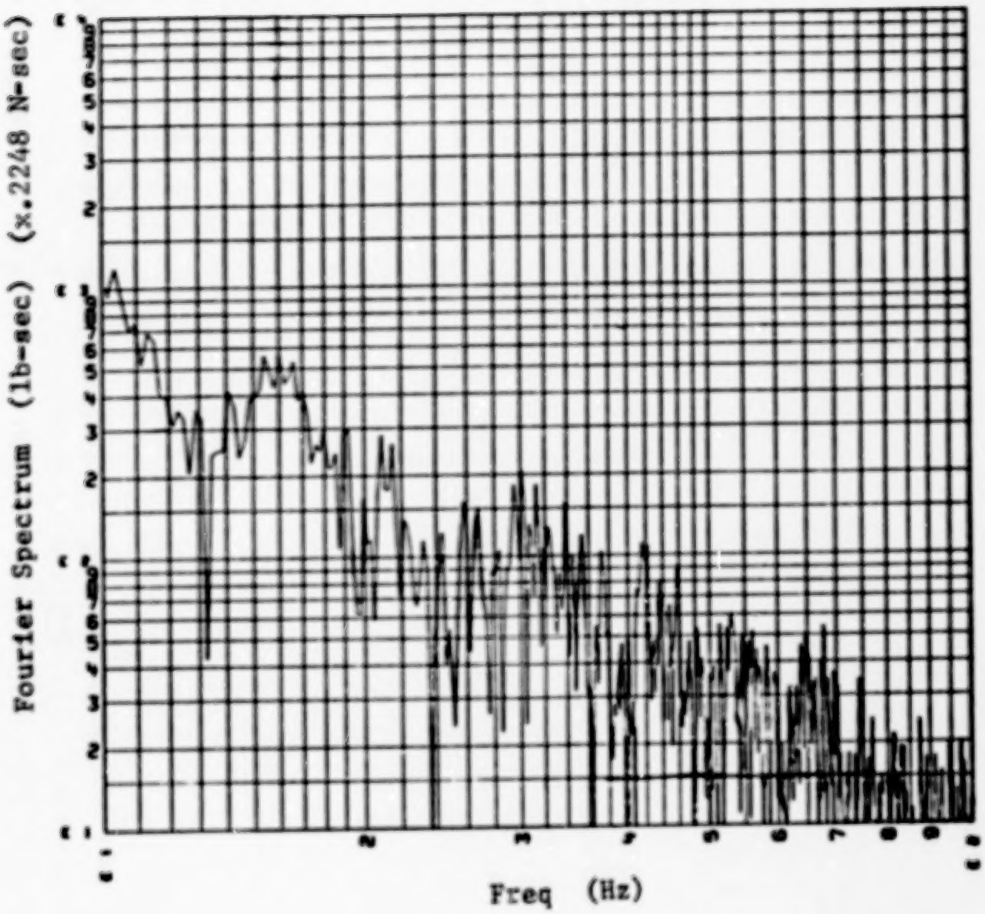

Figure 34. Fourier Spectrum of TP3016 From E-2 Stage I Burnout (10-100 Hz)

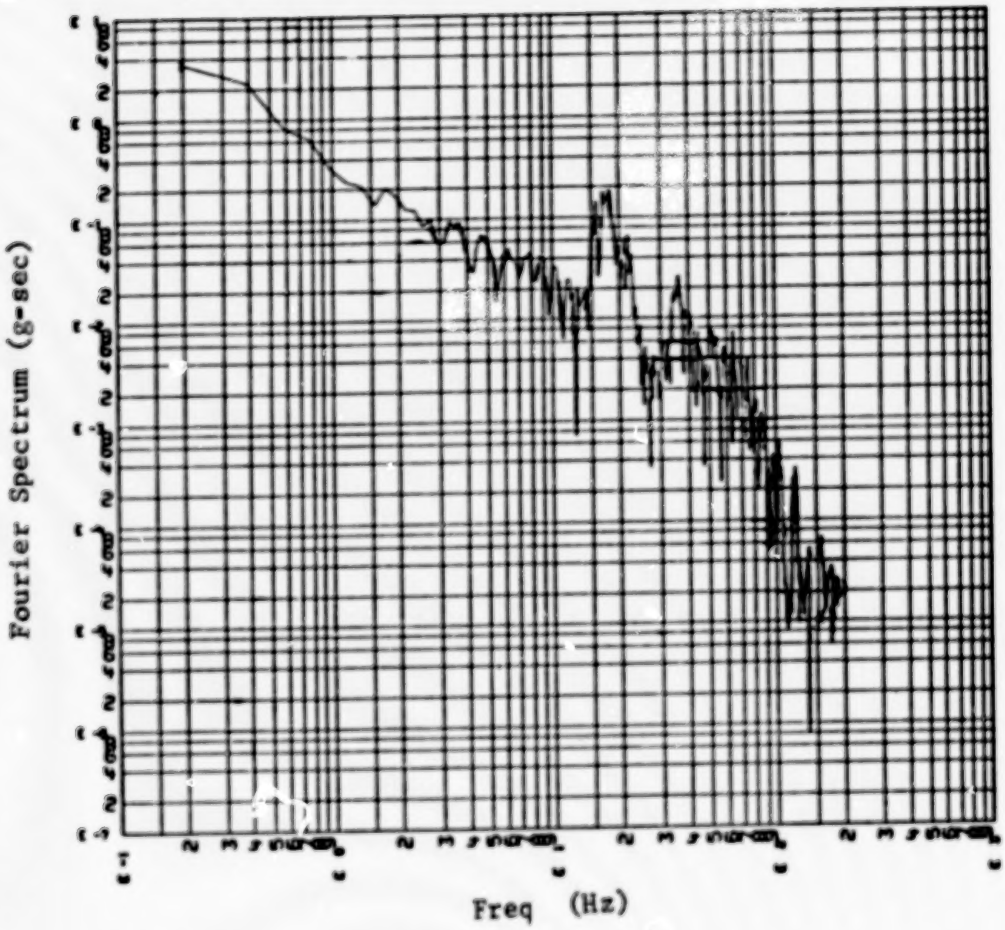

Figure 35. Fourier Spectrum of CM101A From E-2 Stage I Burnout

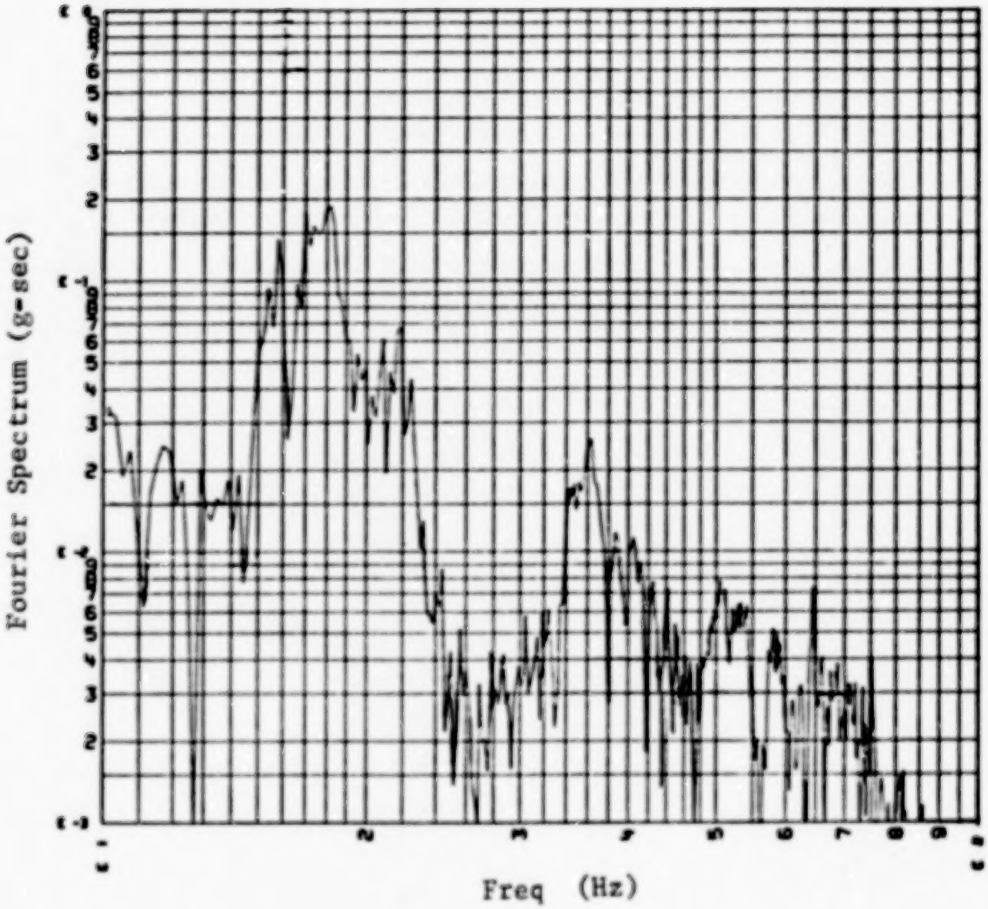

Figure 36. Fourier Spectrum of CM101A From E-2 Stage I Burnout (10-100 Hz)

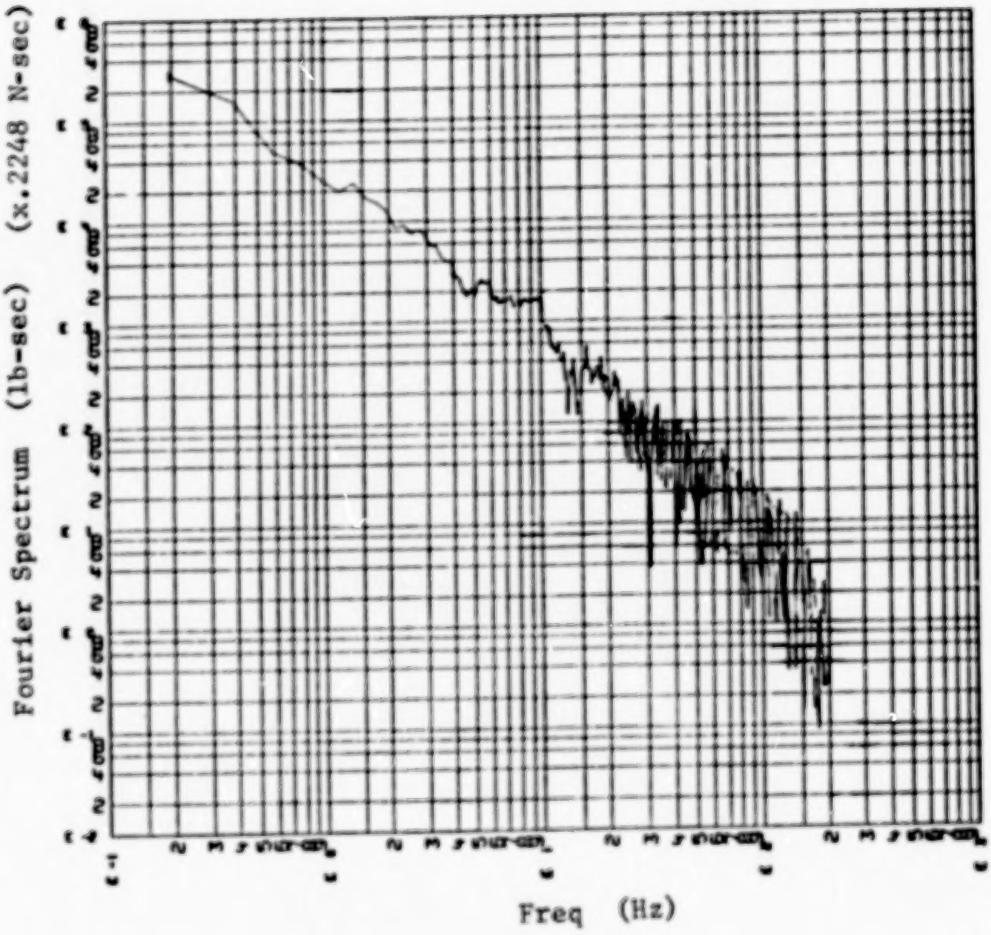

Figure 37. Fourier Spectrum of TP3015 From E-3 Stage I Burnout

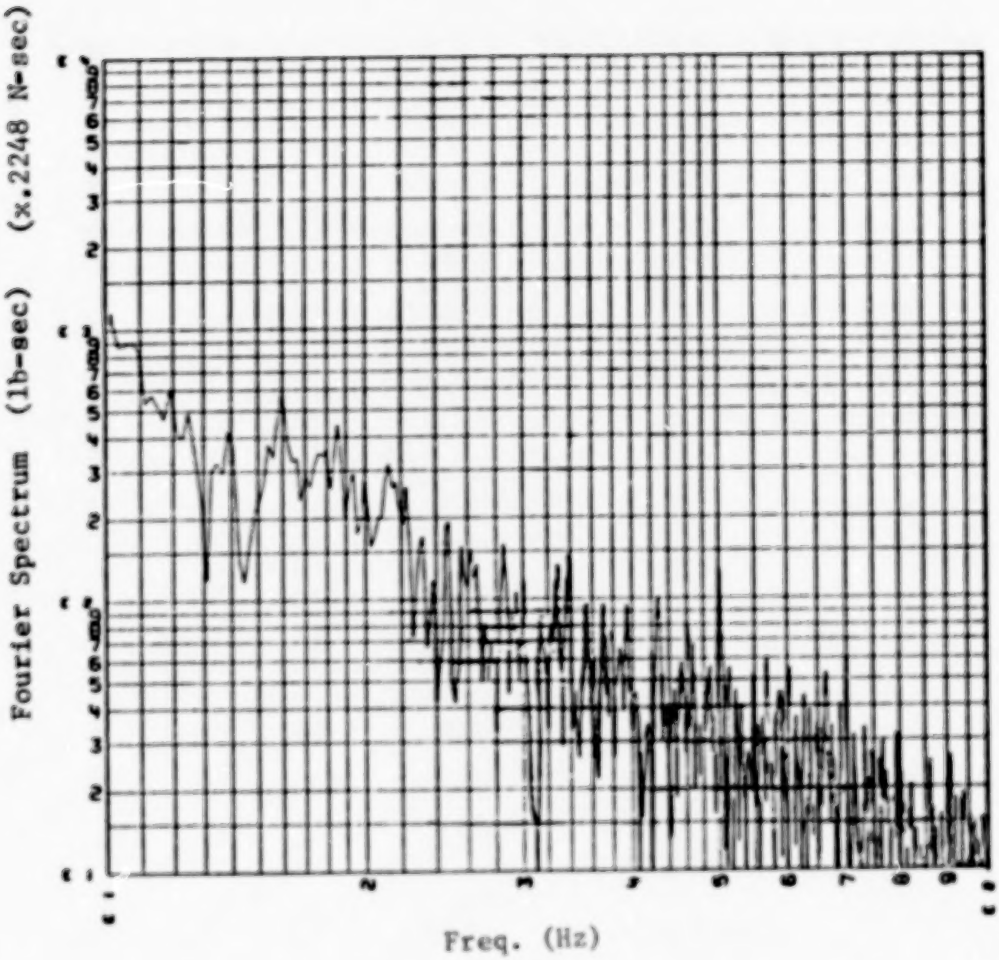

Figure 38. Fourier Spectrum of TP3015 From E-3 Stage I Burnout (10-100 Hz)

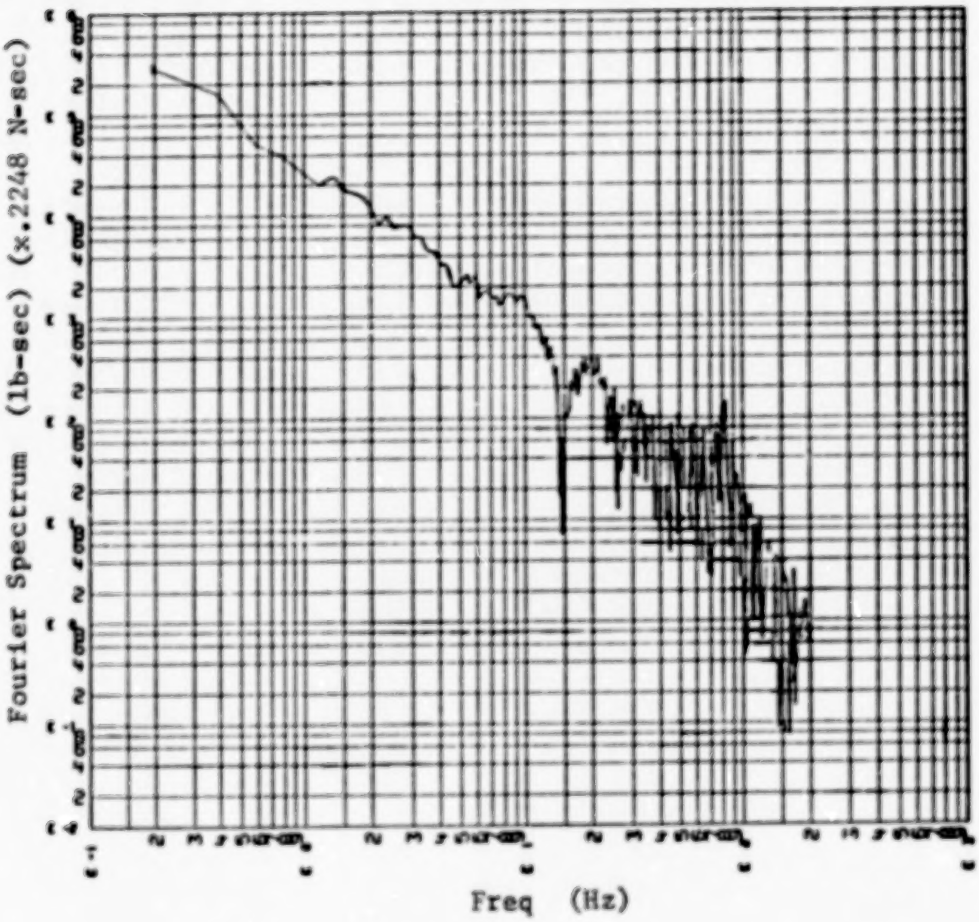

Figure 39. Fourier Spectrum of TP3016 From E-3 Stage I Burnout

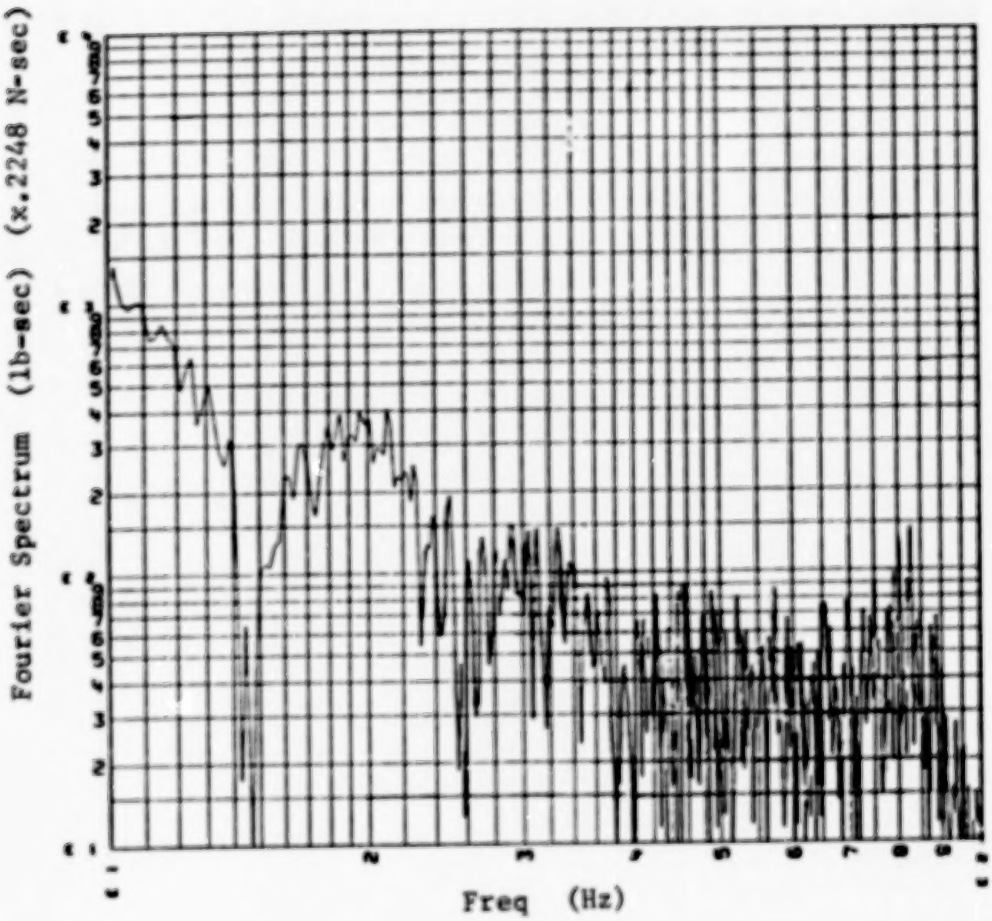

Figure 40. Fourier Spectrum of TP3016 From E-3 Stage I Burnout (10-100 Hz)

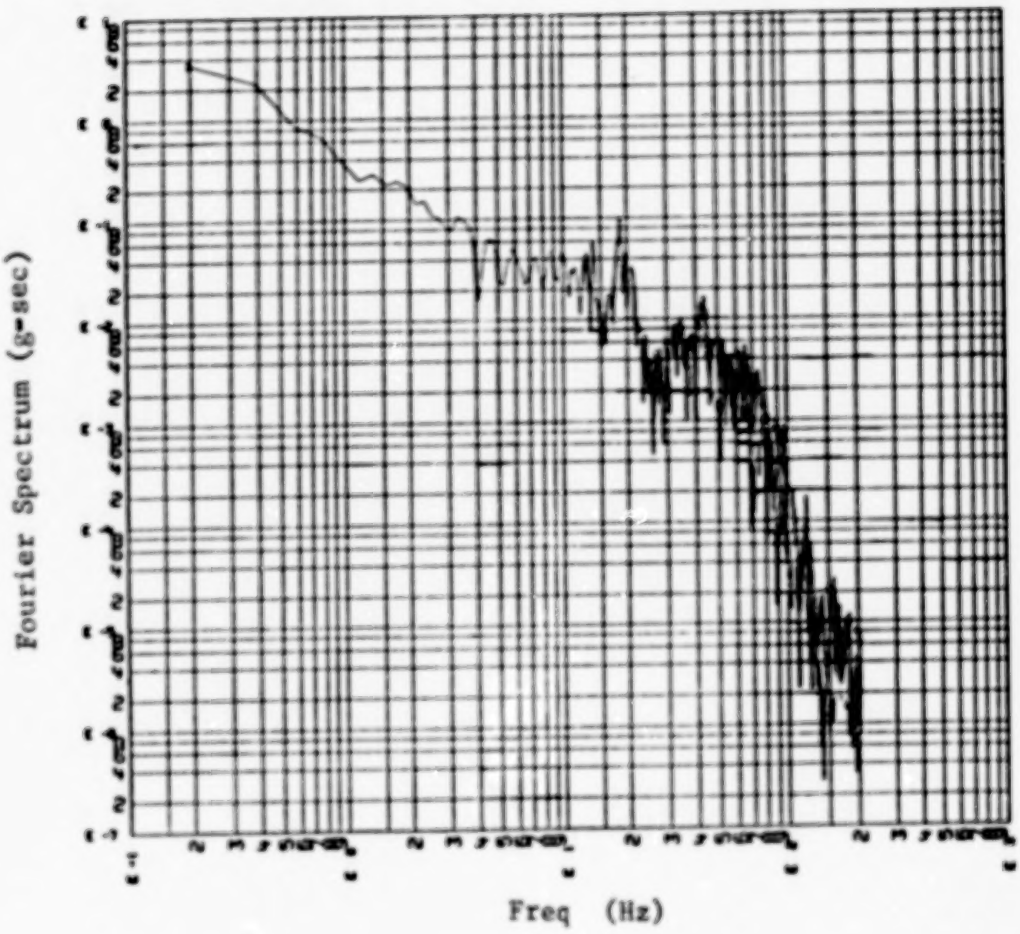

Figure 41. Fourier Spectrum of CM101A From E-3 Stage I Burnout

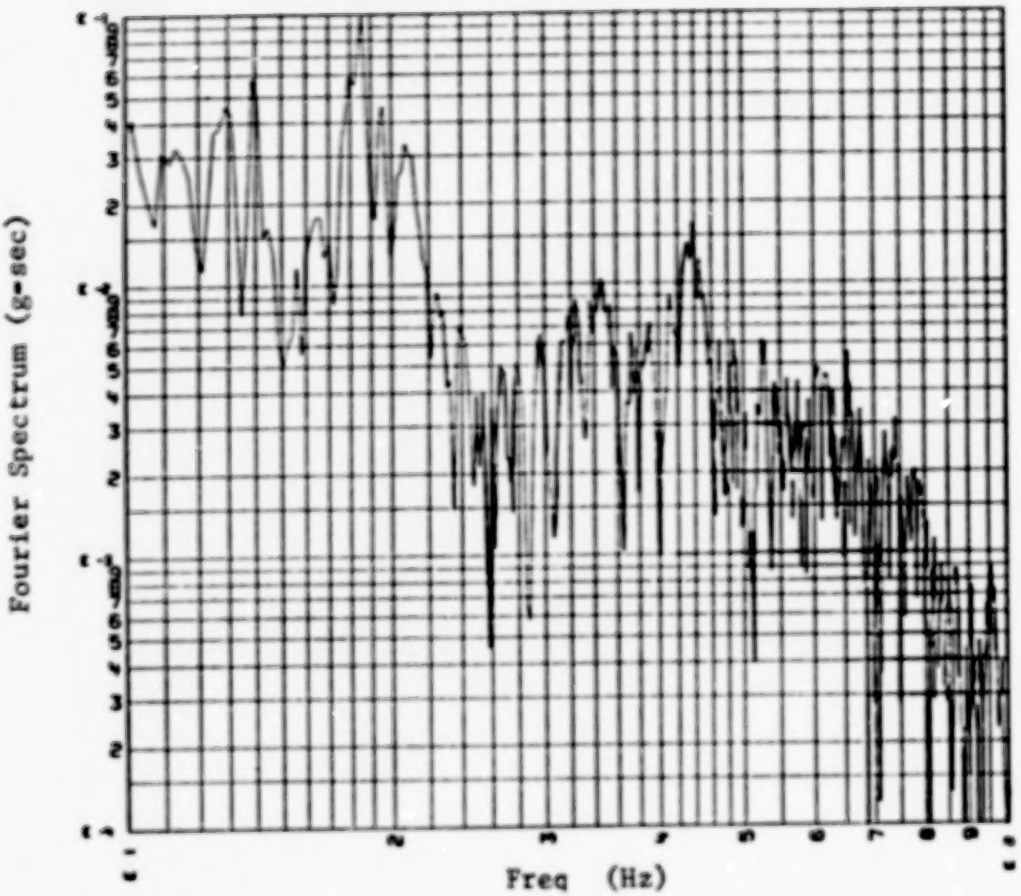

Figure 42. Fourier Spectrum of CM101A From E-3 Stage I Burnout (10-100 Hz)

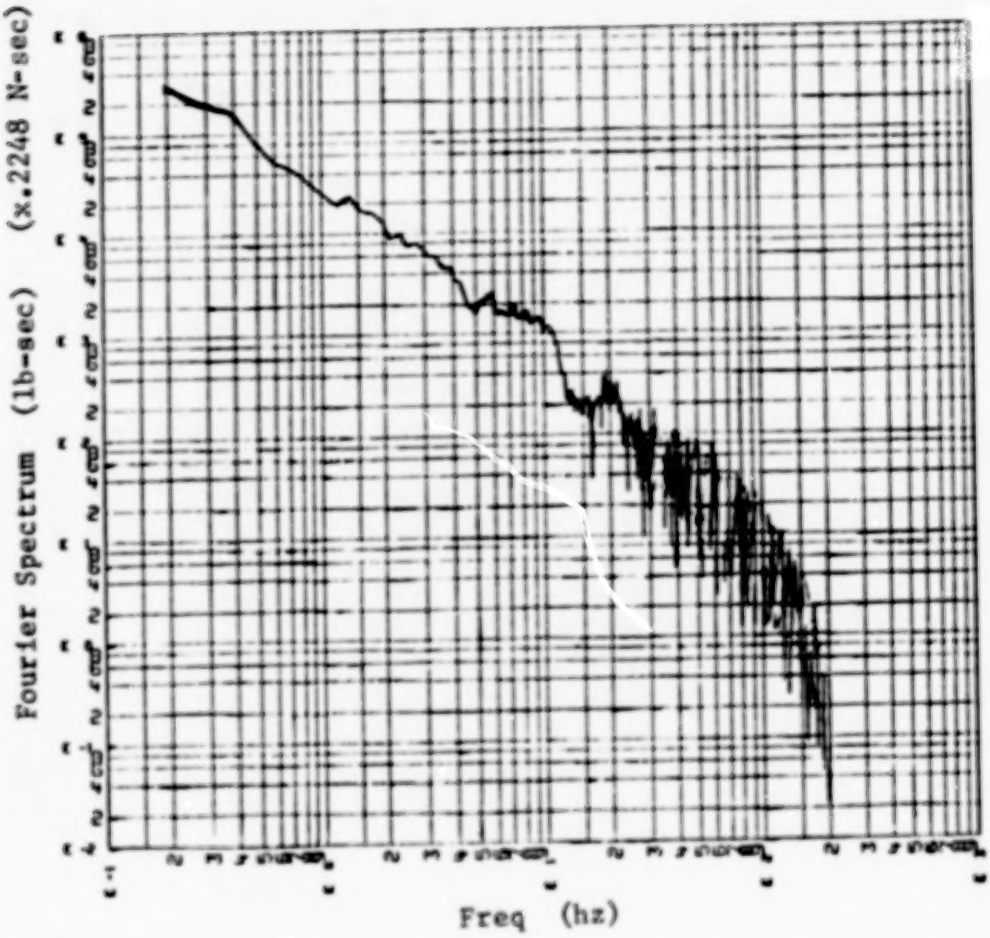

Figure 43. Fourier Spectrum of TP3015 From E-4 Stage I Burnout

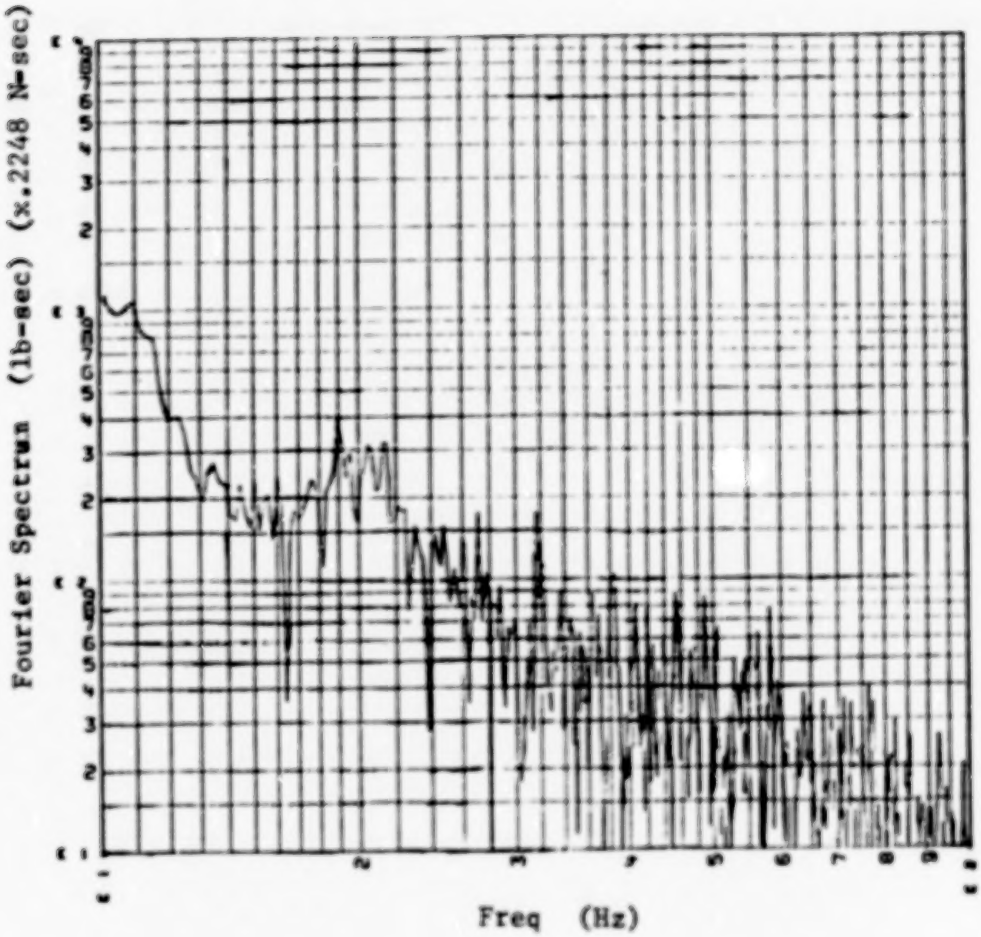

Figure 44. Fourier Spectrum of TP3015 From E-4 Stage I Burnout (10-100 Hz)

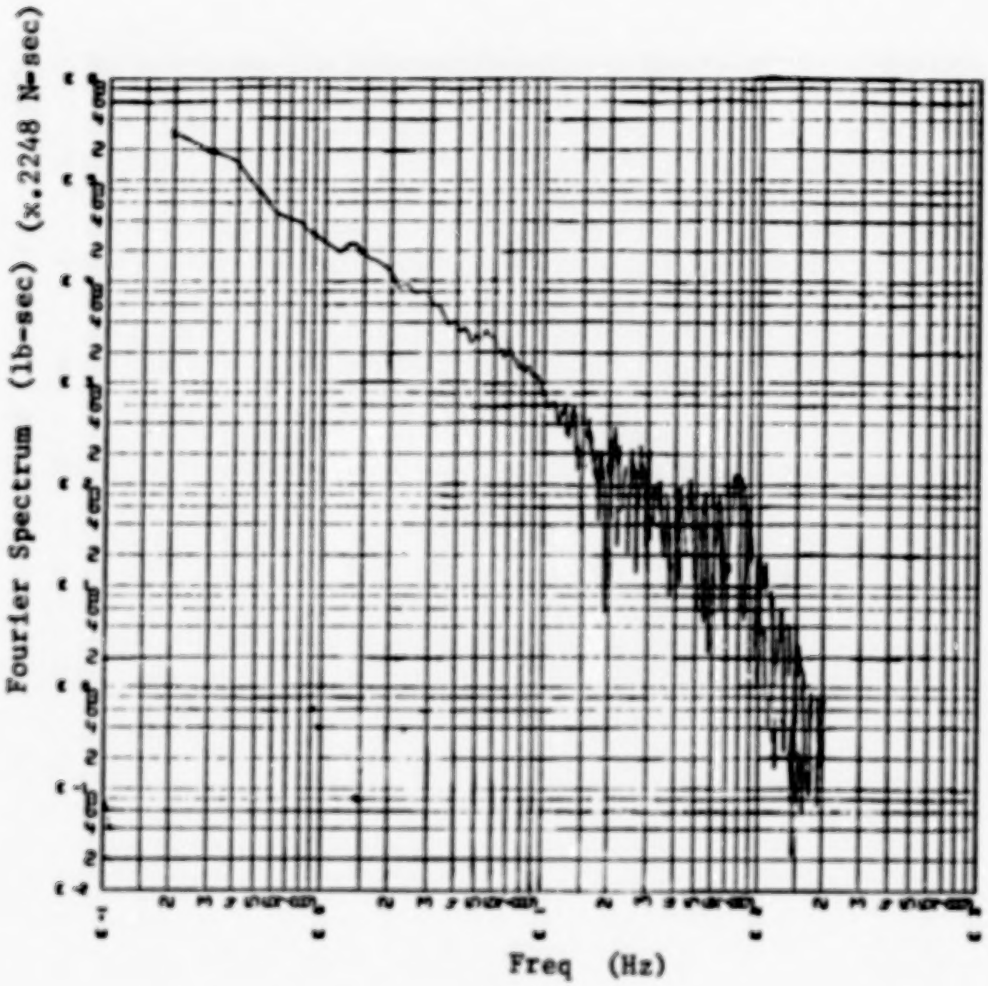

Figure 45. Fourier Spectrum of TP3016 From E-4 Stage I Burnout

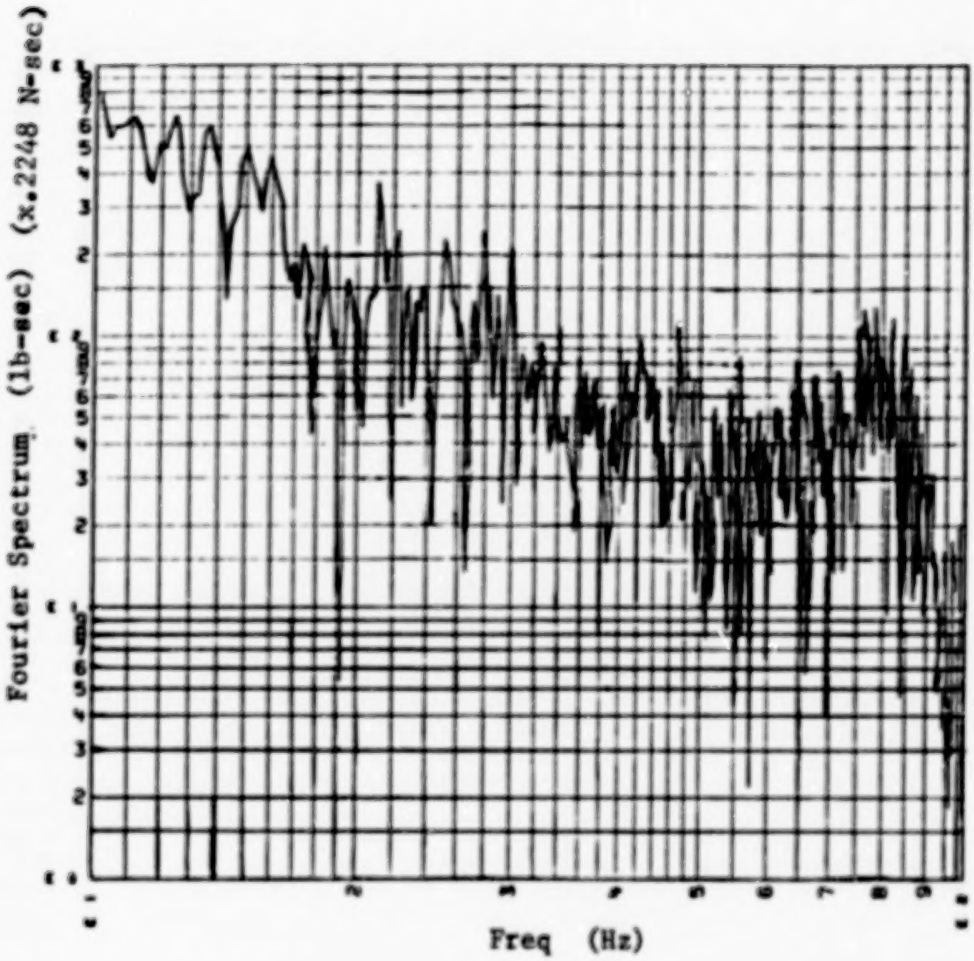

Figure 46. Fourier Spectrum of TP3016 From E-4 Stage I Burnout (10-100 Hz)

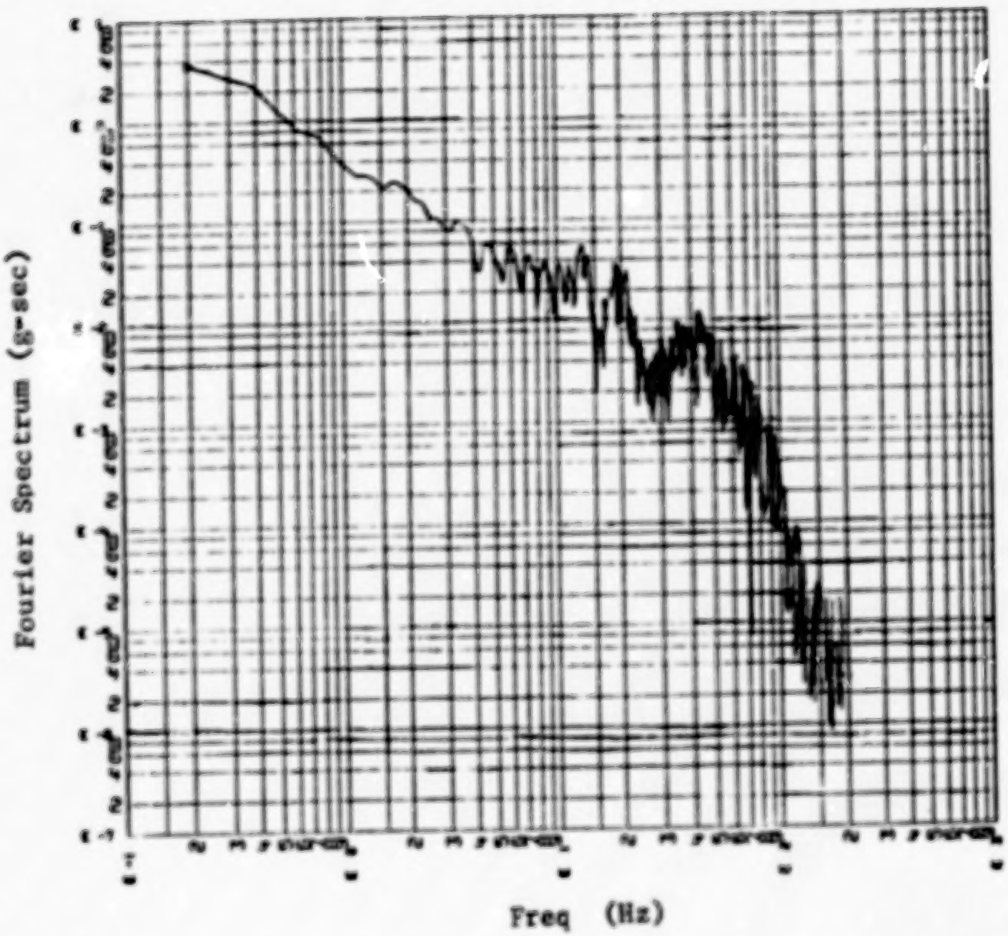

Figure 47. Fourier Spectrum of CM101A From E-4 Stage I Burnout

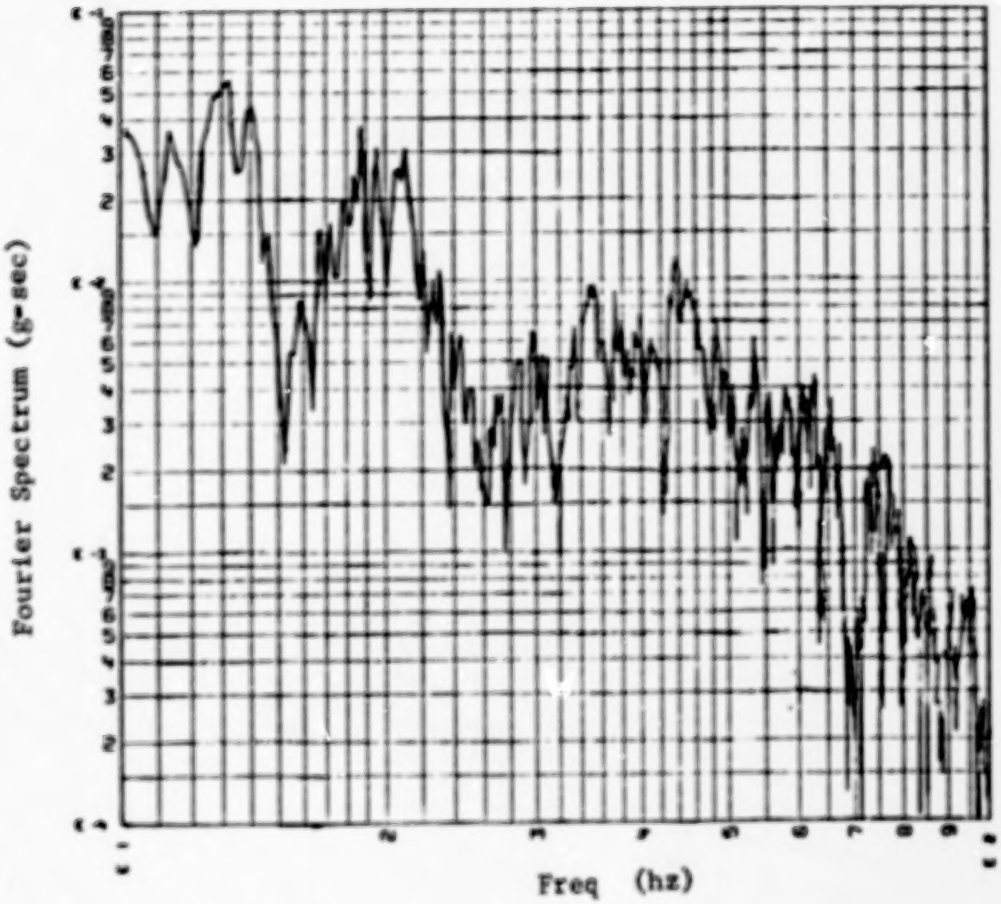

Figure 48. Fourier Spectrum of CM101A From E-4 Stage I Burnout (10-100 Hz)

from one flight to the next, the differences are quite evident.

In order to generate the interface accelerations using the impedance equations, the analytical models for Stage I burnout of all four boosters and the payloads were resurrected. Booster model information was used for the complex transfer and point admittance coefficient matrices and the payload data generated the necessary complex payload impedance matrices.

Since the structural configurations were the same for the boosters (with the exception of slight differences in propellant line dynamics), the only difference in model parameters from one flight vs another was related to structural weight (see Tables 1 through 3); the largest difference being in the residual Stage I slosh fuel at burnout. Fifty modes were used for each booster in the analysis set. All modes above 50 Hz were truncated since the frequency regime of interest was approximately 18 Hz, the frequency content of a typical Stage I burnout.

Tables 4 through 7 show a comparison of the modal frequencies for all longitudinal, pitch, roll and yaw modes. It is evident that in comparison the models vary only slightly in modal frequencies. The same is true for the eigenvectors used for the transfer characteristics.

The modal damping used for the booster model was perturbated a number of times to obtain what was felt to be optimum agreement with the first data spectra. Originally the booster damping chosen corresponded to that shown in Figure 49 which has been used in Titan loads analysis for some time. However, as stated before, the Stage I burnout is basically an 18 Hz event. The rise in the damping curve at

TABLE 1. LONGITUDINAL WEIGHT SUMMARY FOR BOOSTER STAGE I BURNOUT MODELS

Item	E-1 Wt. (N)	E-2 Wt. (N)	E-3 Wt. (N)	E-4 Wt. (N)
Centaur	1.580×10^5	1.576×10^5	1.576×10^5	1.570×10^5
Interstage Adapter	5.004×10^3	5.004×10^3	5.058×10^3	5.058×10^3
Fairing	3.205×10^4	3.205×10^4	3.205×10^4	3.205×10^4
Core (Struct)	9.963×10^4	9.963×10^4	9.963×10^4	9.963×10^4
Stage II Ox	1.900×10^5	1.921×10^5	1.913×10^5	1.910×10^5
Stage II Fuel	1.072×10^5	1.077×10^5	1.064×10^5	1.054×10^5
Stage I Ox	5.738×10^2	5.293×10^2	5.293×10^2	5.738×10^2
Stage I Fuel	1.066×10^4	1.108×10^4	2.584×10^3	3.679×10^3
Total	6.032×10^5	6.102×10^5	5.950×10^5	5.944×10^5

TABLE 2. LATERAL WEIGHT SUMMARY FOR BOOSTER STAGE I BURNOUT MODELS

Item	E-1 Wt. (N)	E-2 Wt. (N)	E-3 Wt. (N)	E-4 Wt. (N)
Centaur	1.585×10^5	1.578×10^5	1.578×10^5	1.574×10^5
Interstage Adapter	5.004×10^3	5.004×10^3	5.058×10^3	5.058×10^3
Fairing	3.205×10^4	3.205×10^4	3.205×10^4	3.205×10^4
Core (Struct)	9.962×10^4	9.962×10^4	9.962×10^4	9.962×10^4
Stage II Ox	1.900×10^5	1.921×10^5	1.912×10^5	1.910×10^5
Stage II Fuel	1.072×10^5	1.077×10^5	1.064×10^5	1.054×10^5
Stage I Ox	5.738×10^2	5.738×10^2	5.738×10^2	5.738×10^2
Stage I Fuel	1.066×10^4	1.107×10^4	2.580×10^3	3.679×10^3
Total	6.036×10^5	6.060×10^5	5.953×10^5	5.948×10^5

TABLE 3. SLOSH WEIGHT SUMMARY FOR BOOSTER STAGE I BURNOUT MODELS

Item	E-1 Slosh Wt. (N)	E-2 Slosh Wt. (N)	E-3 Slosh Wt. (N)	E-4 Slosh Wt. (N)
Centaur				
LO_2	1.432×10^4	1.432×10^4	1.432×10^4	1.432×10^4
LH_2	2.153×10^3	2.153×10^3	2.153×10^3	2.153×10^3
Stage II				
Ox	3.674×10^4	3.674×10^4	3.674×10^4	3.674×10^4
Fuel	2.285×10^4	2.285×10^4	2.285×10^4	2.285×10^4
Stage I				
Ox	8.896×10^0	8.896×10^0	8.896×10^0	8.896×10^0
Fuel	7.967×10^3	8.380×10^3	1.957×10^3	2.576×10^3

TABLE 4. LONGITUDINAL MODAL FREQUENCIES FOR STAGE I BURNOUT BOOSTER MODELS

Mode No.	E-1 Freq. (Hz)	E-2 Freq. (Hz)	E-3 Freq. (Hz)	E-4 Freq. (Hz)
1	0.0	0.0	0.0	0.0
2	18.1	18.1	18.4	18.4
3	21.9	21.8	22.4	22.3
4	26.8	26.7	27.2	27.2
5	31.5	31.5	31.6	31.5
6	37.4	37.4	37.4	37.4
7	44.0	44.0	44.0	44.1

TABLE 5. ROLL MODAL FREQUENCIES FOR STAGE I BURNOUT BOOSTER MODELS

Mode No.	E-1 Freq. (Hz)	E-2 Freq. (Hz)	E-3 Freq. (Hz)	E-4 Freq. (Hz)
1	0.0	0.0	0.0	0.0
2	13.3	13.3	13.3	13.3
3	15.9	15.9	15.9	15.9
4	34.4	34.4	34.4	34.4
5	38.1	38.1	38.1	38.1

TABLE 6. PITCH MODAL FREQUENCIES FOR STAGE I BURNOUT BOOSTER MODELS

Mode No.	E-1 Freq. (Hz)	E-2 Freq. (Hz)	E-3 Freq. (Hz)	E-4 Freq. (Hz)
1	0.0	0.0	0.0	0.0
2	0.0	0.0	0.0	0.0
3	0.7	0.7	0.8	0.9
4	0.9	0.9	0.9	0.9
5	1.0	1.0	1.0	1.0
6	1.0	1.0	1.0	1.0
7	1.2	1.2	1.2	1.2
8	3.1	3.1	3.1	3.1
9	6.5	6.5	6.5	6.5
10	10.5	10.5	10.4	10.5
11	13.4	13.4	13.4	13.4
12	16.0	16.0	16.0	16.0
13	18.2	18.1	18.2	18.2
14	28.7	28.7	28.7	28.7
15	34.9	34.9	35.0	35.0
16	36.7	36.7	36.8	36.8
17	40.0	40.0	40.1	40.1
18	46.2	46.5	46.2	46.2
19	48.1	48.0	48.0	48.0

TABLE 7. YAW MODAL FREQUENCIES FOR STAGE I BURNOUT BOOSTER MODELS

Mode No.	E-1 Freq. (Hz)	E-2 Freq. (Hz)	E-3 Freq. (Hz)	E-4 Freq. (Hz)
1	0.0	0.0	0.0	0.0
2	0.0	0.0	0.0	0.0
3	0.7	0.7	0.8	0.9
4	0.9	0.9	0.9	0.9
5	1.0	1.0	1.0	1.0
6	1.0	1.0	1.0	1.0
7	1.2	1.2	1.2	1.2
8	3.1	3.1	3.1	3.1
9	6.5	6.5	6.5	6.5
10	10.5	10.5	10.5	10.5
11	13.4	13.4	13.4	13.4
12	16.0	16.0	16.0	16.0
13	18.2	18.2	18.2	18.2
14	28.7	28.7	28.7	28.7
15	34.9	34.9	35.0	35.0
16	36.9	36.9	37.0	37.0
17	40.0	40.0	40.1	40.1
18	46.2	46.5	46.2	46.2
19	48.1	48.0	48.0	48.0

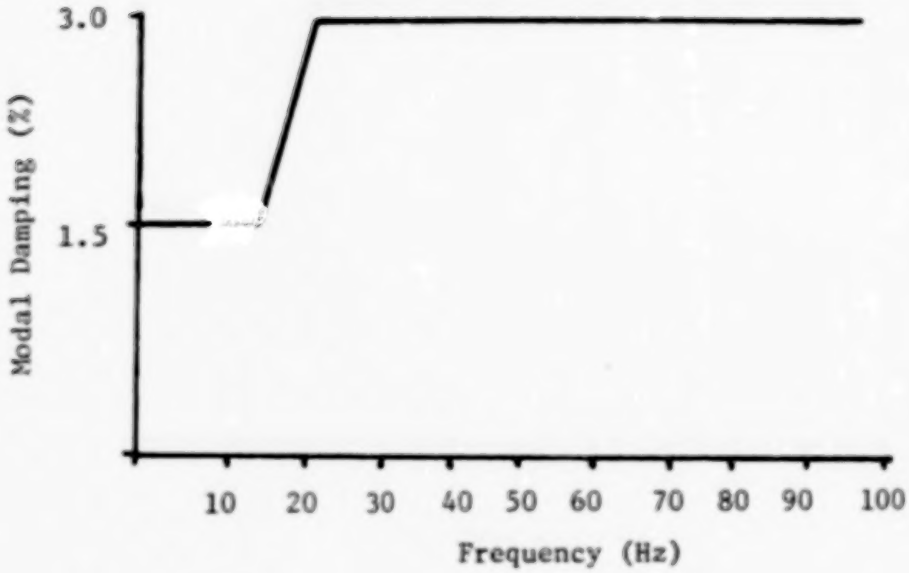

Figure 49. Titan Modal Damping Curve

approximately this frequency appeared to attenuate the response to an extreme degree. Therefore, the optimum modal damping for good comparison to flight data spectra of measurement CM101A was chosen as 1.5% for all modes. Since there appears to be very little justification for using the curve in Figure 49 aside from precedent, this assumption seems valid.

The payload models varied understandably from one flight to another with the exception of the E-3 and E-4 flights which were, of course, both Viking payloads. A detailed breakdown of each payload's dynamic characteristics would be beyond the scope of the intent of this report. Instead, frequency domain plots of the impedances for each payload in the longitudinal direction are shown in Figures 50 through 53. Table 8 gives total weights and centers of gravity for comparisons. The impedance shown are based on mode shapes truncated above 50 Hz and include the individual payload damping. For the Viking models, the damping used was based on coupled damping from modal coupling discarding the off-diagonal terms. Helios assumed a damping curve as a function of frequency identical to that shown previously in Figure 49, and the VDS damping was obtained directly from the modal survey of the flight structure.

The Titan data analysis was broken into two parts. One part of the effort demonstrated the solution for the payload interface accelerations using a computer program written to solve equation (28). For each of the four flights, the Fourier spectra of the engine pressure time histories were used to drive the models resulting in the interface acceleration spectra in the longitudinal direction. These calculated Fourier response spectra are shown in Figures 54 through 57.

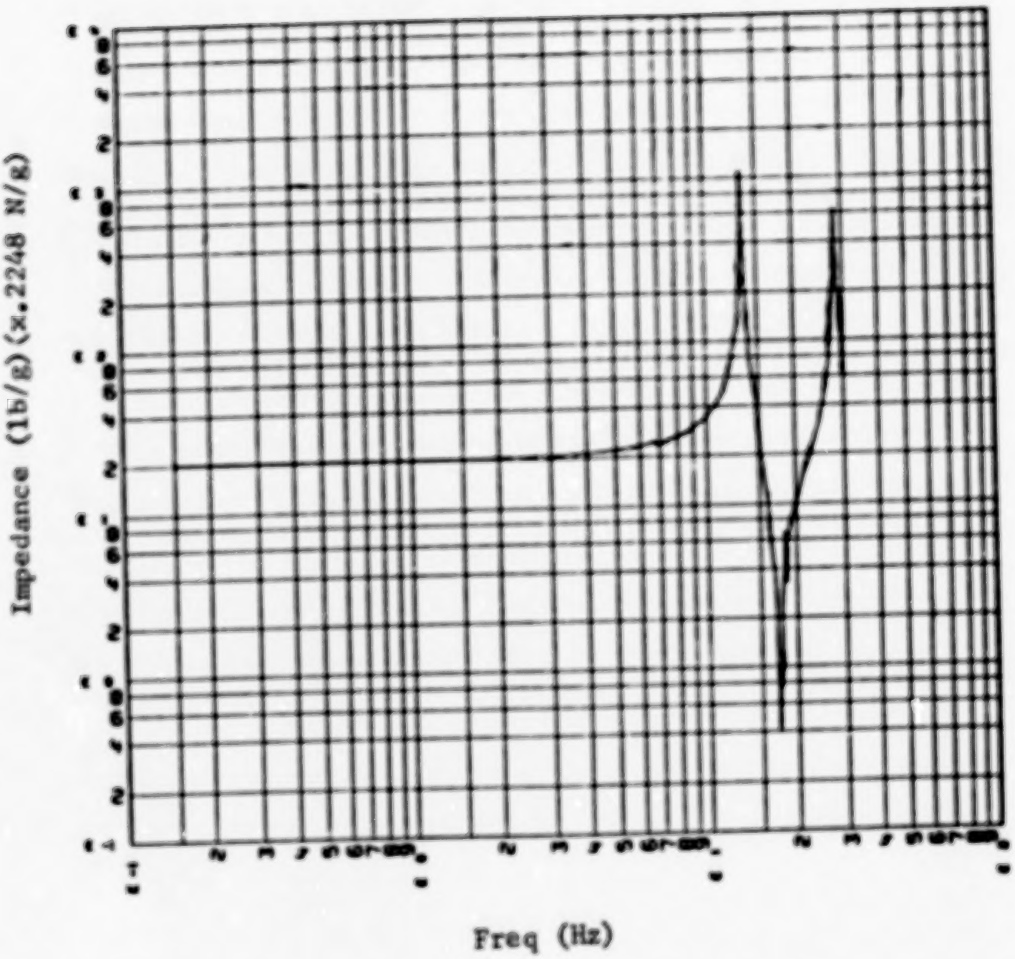

Figure 50. Longitudinal Payload Impedance For VDS.

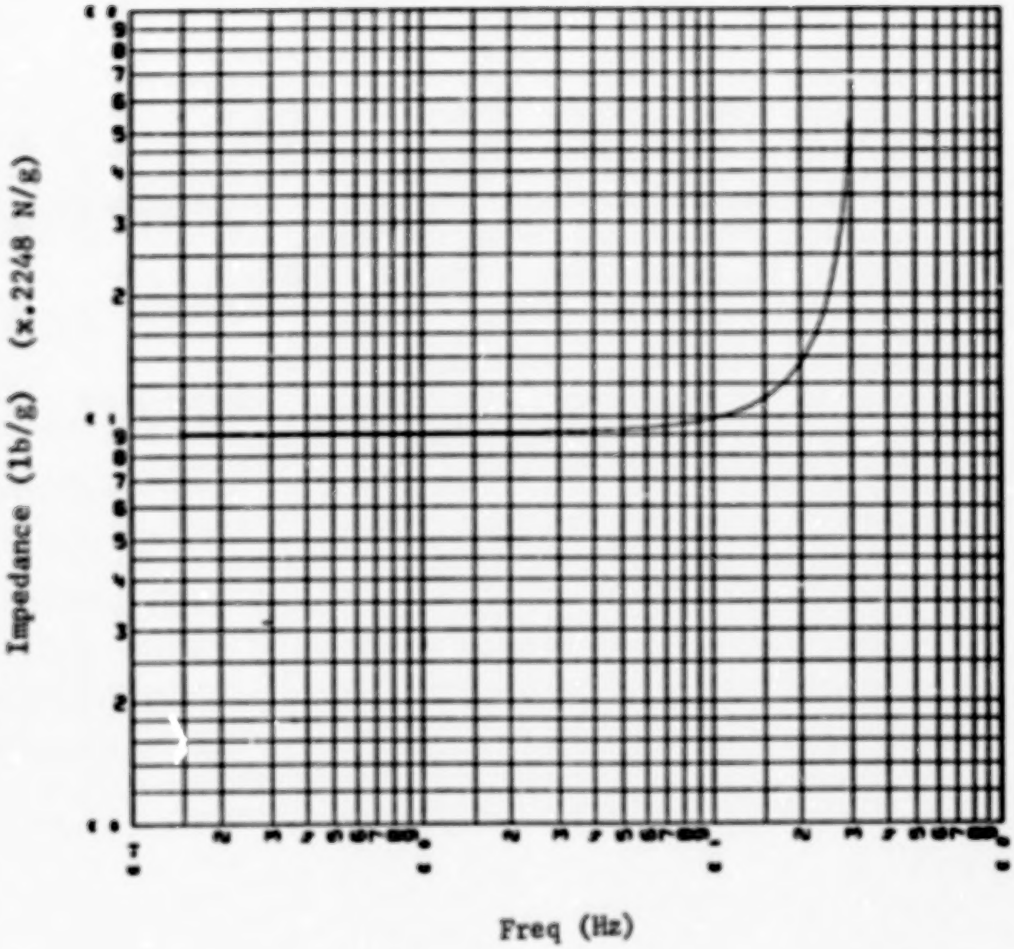

Figure 51. Longitudinal Payload Impedance For Helios.

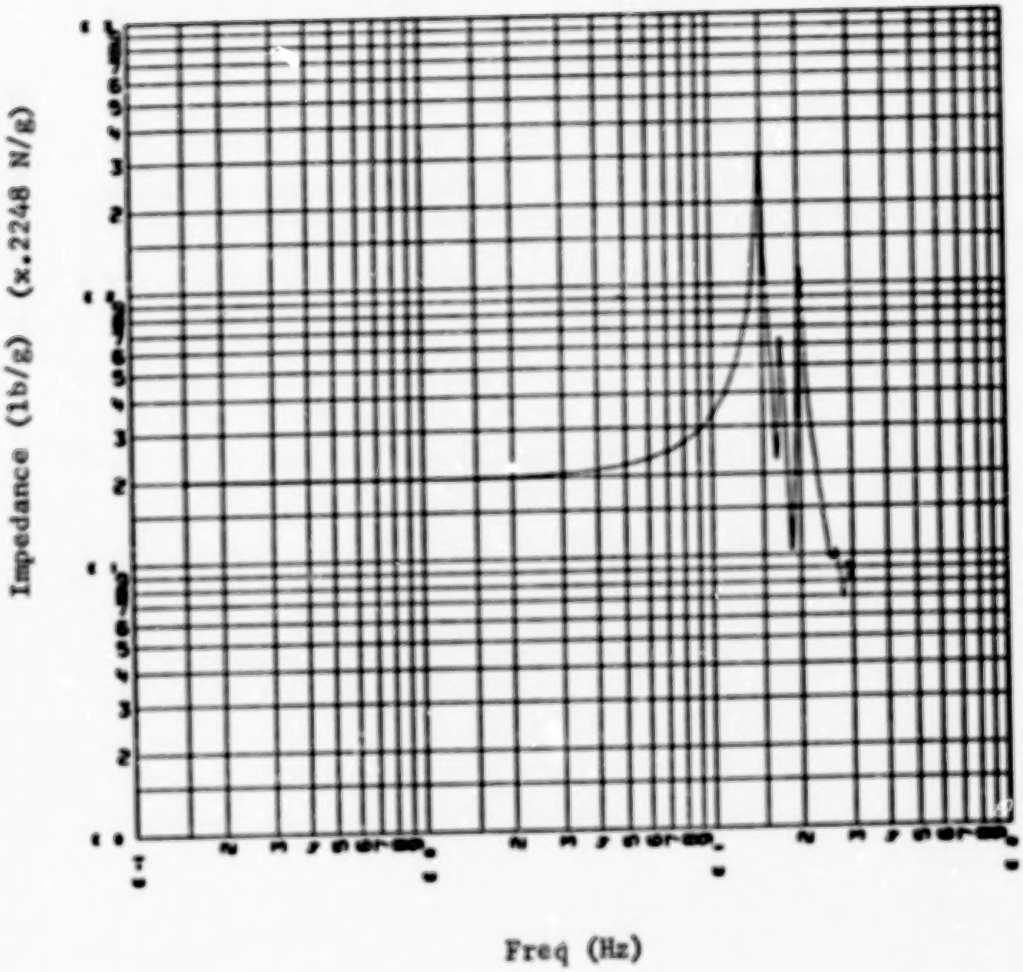

Figure 52. Longitudinal Payload Impedance For Viking A.

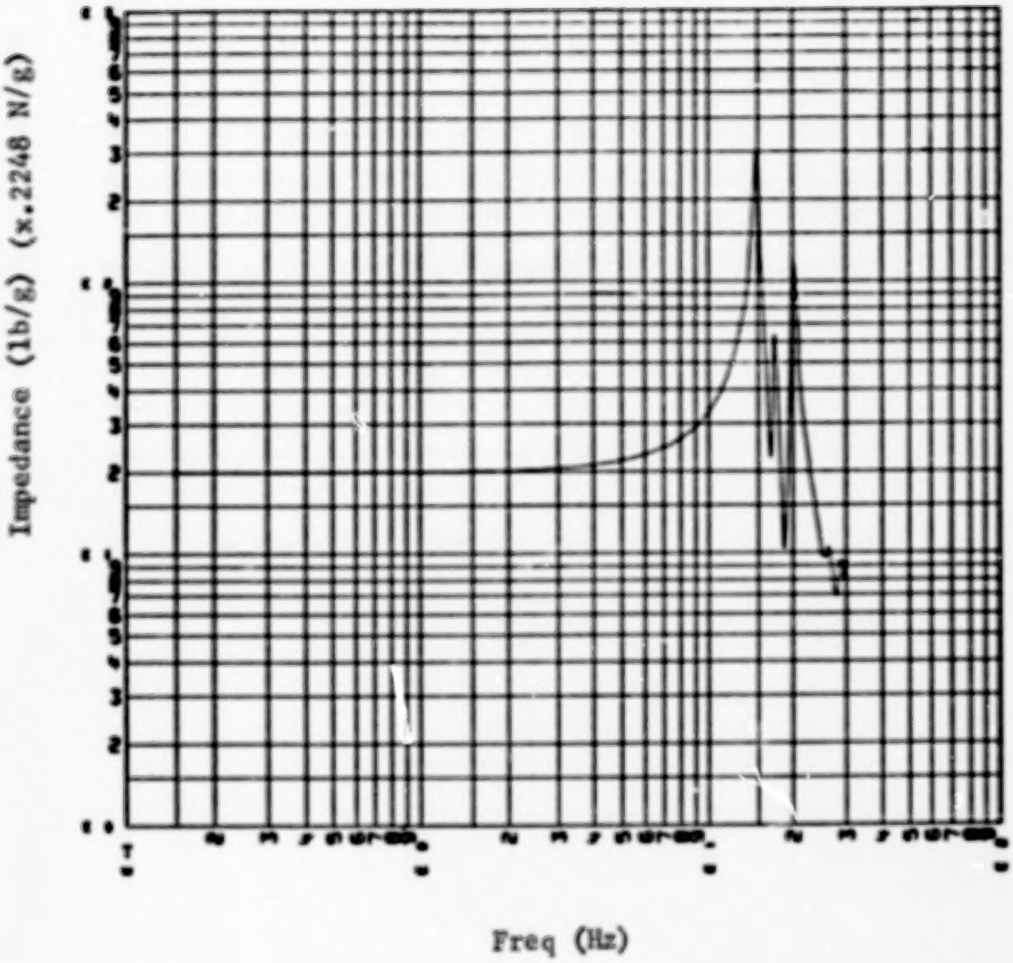

Figure 53. Longitudinal Payload Impedance For Viking B.

CONTENTS

	Page	
SUMMARY	1	1/A13
INTRODUCTION	2	1/A14
SYMBOLS	4	1/B2
IMPEDANCE TECHNIQUE	6	1/B4
Development of the Equations of Motion	6	1/B4
Analysis of the Titan Data	31	1/D4
Applications to STS Payload	93	2/A11
DISCUSSION OF RESULTS	122	2/C13
CONCLUSIONS	126	2/D3
APPENDICES	127	2/D4
A	127	2/D4
B	131	2/D8
REFERENCES	135	2/D12

TABLE 8. COMPARISON OF PAYLOAD TOTAL WEIGHTS AND C.G. LOCATIONS

Payload	Total Weight (N)	C.G. Location* X (M)	Y (M)	Z (M)
VDS	3.48×10^{4}	3.64×10^{0}	3.35×10^{-2}	-1.52×10^{-2}
Helios	1.56×10^{4}	2.13×10^{0}	-3.95×10^{-3}	-3.13×10^{-4}
Viking A	3.42×10^{4}	3.33×10^{0}	2.08×10^{-2}	-1.83×10^{-2}
Viking B	3.42×10^{4}	3.33×10^{0}	2.08×10^{-2}	-1.83×10^{-2}

* C.G. locations are referenced to the booster interface with a coordinate system shown below:

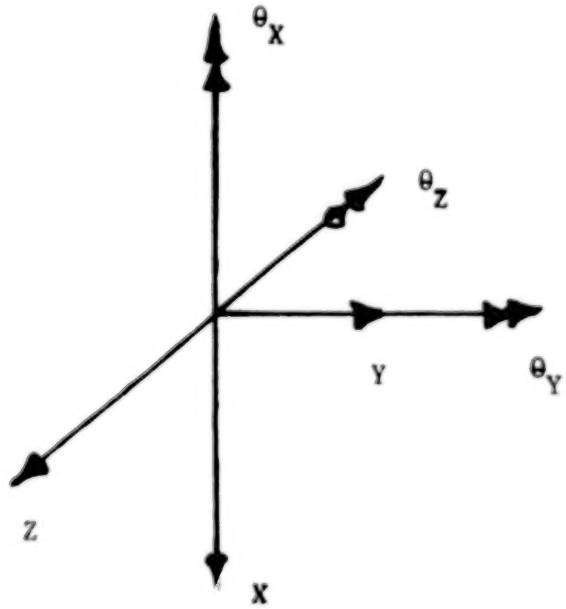

AFT

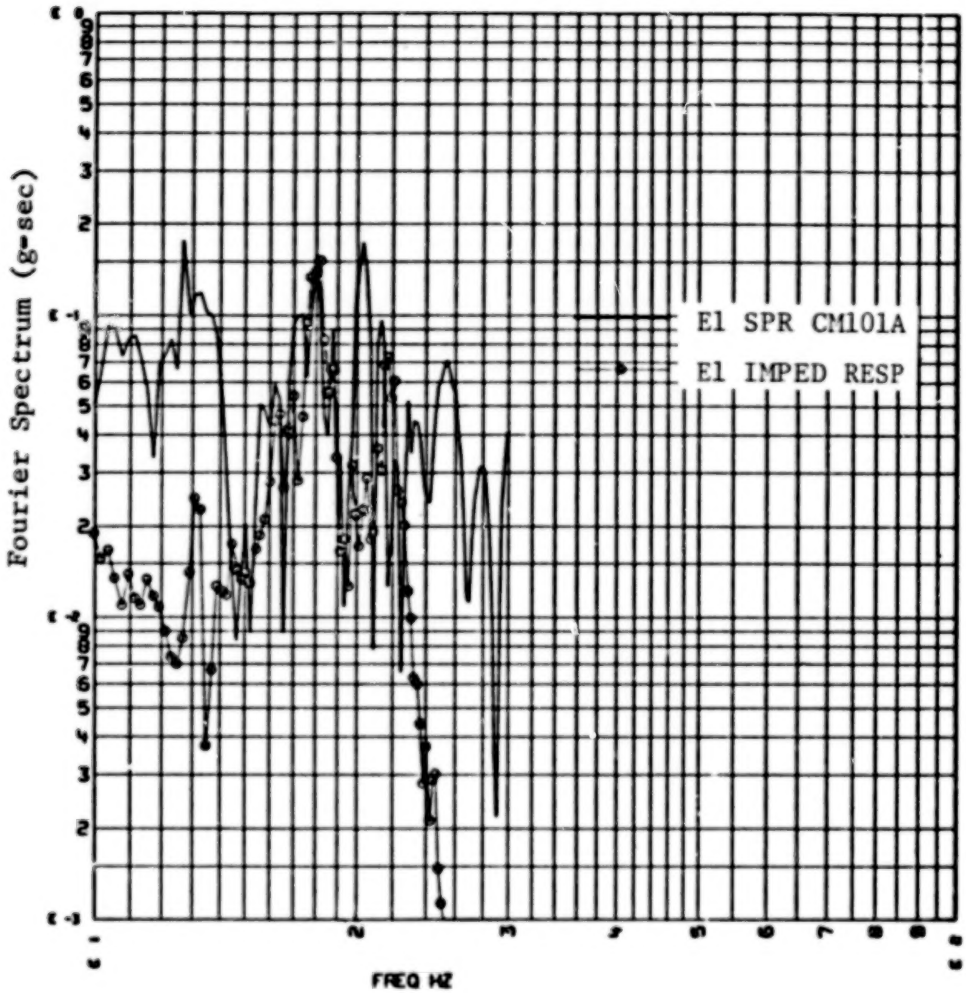

Figure 54. Comparison of CM101A Flight Data Spectrum With Impedance Analytical Predictions for E-1 Stage I Burnout

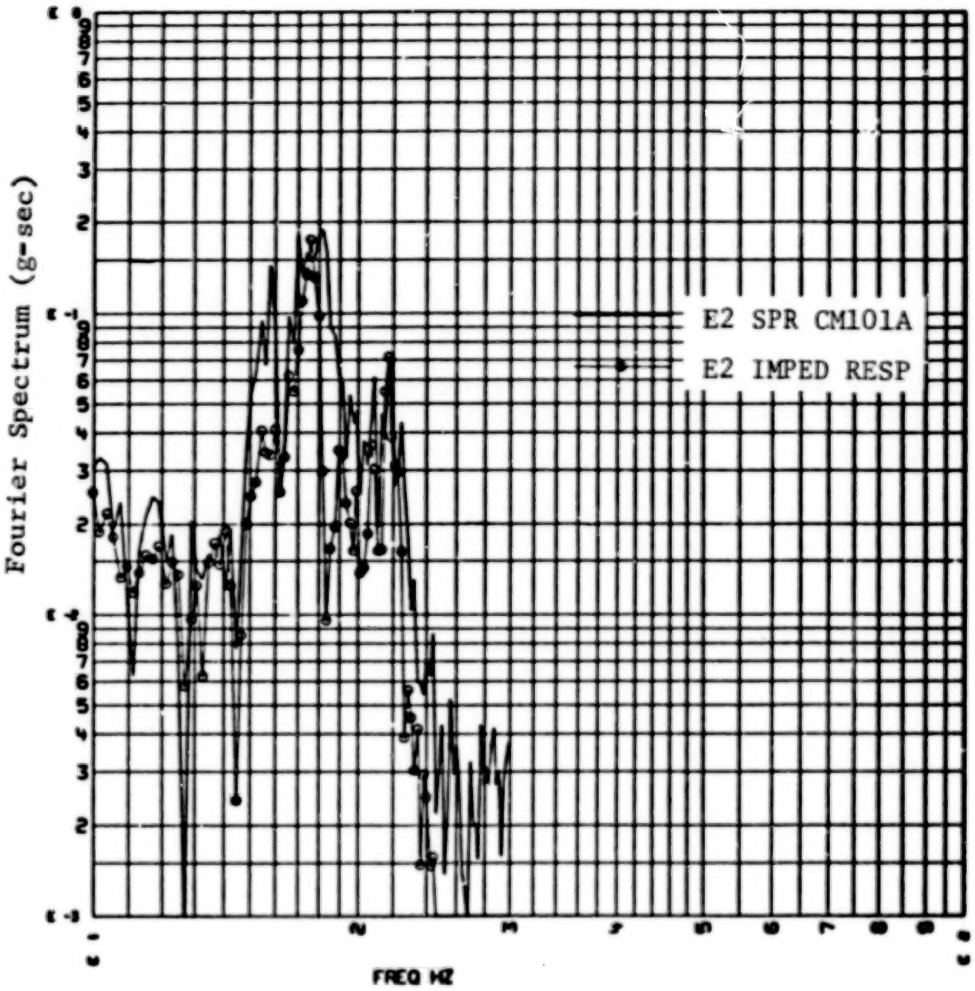

Figure 55. Comparison of CM101A Flight Data Spectrum With Impedance Analytical Predictions for E-2 Stage I Burnout

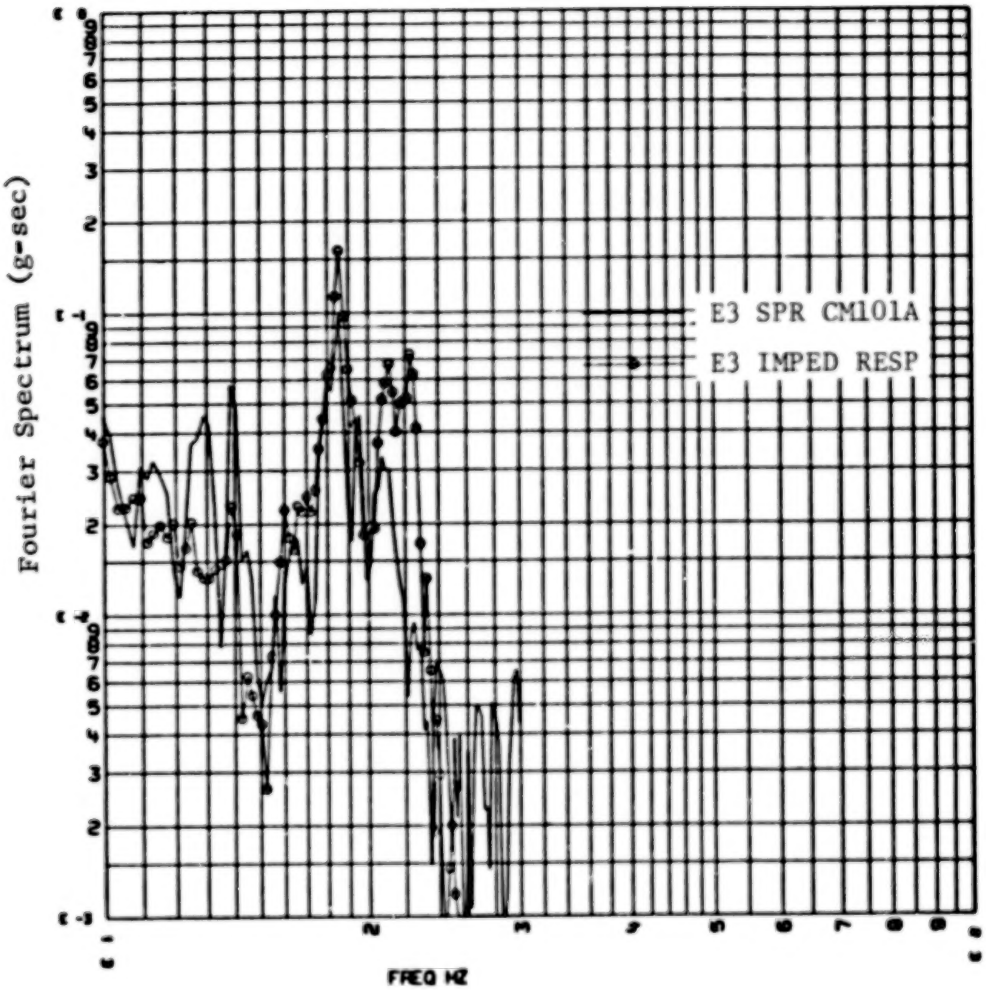

Figure 56. Comparison of CM101A Flight Data Spectrum With Impedance Analytical Prediction for E-3 Stage I Burnout

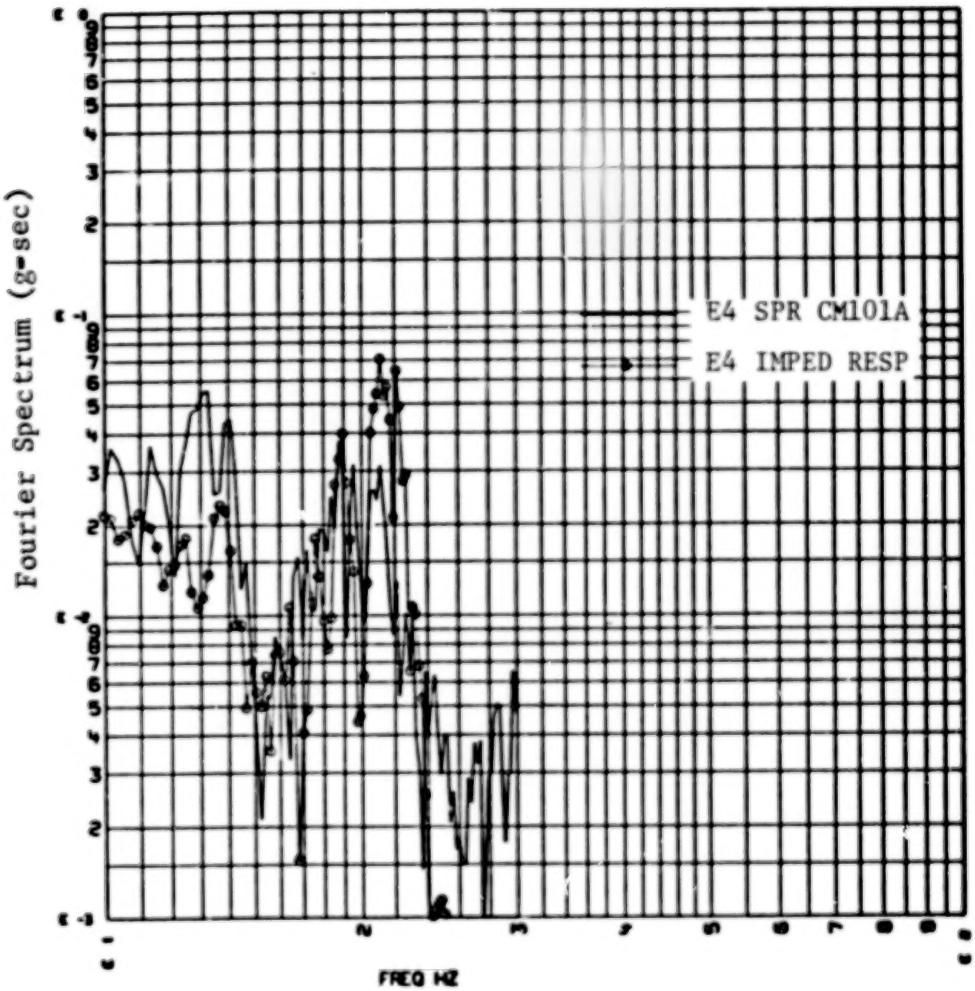

Figure 57. Comparison of CM101A Flight Data Spectrum With Impedance Analytical Predictions for E-4 Stage I Burnout

The second part of the analysis involved using the flight data to solve equation (29). The Helios flight, E-2, was chosen as the basis for the original interface data from which the low frequency environments were predicted. Most of the modes of the Helios payload can be considered to be longitudinal in nature based on information from previous work. For this reason, most of the response shown in the CM101A measurement during the E-2 flight should be due to longitudinal motion and very little to lateral and bending mode feedback. A separate computer program was written to solve equation (29) and the results for the predicted Viking and VDS longitudinal environments are shown in Figures 58 and 59.

As expected the first obvious problem encountered in using the CM101A data pertained to its location. The models used for the generation of the booster admittances, i.e., in this case the transfer characteristics of the coupled Centaur and two stages of the Titan III, and the structural response measured by CM101A were inconsistent. CM101A was physically located on a forward equipment truss at the outer circumference of the Centaur structure. In that location, the accelerometer picked up not only the desired longitudinal vehicle accelerations but any bending mode responses as well as local secondary structure responses.

One other model/flight data correlation problem encountered was due to the Titan second stage ignition. Close comparisons of engine thrust time histories and accelerometer time histories in Figures 13 through 24 show a response on the accelerometer that does not appear on the pressure time histories. This response occurs after the first stage shutdown, i.e., where the acceleration bagins to pick up a dc level, and contains 20 to 22 Hz frequency oscillations.

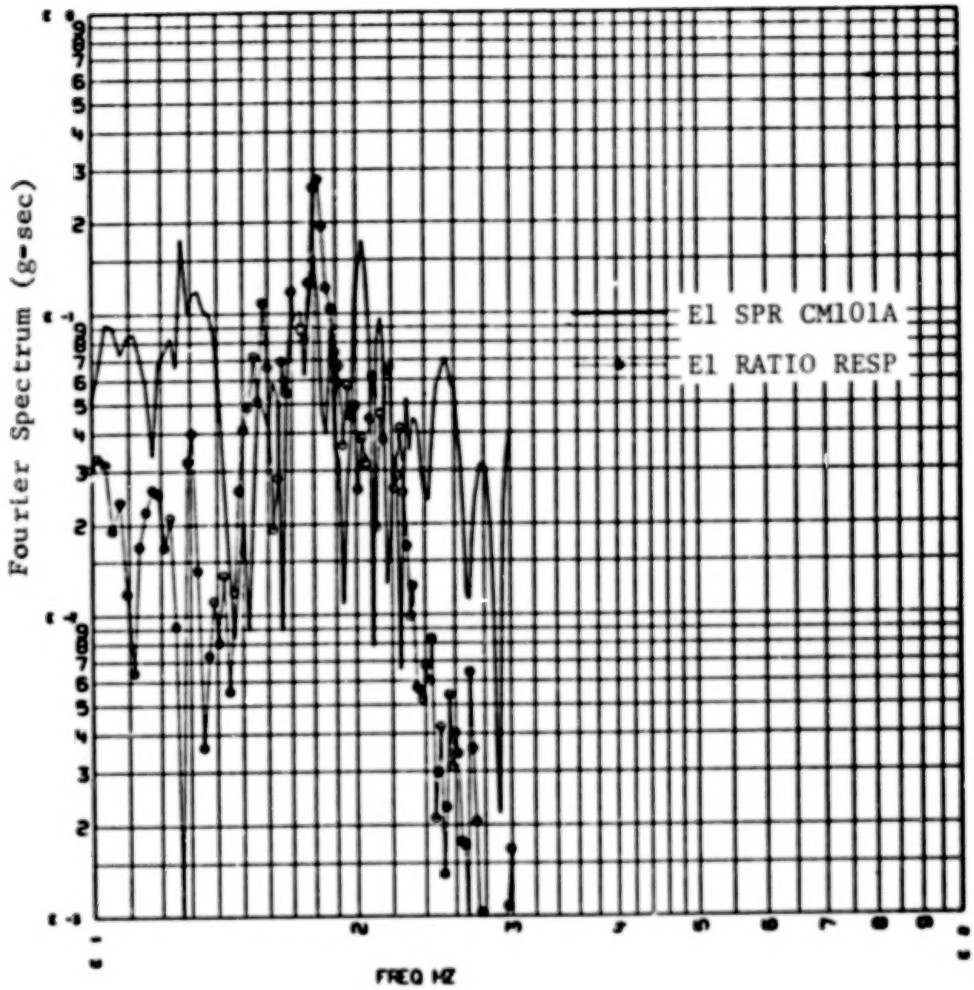

Figure 58. Comparison of CM101A E-1 Spectrum With Impedance Ratio Response From E-2

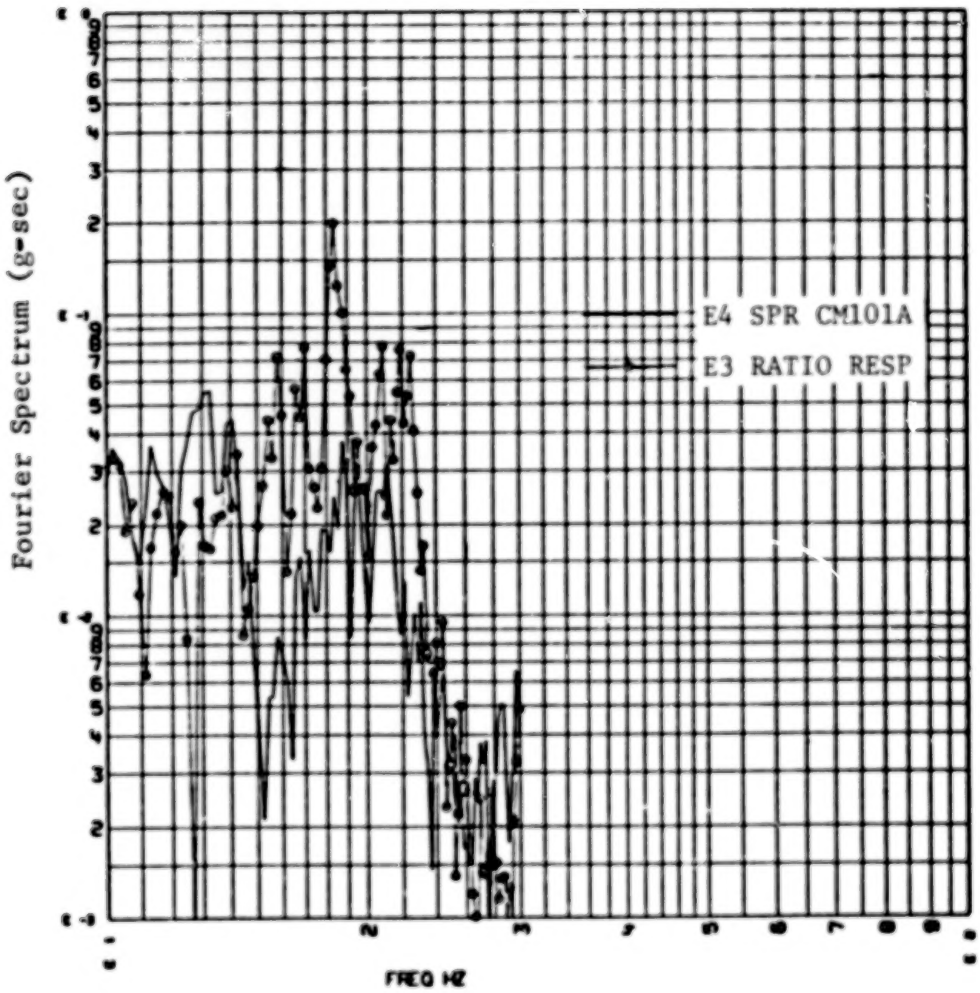

Figure 59. Comparison of CM101A E-3 Spectrum With Impedance Ratio Response From E-2.

The Stage I burnout models, however, have neither the true modeling of the physical separation of the first and second stages nor the forcing function corresponding to the second stage fire. For these reasons close comparisons of flight data and analytical predictions are not expected above the 18 Hz first stage burnout. It should also be pointed out that the second stage ignition problem will be different from one flight to another. For this reason in particular, the frequency content of the spectra will be different also.

However, even with these discrepancies, the correlations of flight data and analytical prediction are quite good (Figures 54 through 57). For the desired mode of response (approximately 18 Hz), the technique appears to correlate in amplitude and bandwidth. With proper signal conditioning and modeling the correlation at the other frequencies can be improved. These points are important for consideration of a payload user's guide.

Application to STS Payload

As a further demonstration of the impedance technique the second phase of the analytical effort was directed at predicting the low frequency environment for an existing STS payload. The primary objective of this analysis was to compare results with other current environmental predictions from state-of-the-art techniques. It is hoped that the results of these predictions can then be used for comparisons with flight measured data from the development flights.

The models used for this set of analyses were chosen to be consistent with those used for the loads cycles done by the STS project. They were obtained through LRC and were comprised of eigenvalues and eigenvectors for the STS finite element model of the liftoff and landing configurations. Two hundred eigenvectors were used for each configuration which included the models of two of the three payloads in the payload bay for this flight, the DFI and SP. All modes for each loads case were assumed to have a modal damping ratio of 1%.

The third payload in the bay, the Long Duration Exposure Facility (LDEF), was chosen as the payload for these analyses. Forty eigenvalues and eigenvectors were again furnished by LRC. The discrete mass matrix for the LDEF, necessary for the generation of the inertial coupling coefficients matrix on the right-hand side of equation (22) was not available and had to be generated from discrete model data with in-house finite element routines (see Figure 60). Orthogonality checks were calculated to ensure that the modes and regenerated mass matrix were consistent. Like the booster models, the LDEF modes were assumed to have 1% damping throughout.

The agreed upon flight events for analysis were liftoff and landing. The liftoff event analyzed was defined as a

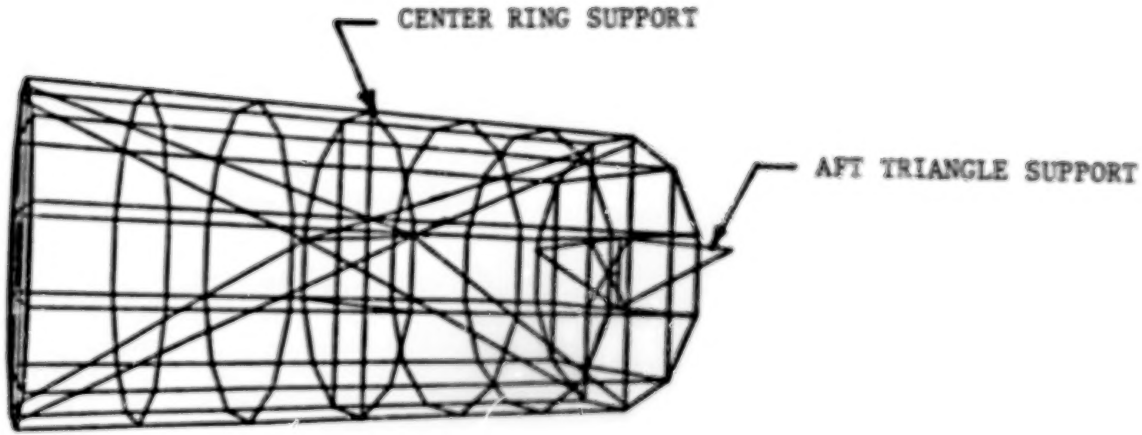

Figure 60. Finite Element Representation of LDEF.

"high performance fast timing" engine thrust with a mismatch between right and left SRBs. The SRB mismatch in this case was 0.098 sec.

A total of 62 discrete forcing functions were used to drive the analytical model for liftoff. Each defined time history was 10.0 sec in length. To obtain the Fourier spectrum of each force, they were first digitized, i.e., linearly interpolated, at 102.4 samples per second. This resulted in a total number of samples of 1024 with a Nyquist of approximately 50 Hz. The same Tukey window discussed in the previous sections was used for the liftoff forcing functions. Representative Fourier spectra of these forces were plotted and are shown in Appendix A.

The spectral results of the impedance predictions for the landing event are shown in Figures 61 through 66. These plots show the frequency bandwidths of maximum and minimum interface acceleration for the LDEF during the LP501R liftoff event. For a check with previous predictions, the complex Fourier spectra were inverse transformed to obtain a time history for amplitude and frequency content comparisons. The inverse Fourier transform time histories are presented in Figures 67 through 72. Shown also on the plots are the corresponding peak accelerations resulting from a time domain analysis. Corresponding, Z, or pitch, responses for the aft end of the LDEF were not available for comparison.

The Tukey window effect on the resulting time histories is best shown in Figure 67 which is the longitudinal acceleration at a forward LDEF attach point. Because of the window, this response begins and ends at approximately zero amplitude. However, since this windowing technique of signal conditioning does not alter the signal in the remaining areas, its effect can be ignored.

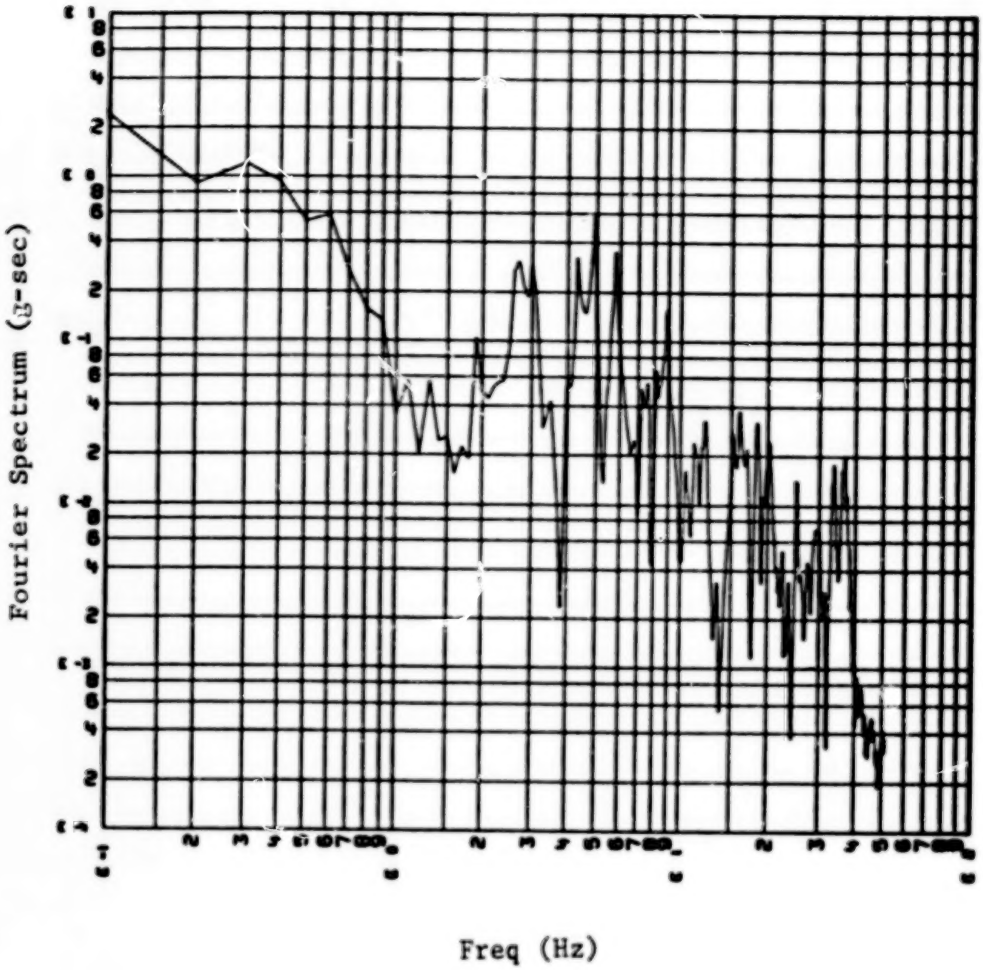

Figure 61. Fourier Spectrum of X Response At Forward Attach Point Right Hand Side For Lift-Off.

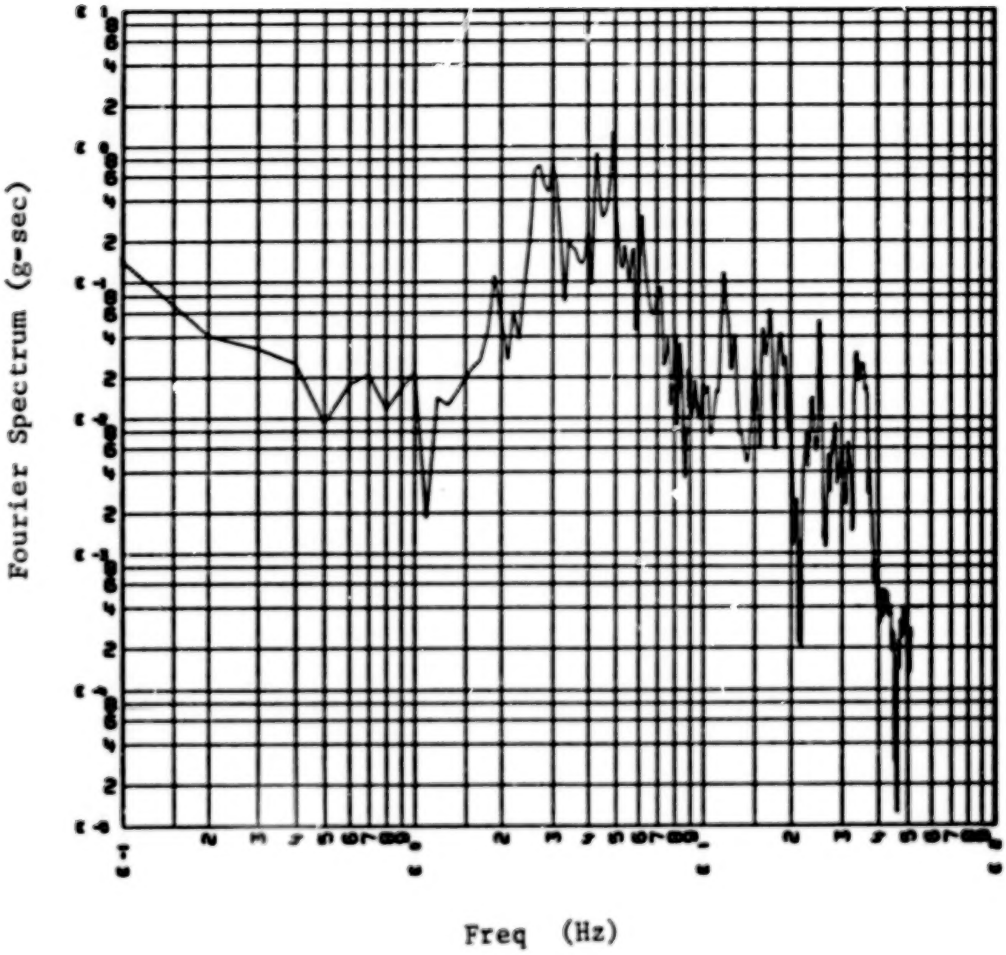

Figure 62. Fourier Spectrum of Z Response At Forward Attach Point Right Hand Side For Lift-Off.

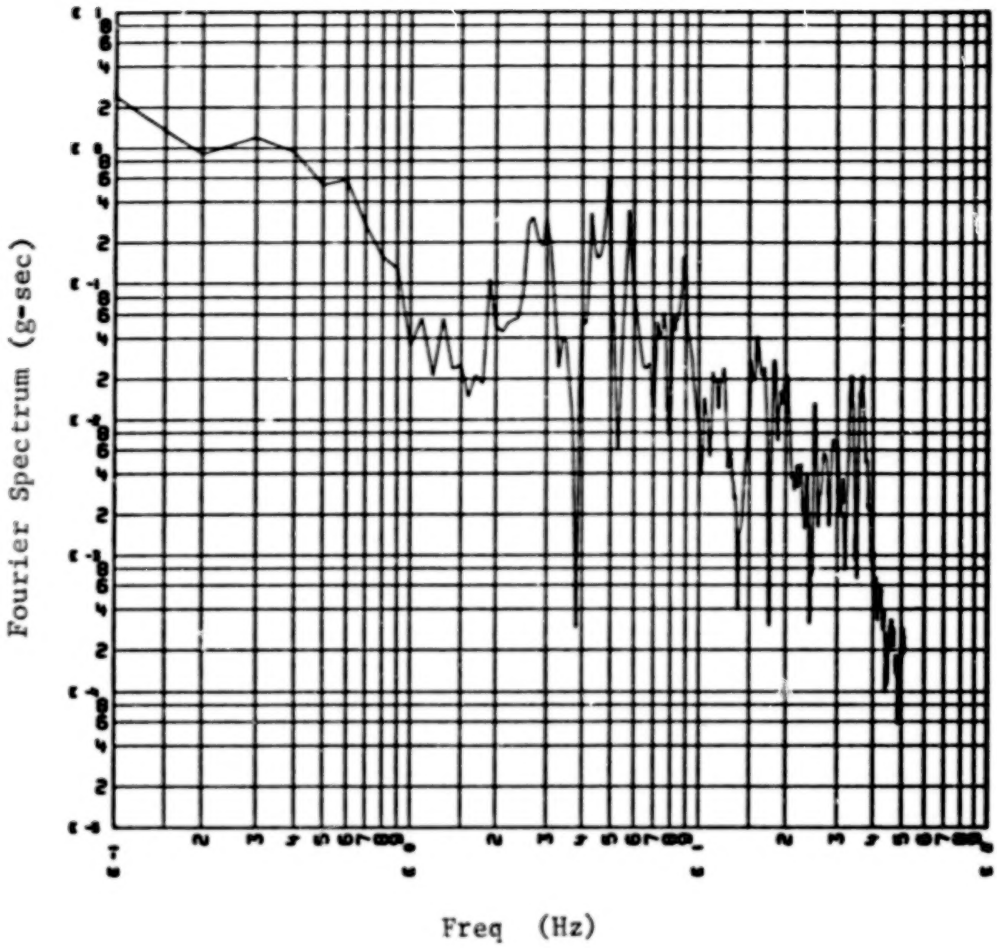

Figure 63. Fourier Spectrum of X Response At Forward Attach Point Left Hand Side For Lift-Off.

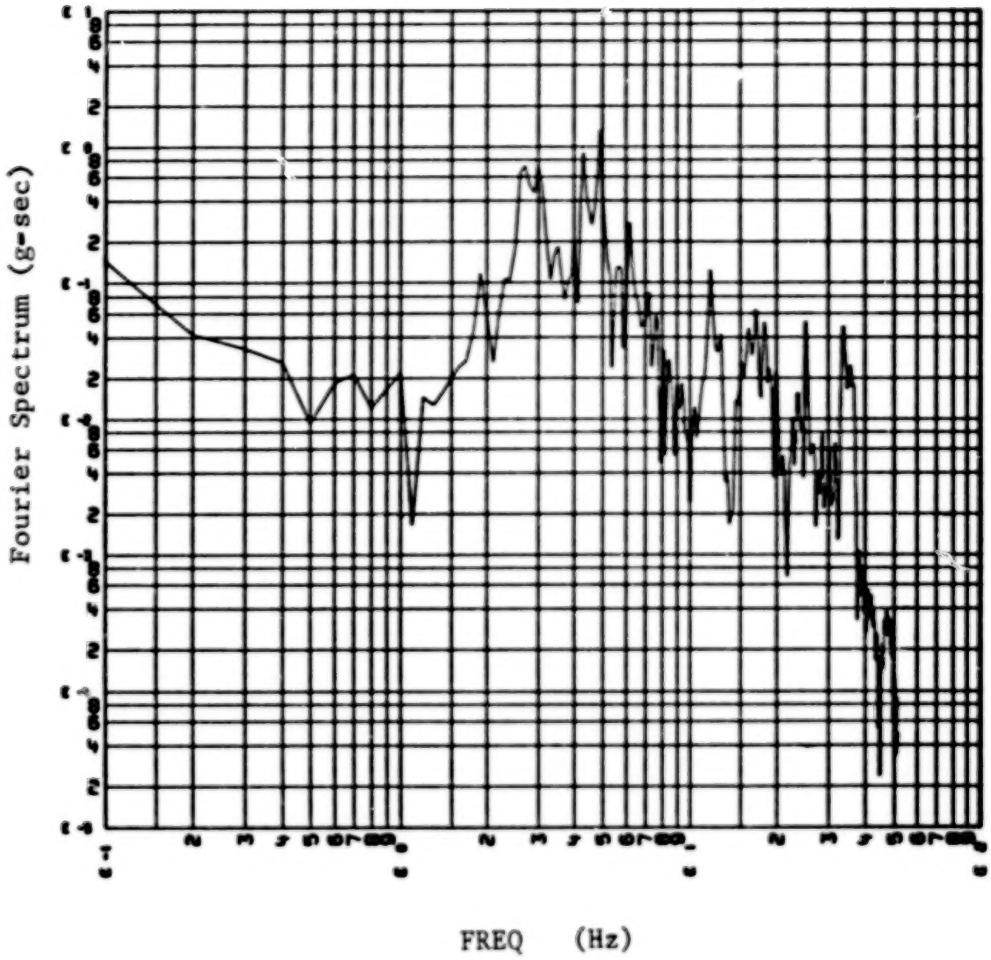

Figure 64. Fourier Spectrum of Z Response At Forward Attach Point Left Hand Side For Lift-Off.

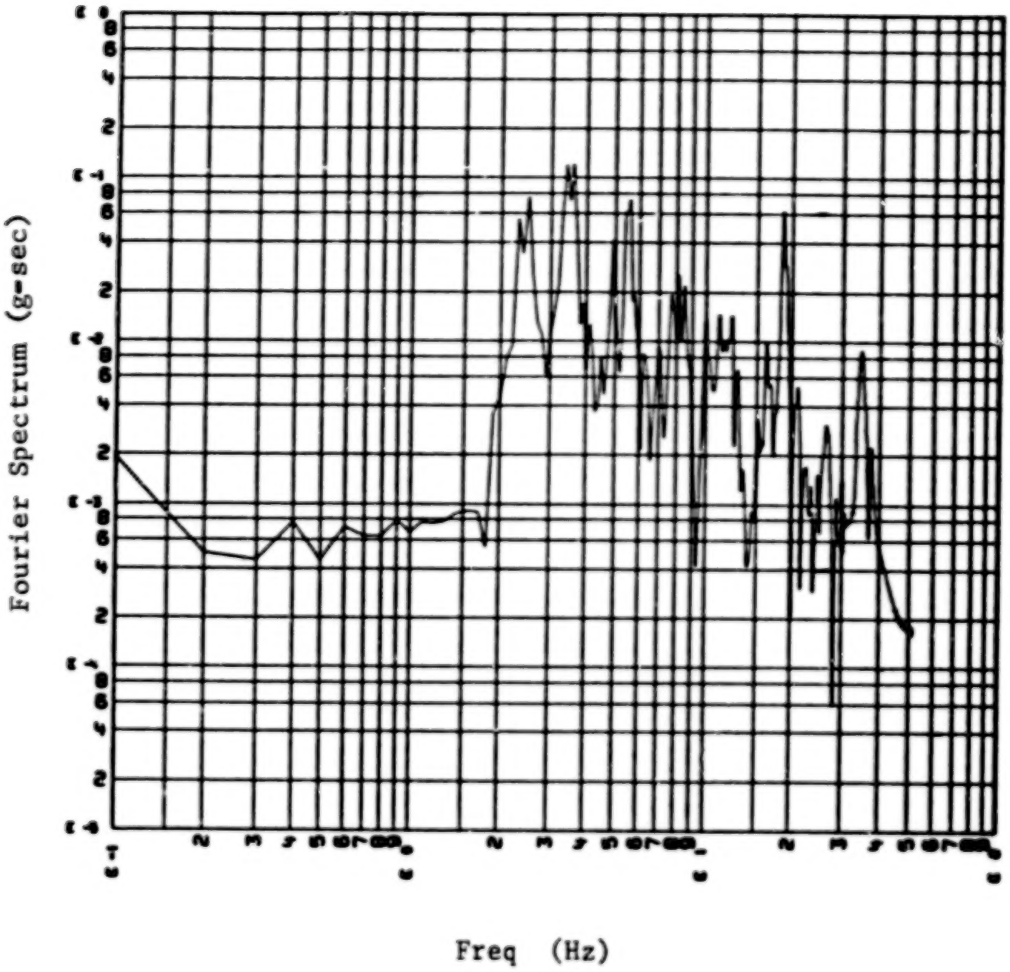

Figure 65. Fourier Spectrum of KEEL Response
For Lift-Off.

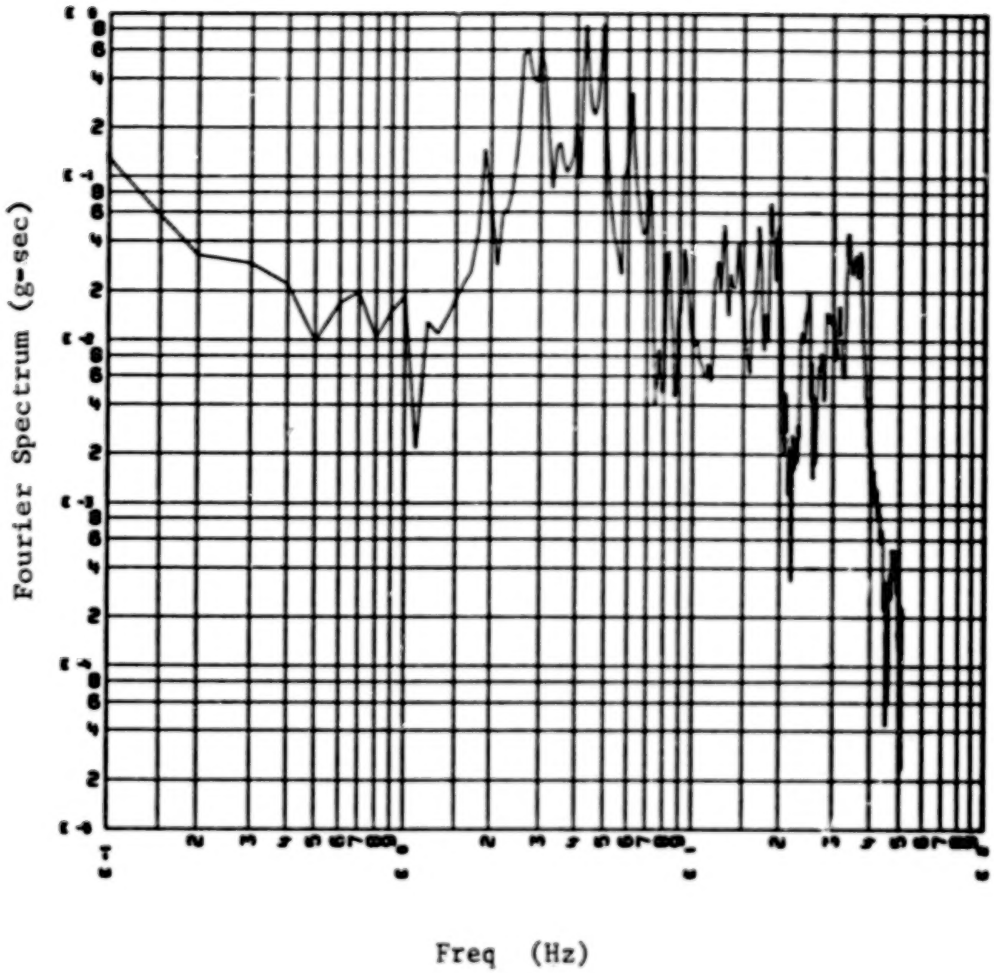

Figure 66. Fourier Spectrum of Aft Z Response For Lift-Off.

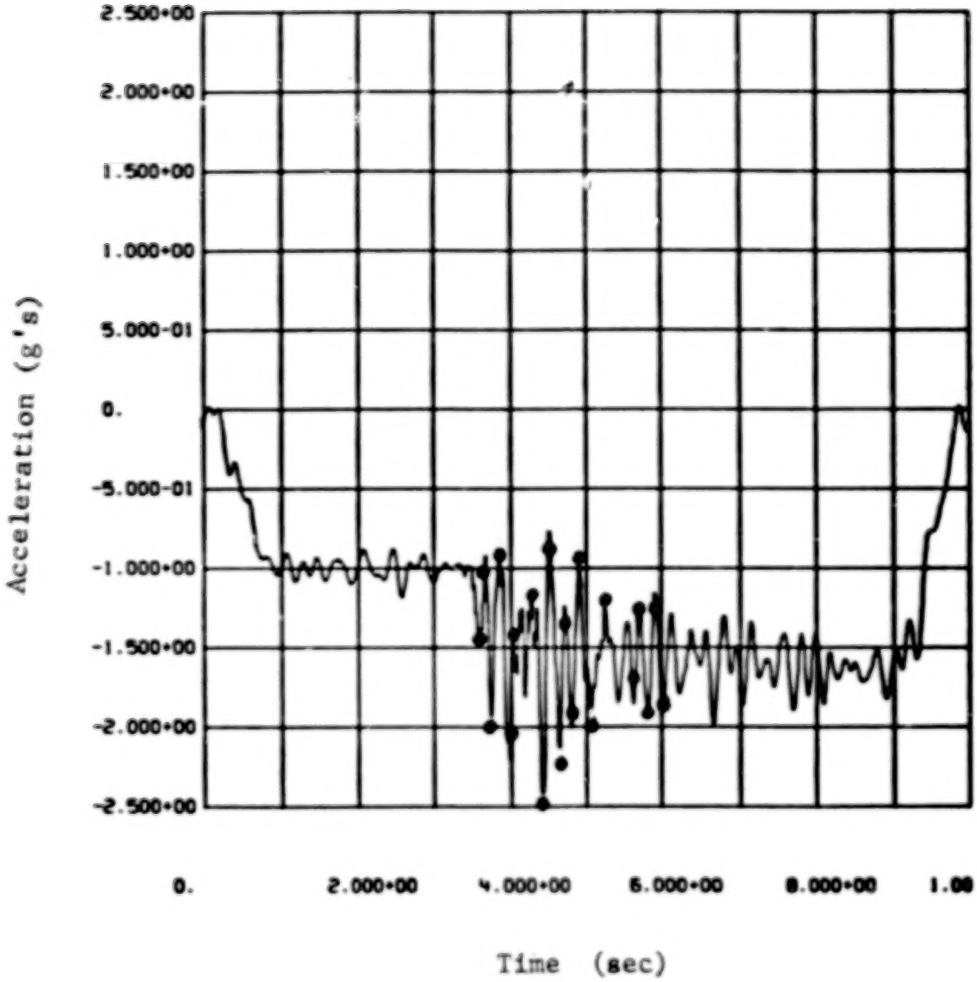

Figure 67. Response X Forward Attach Right Hand Side For Lift-Off.

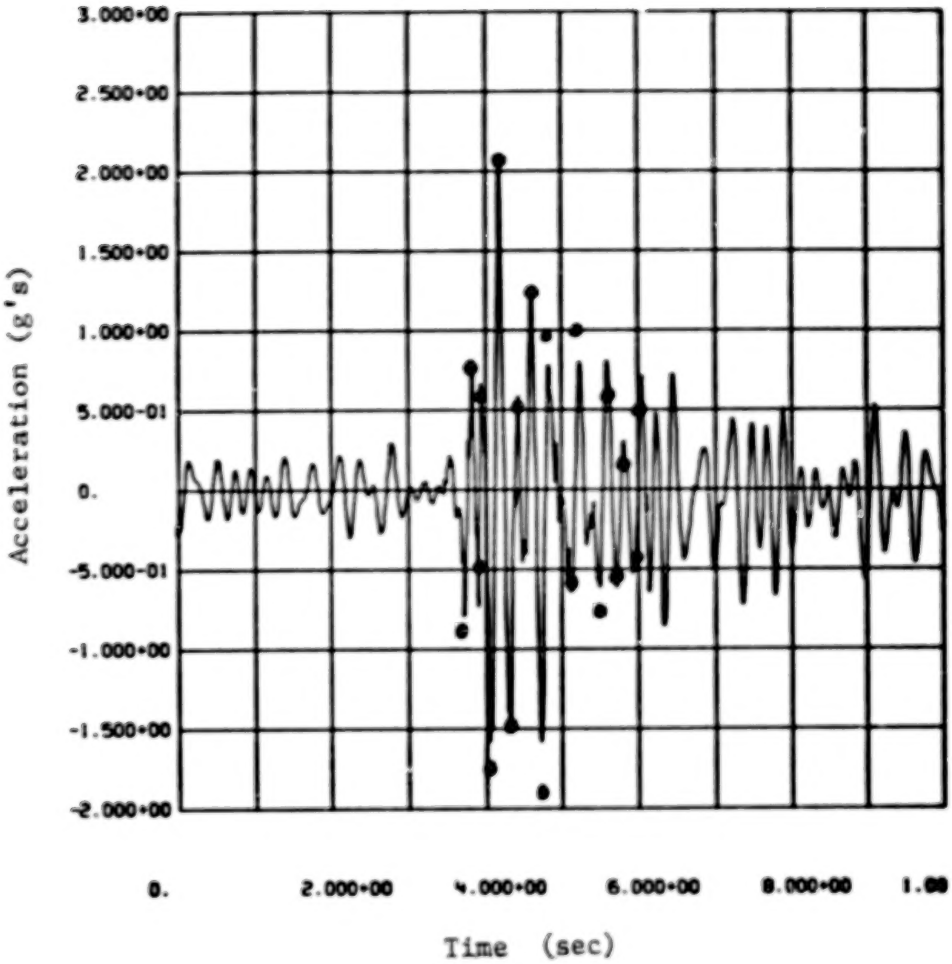

Figure 68. Response Z Forward Attach Right Hand Side For Lift-Off.

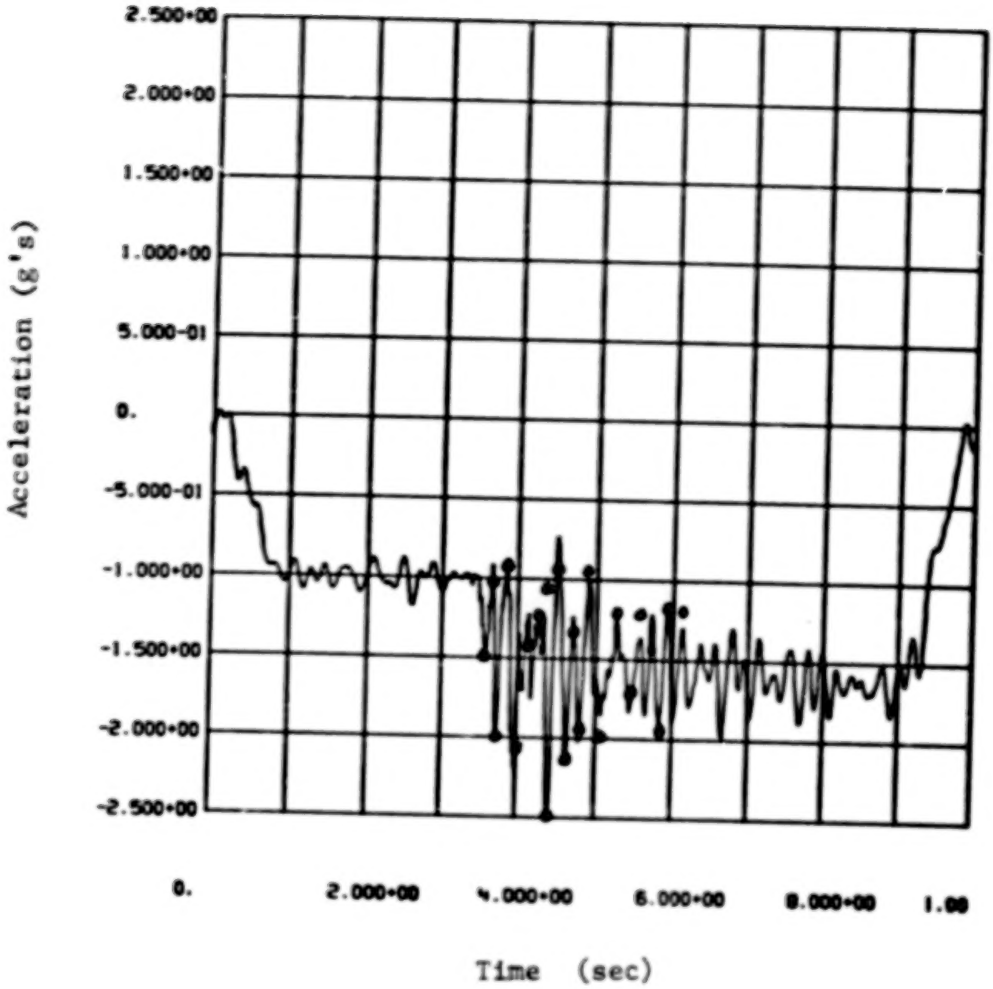

Figure 69. Response X Forward Attach Left Hand Side For Lift-Off.

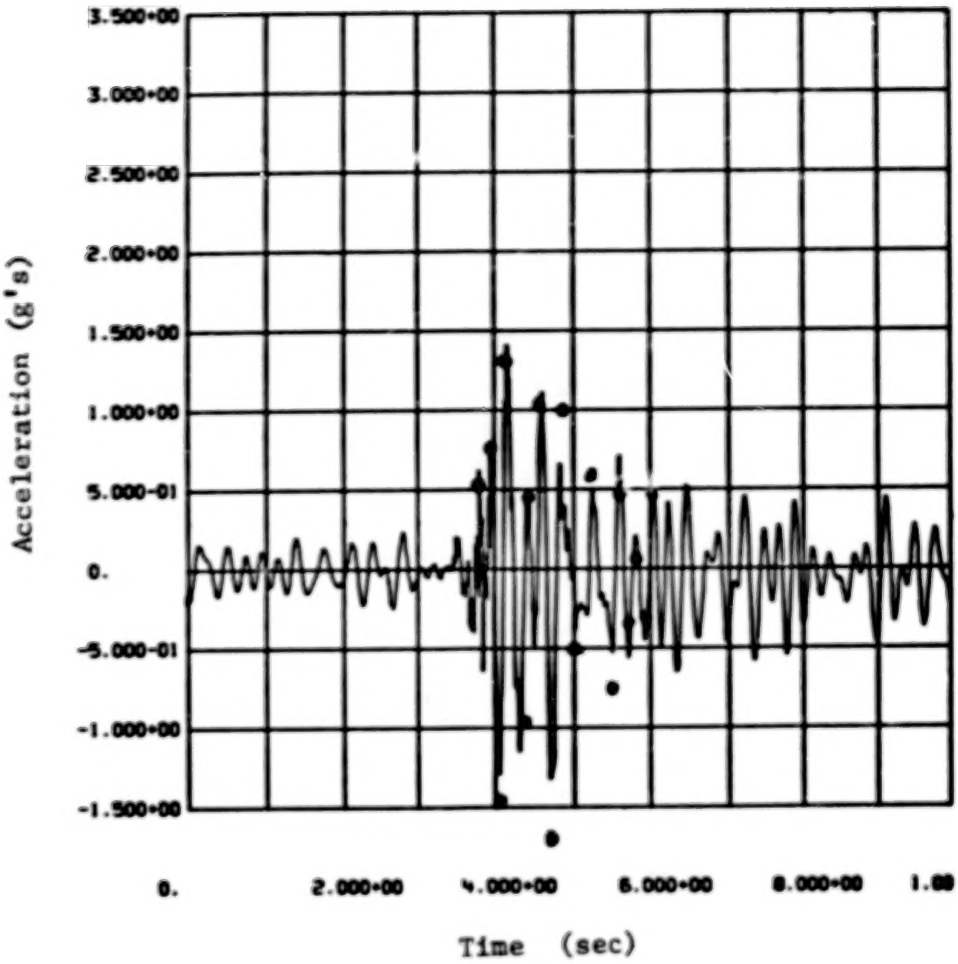

Figure 70. Response Z Forward Attach Left Hand Side For Lift-Oft.

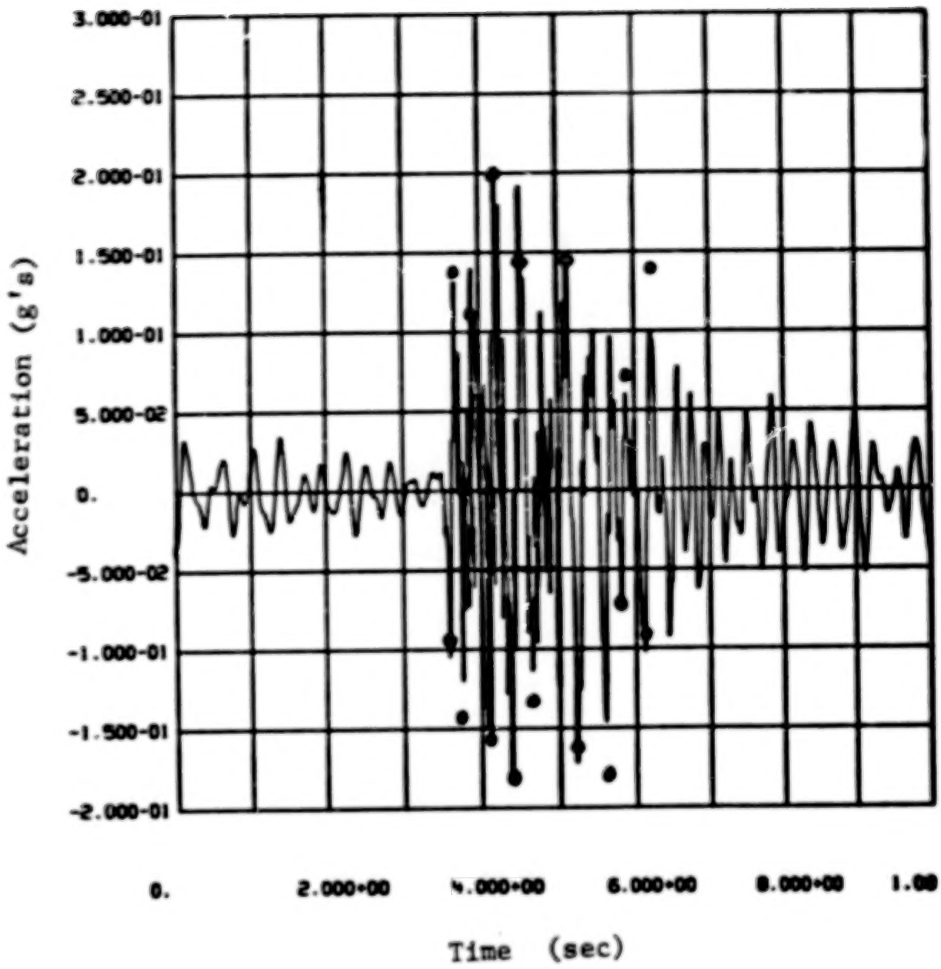

Figure 71. Response At KEEL For Lift-Off.

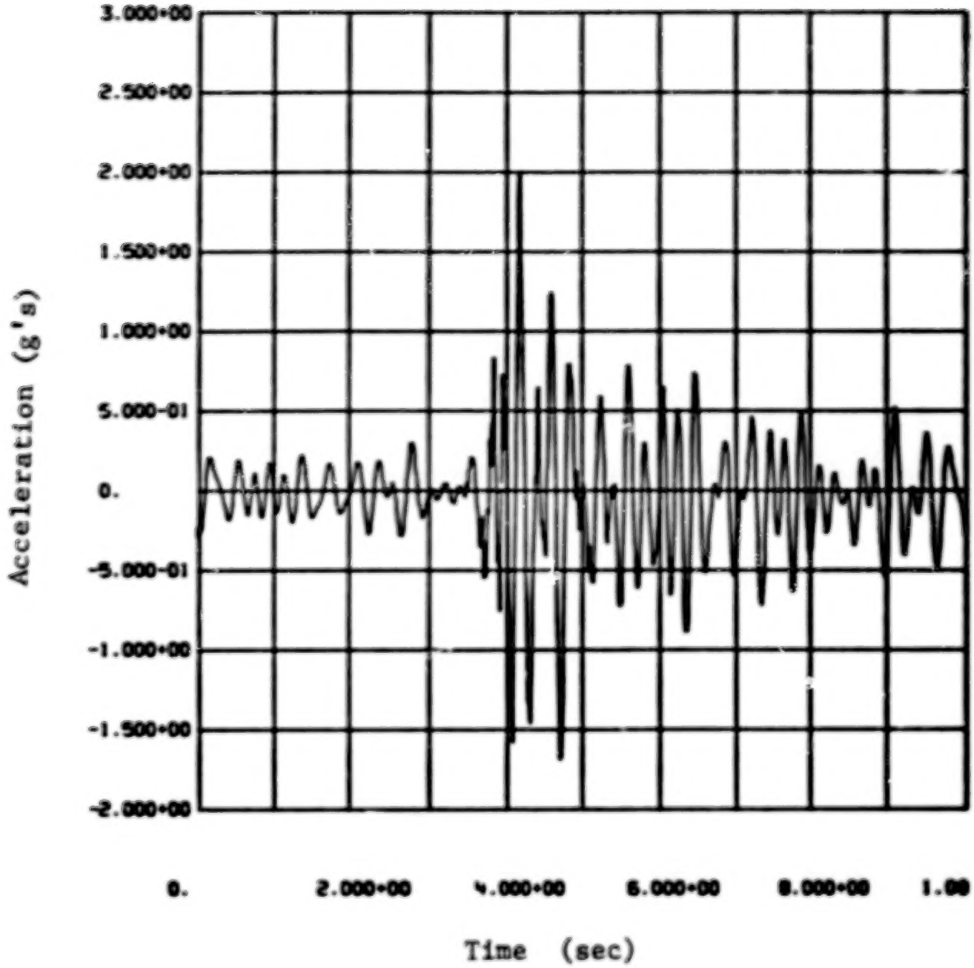

Figure 72. Response Z Aft For Lift-Off.

The correlation of the impedance technique results and the time domain solutions show generally good comparisons. Transcribing the peaks of the time domain accelerations to the inverse transform plots is agreed not to give conclusive comparison parameters. However, the peaks do appear to occur at the same points in time for both cases, indicating a minimal phase error. The largest discrepancy is shown in amplitude comparisons. Even in this area some of the amplitudes calculated with the impedance technique compare quite well. The best comparisons are shown in the longitudinal accelerations (Figures 67 and 69).

The final event analyzed with the impedance technique was a landing case. For this event 266 Fourier spectra were calculated for discrete forcing functions for the orbiter (representative loads and spectra can be found in Appendix B). The event can generally be described as a high angle of attack with symmetric landing conditions.

The problems encountered in analyzing the landing event resulted in defining analytical requirements for the use of the impedance technique for low frequency environment predictions. The analysis of this event pointed out the pitfalls of frequency resolution. The time histories of the forcing function for landing were of two different lengths. These are two basic external forces on the orbiter for landing (Appendix B): the landing gear strut loads; and the aerodynamic loads due to such things as ground effects, etc. The strut force time histories were 2.0 seconds in length and all other loads were only 0.8 seconds in length. Since the behavior of the aerodynamic loads were not known past 0.8 second and since it appeared that all oscillatory characteristics of the strut forces had diminished by 0.8 sec, the decision was made to

truncate the strut forces at 0.8 seconds for the analysis. The resulting sample rate based on the 512 data points used was 640 samples per second with a Nyquist frequency of 320 Hz.

The important thing of note, however, was that the frequency resolution for the 0.8 second signal was only 1.25 Hz. This resolution would be sufficient for describing characteristics of higher frequencies. However, the orbiter model contains low frequency bending modes at or around 5 Hz. With the assumed 1% modal damping ratio, this mode may have a bandwidth of 0.1 Hz. Thus, it is obvious that frequency descriptions of the input forces with a frequency resolution of 1.25 Hz could and did give erroneous answers.

The decision was made to discard the aerodynamic loads and perform the analysis with the full 2.0 second time history of the strut loads only. This decision of neglecting the aerodynamic forces was based on the general assumption that the aerodynamic forces contribute only a small part to the low frequency environment at the payload interface. The resulting resolution with only the strut forces becomes 0.5 Hz, which comes somewhat closer to the desired 0.1 Hz.

The results of the analysis with only the strut loads are shown in Figures 73 through 84. Here again the peaks from the time domain solution were transcribed to the plots for comparison.

These comparisons were not expected to be as good as the liftoff case generally because of the absence of aerodynamic loads. The worst comparisons are more evident in the "Z" direction acceleration, as expected, since this is the direction of the general aerodynamic forces. Also, the correlation seems to get worse from about 0.3 to 0.4 seconds on. This again is when the aerodynamic forces are the most active.

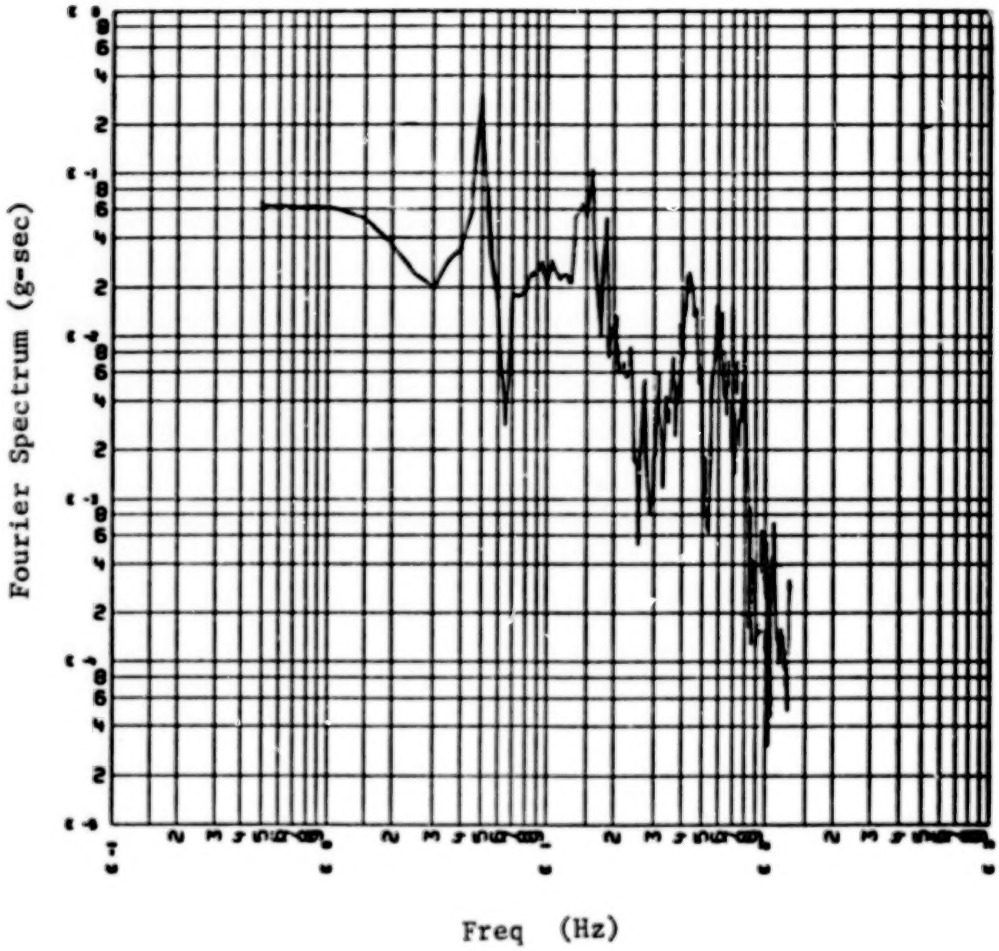

Figure 73. Fourier Spectrum of X Response At Forward Attach Point Right Hand Side For Landing Due To Strut Forces Only.

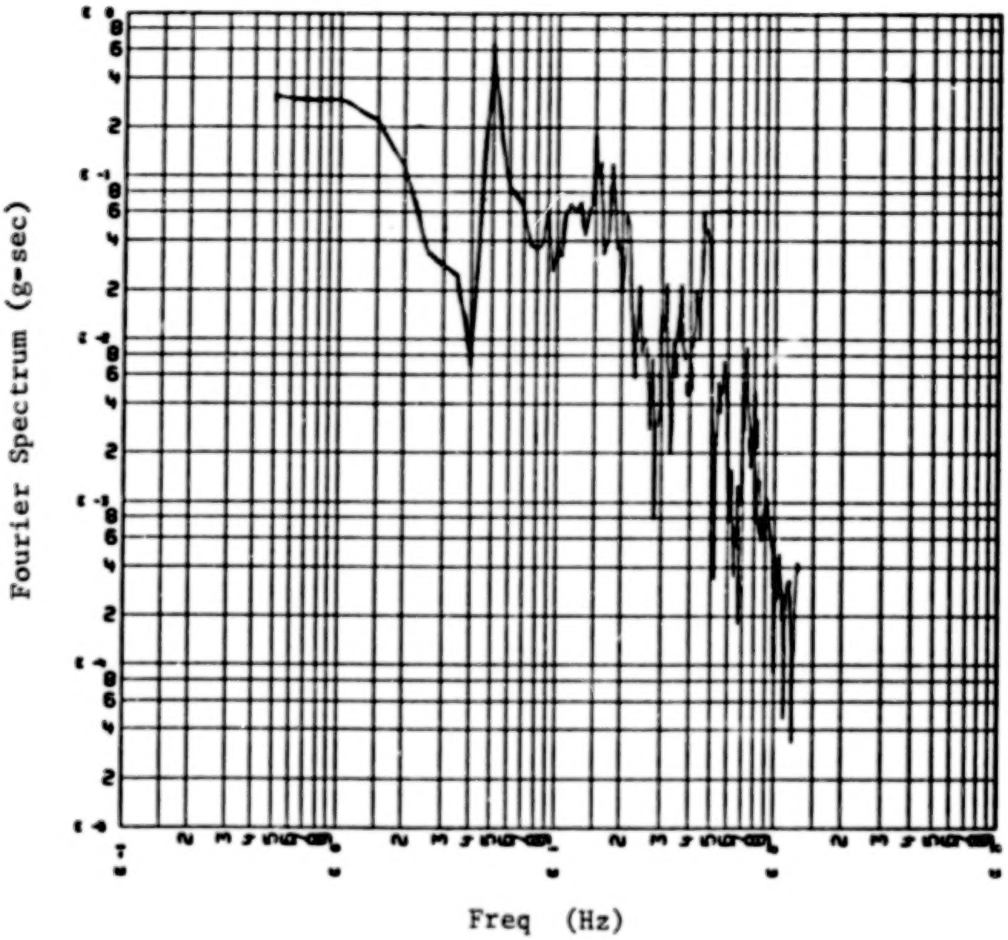

Figure 74. Fourier Spectrum of Z Response At Forward Attach Point Right Hand Side for Landing Due to Strut Forces Only.

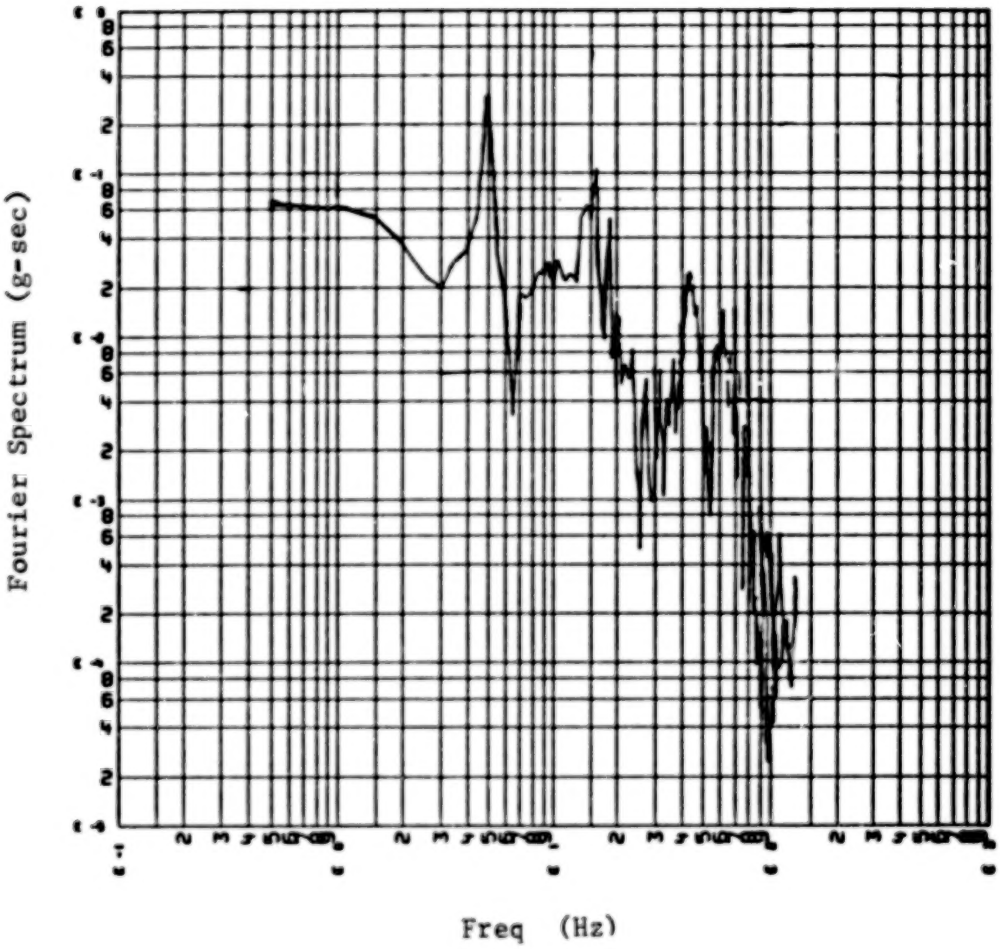

Figure 75. Fourier Spectrum of X Response At Forward Attach Point Left Hand Side For Landing Due To Strut Forces Only.

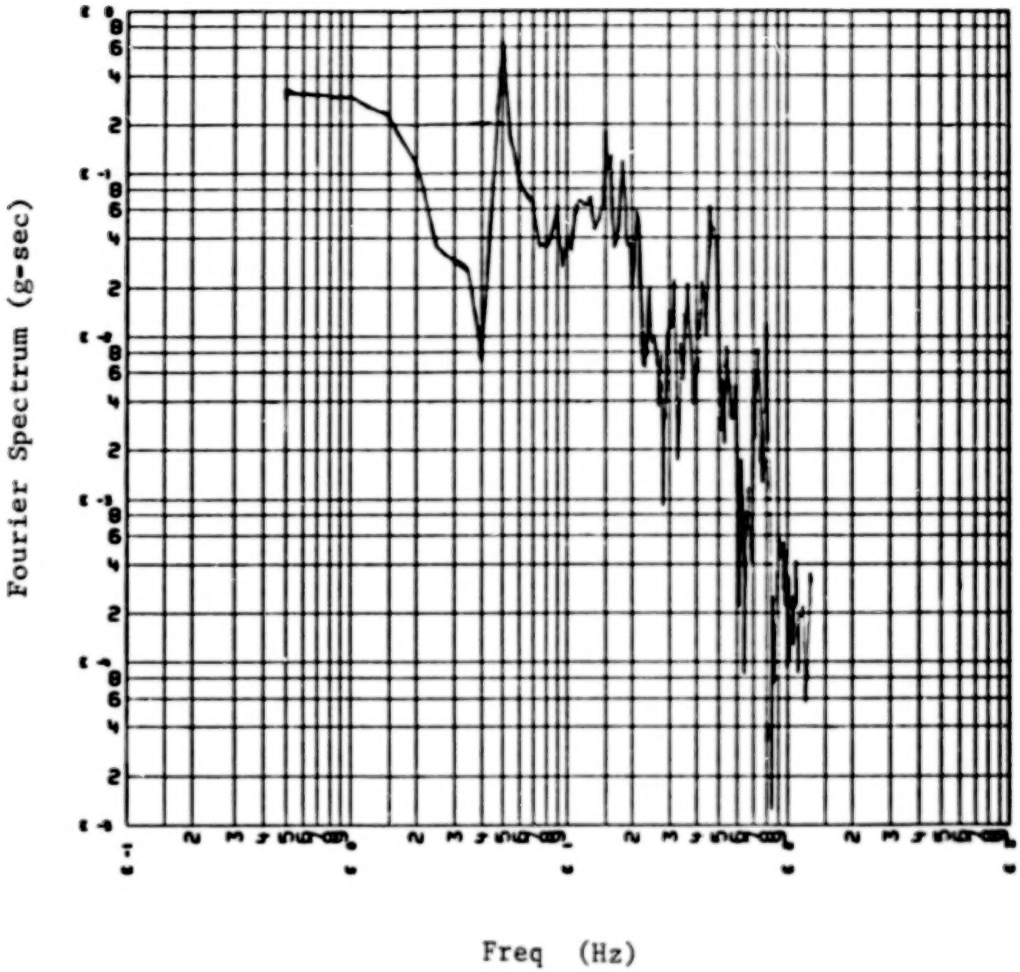

Figure 76. Fourier Spectrum of Z Response At Forward Attach Point Left Hand Side For Landing Due To Strut Forces Only.

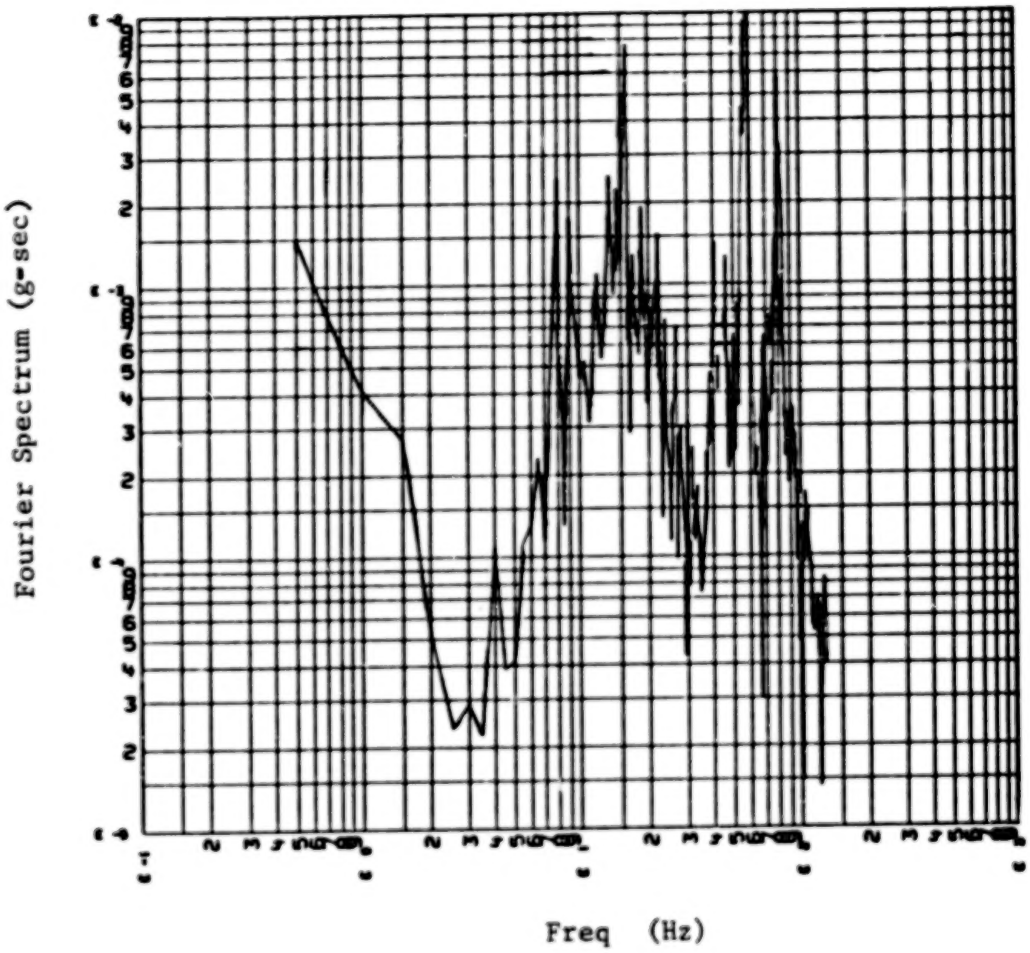

Figure 77. Fourier Spectrum of KEEL Response For Landing Due to Strut Forces Only.

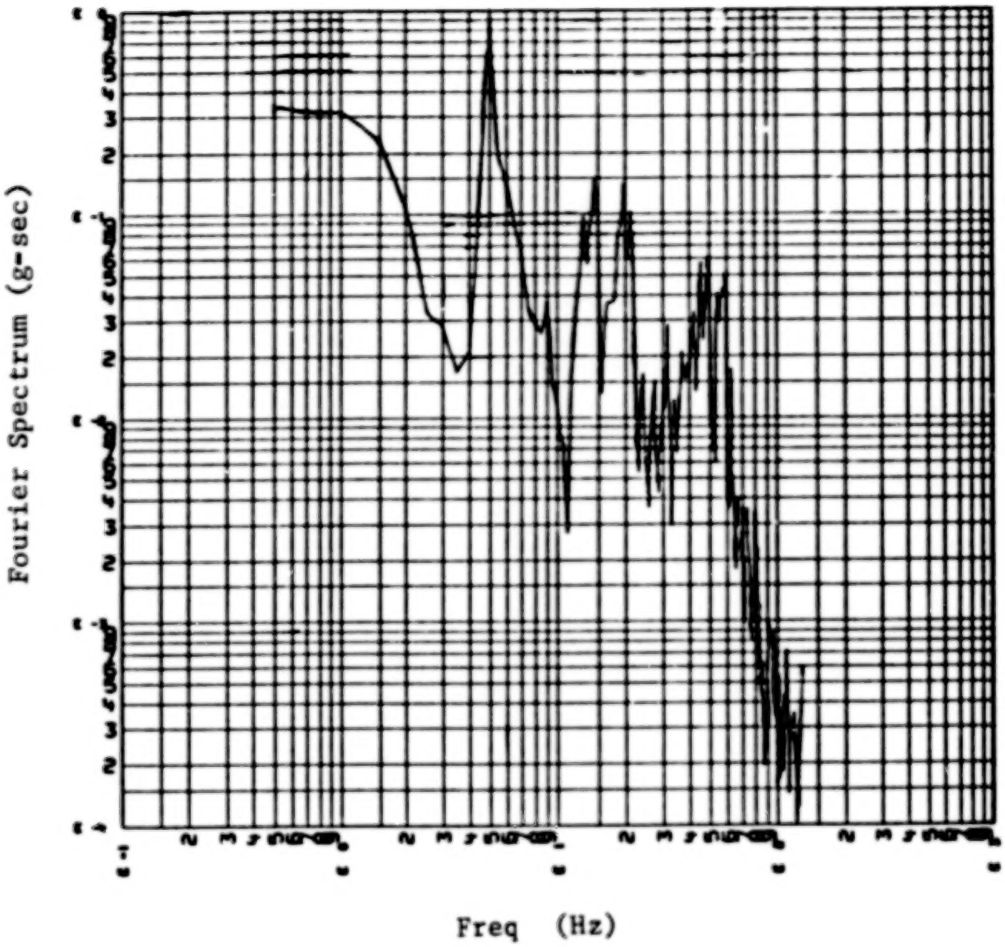

Figure 78. Fourier Spectrum of Aft Z Response For Landing Due to Strut Forces Only.

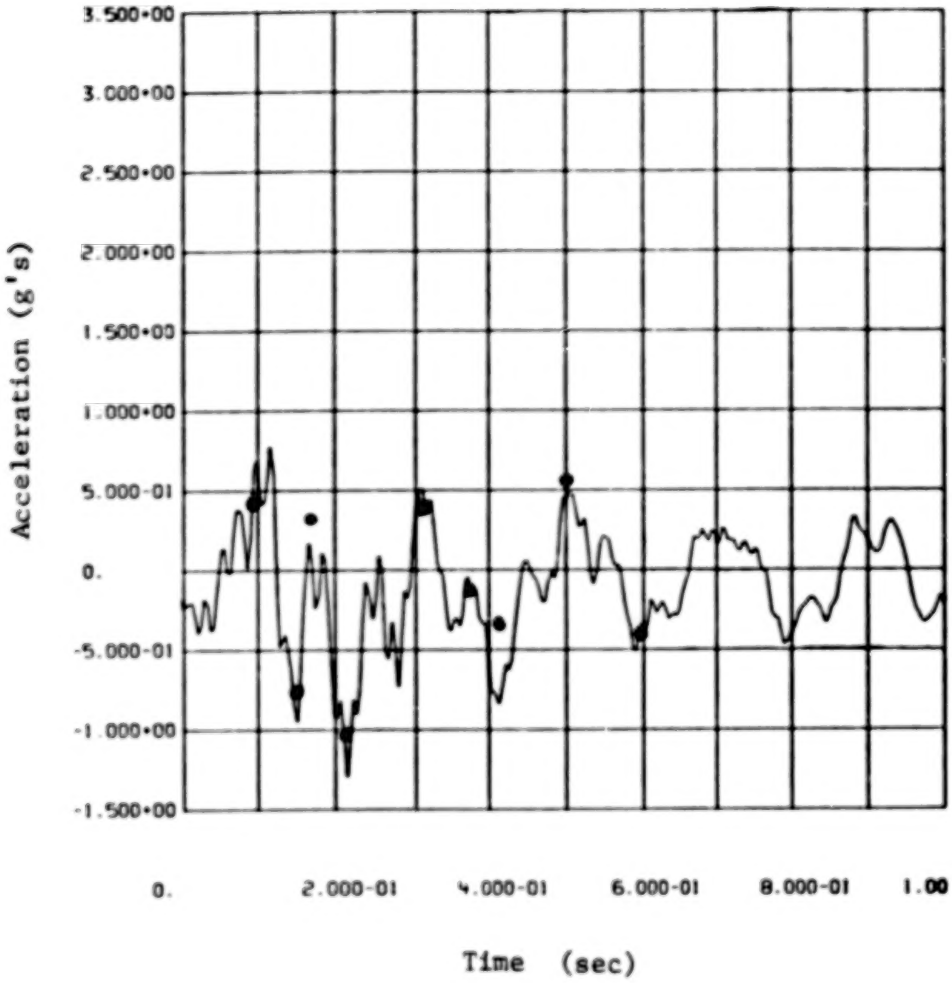

Figure 79. Response X Forward Attach Right Hand Side for Landing Due to Strut Forces Only.

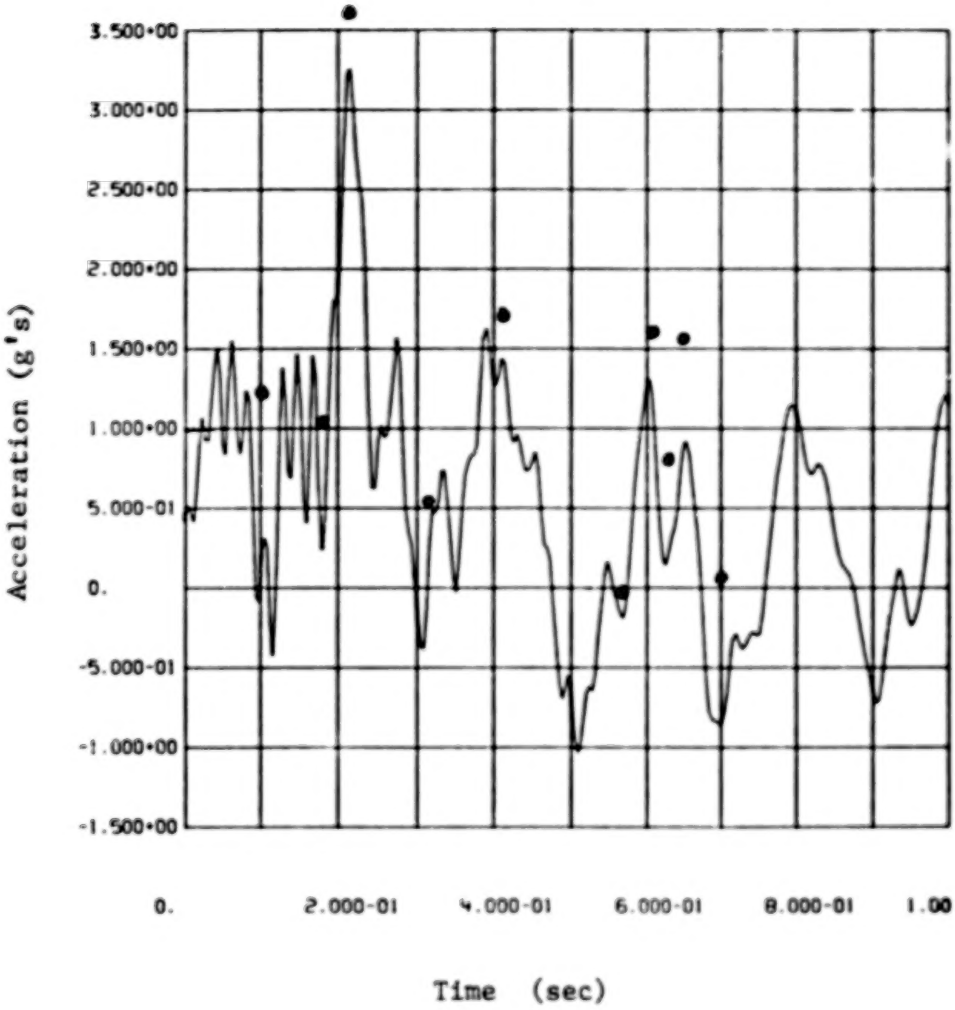

Figure 80. Response Z Forward Attach Right Hand Side For Landing Due To Strut Forces Only.

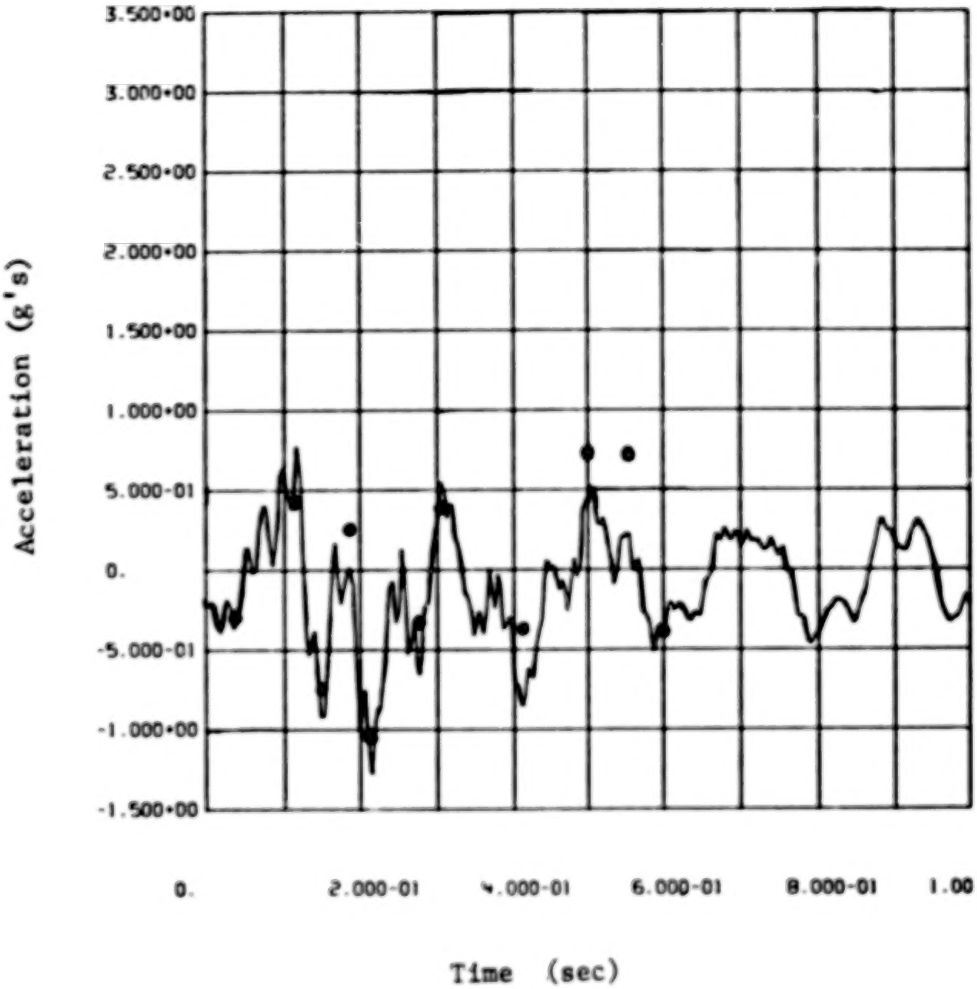

Figure 81. Response X Forward Attach Left Hand Side For Landing Due To Strut Forces Only.

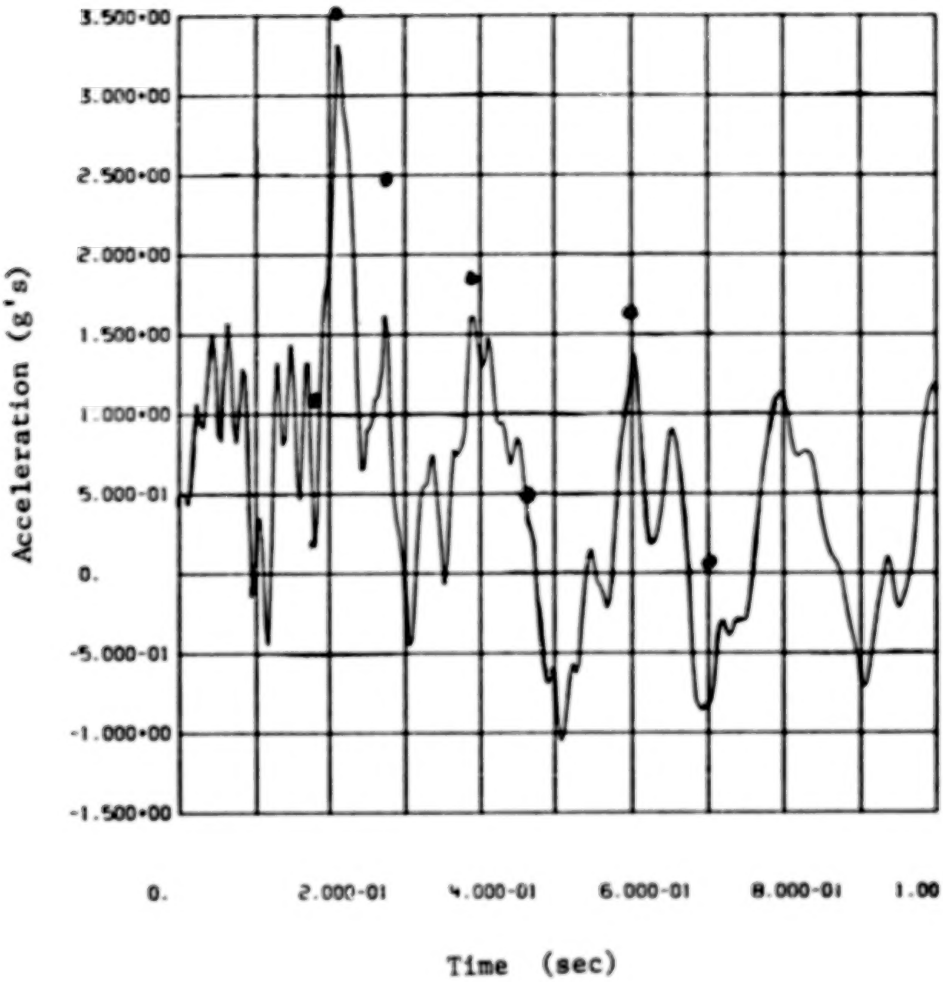

Figure 82. Response Z Forward Attach Left Hand Side for Landing Due to Strut Forces Only.

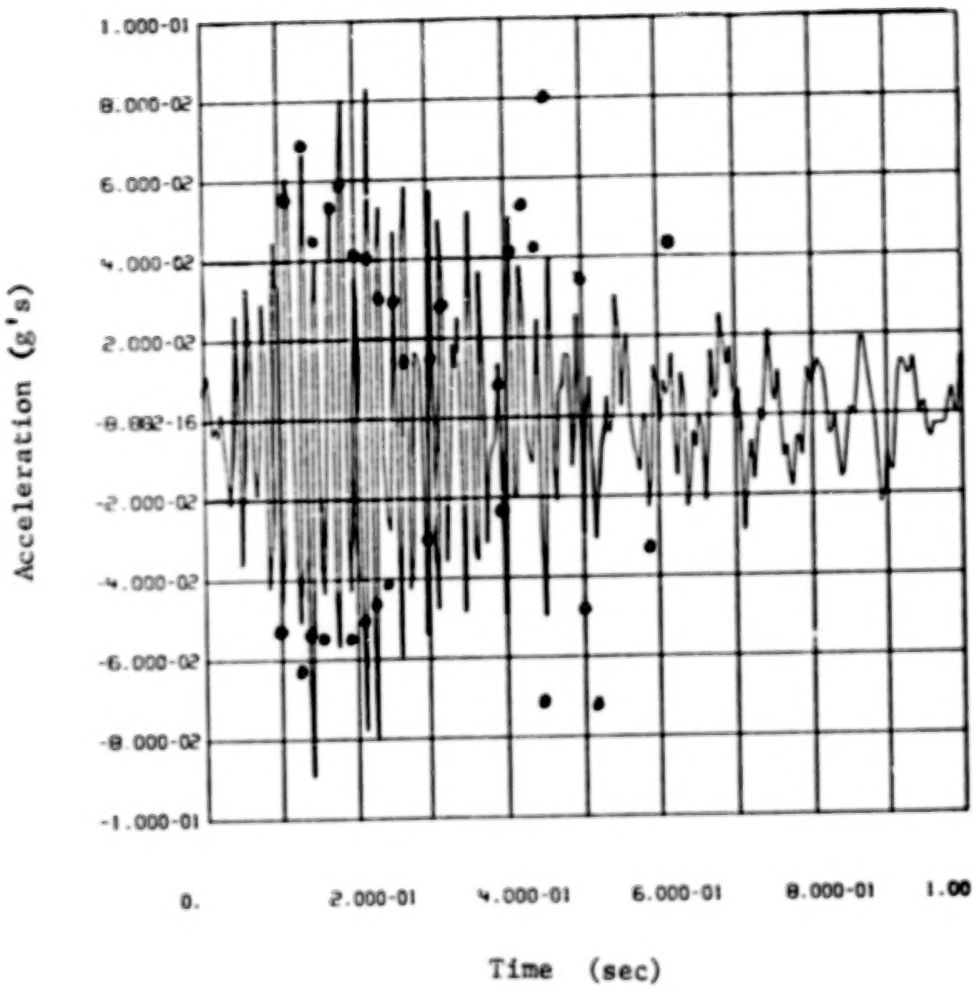

Figure 83. Response At KEEL For Landing Due To Strut Forces Only.

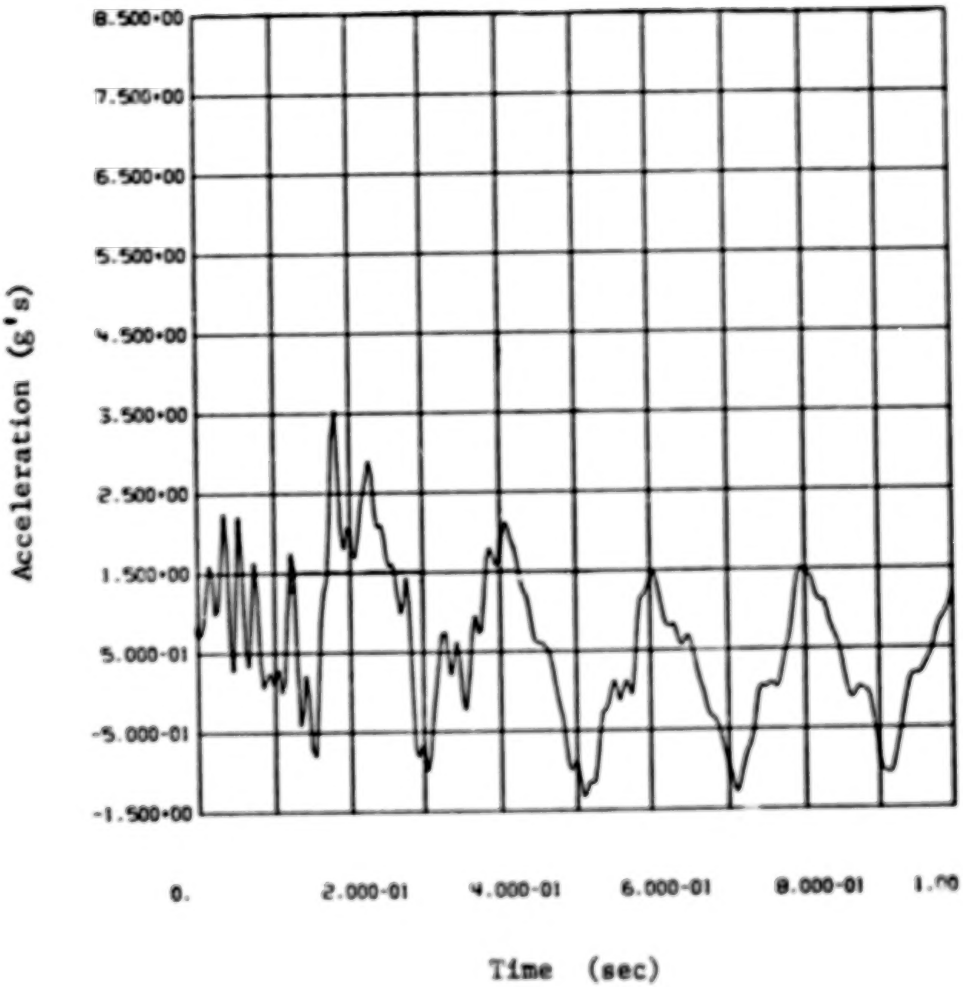

Figure 84. Response Z Aft For Landing Due To Strut Forces Only.

DISCUSSION OF RESULTS

The results of analyzing the Titan III-E data made some significant contributions to the evaluation of the impedance technique. The most important result was somewhat obvious from the beginning of the study. Extreme care has to be taken when recording and analyzing flight data for use in load prediction techniques. Transducers used for this phase of the study were not optimum for good predictions of the low frequency environments or for description of the vehicle transfer characteristics.

Besides pointing out data recording requirements, the Titan data analysis results consisted of new efforts in signal conditioning and spectral analysis. Efforts using ramps, windows, and FFTs refined the overall philosophy of the impedance technique. Even with these conditioning techniques, the discrepancies and extraneous signals on the flight data make evaluation of the spectral responses against the flight data quite difficult.

These results do, however, point out one important point: determining the low frequency environment from a pure spectral standpoint is quite difficult. As the results of the STS analysis show, additional information is gained from the history obtained from the inverse transforms.

The analysis of the liftoff event for the LDEF by far showed the best results. Even these results can be improved, however. As discussed in the previous sections, the differences in coupled damping versus the resulting damping of the impedance technique will never go away. The differences in the description of the equations of motion at the interface that depend on the boundary conditions will always cause that result. However,

with in-flight information of the true transfer characteristics, these problems could be minimized.

The set of analyses performed with the impedance technique for the liftoff case was done somewhat incorrectly to evaluate the impact on the results. The steady-state winds and gust loads (Appendix C) are represented by a dc level with a "1-cos" gust function. In normal time domain solutions the necessary initial conditions are derived to place the vehicle in equilibrium before the time domain solutions begin. In the spectral analysis of the impedance technique, these forces were applied at time zero, forcing the model to respond to an "imaginary" transient at time zero. Therefore, the responses shown will be changed when the winds are treated correctly.

The landing event analysis probably had the most meaningful results for the intent of this study. These results when compared to the time domain analysis predictions show not only the effects of the aerodynamic forces but more importantly give insight into the errors caused by inadequate frequency resolution.

Neither the liftoff or landing results shown should be used in any manner for design purposes for other payloads. The models used in these analyses are not necessarily the latest configurations. In addition, assumptions made in the impedance technique analysis, e.g., neglecting aerodynamic loads, cause the results to be somewhat unconservative.

Based on the results of all of the analyses performed, a limited evaluation of the technique for the use of future payloads can be made. It appears that this technique can be used for any coupled payload system in a very inexpensive manner. The ratioing of the acceleration from one flight to the next, as developed in the equation of motion and demonstrated

with the flight data from Titan, probably has the least use for STS payloads due to the variety of interface locations in the bay. It may be valuable, however, in evaluating design changes once one loads analysis is conducted.

The best use can be to achieve the removal of an integration role with a final set of eigensolutions. This can be achieved in much the same way as was done in this study. In the future, payload projects can obtain a data tape from the STS project that contains the best STS model and flight event cases. The payload designer can then perform the analysis to evaluate the design. This philosophy merely requires continual update of the STS dynamic characteristics and the latest flight data information.

Having calculated the predicted low frequency environment for a particular payload, the evaluation can be made for the necessity of a more extensive loads and/or response analysis for the payload based on the spectral content of the interface environment and the payload impedance. If there is concern about the design margin, the impedance technique programs should give some insight into the modal degrees of freedom of the generalized forces that are contributing most to the environment at that frequency bandwidth. This information should then be used to reduce the size of the models involved and again cut costs.

In summary, based on the results of this study, with reusable boosters and an environmental data bank, payload organizations can use the impedance technique to:

1. eliminate the necessity of integrated coupled analysis;
2. perform their own low cost environment predictions;

3. reduce analytical effort with spectral evaluation of coupled response; and
4. in the event more detailed analysis is necessary, reduce the size of the dynamic models.

CONCLUSIONS

An analytical technique has been derived that can be used to predict low frequency environments for payloads and at the same time lower the cost of the necessary analytical effort to calculate those predictions. Results of the analytical efforts during this study show that the frequency domain impedance technique can be used to define the interface accelerations, in both spectral and time history form, with sufficient accuracy to evaluate the payload design. By eliminating the necessity for final coupled eigensolutions, performing the response analysis in the frequency domain, and using the FFT to obtain Fourier spectra, the impedance technique reduces not only analytical integration effort, but computation costs as well.

Future payloads developers using common boosters will be able to perform their own environmental prediction analyses and therefore possibly impact the design earlier in the payload program. By evaluation of the low frequency environments versus the payloads dynamic characteristics and design margin, early decisions for more or less extensive analyses can be made.

Martin Marietta Corporation
Denver Division
Denver, Colorado 80201
June 26, 1978

APPENDIX A

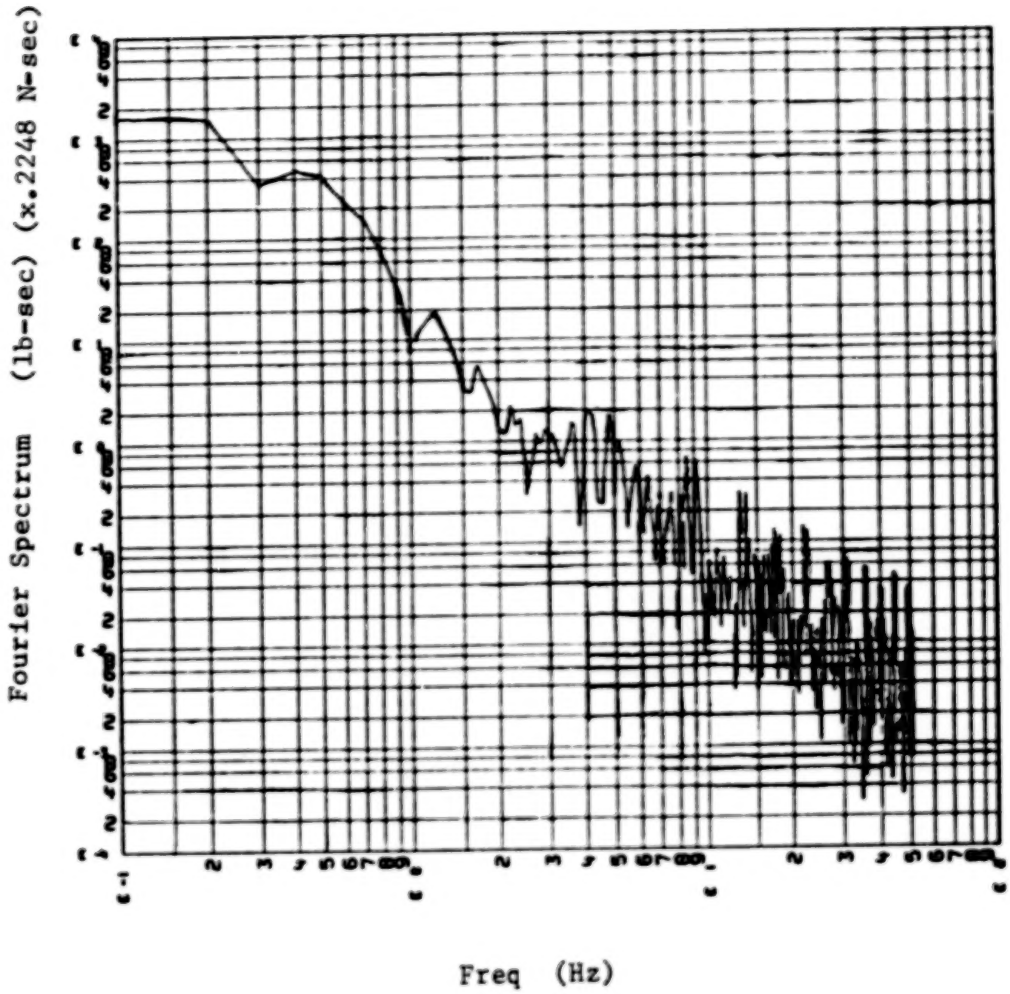

Figure A-1. Typical Fourier Spectrum of "1-cos" Wind Load Used For Lift-Off Analysis.

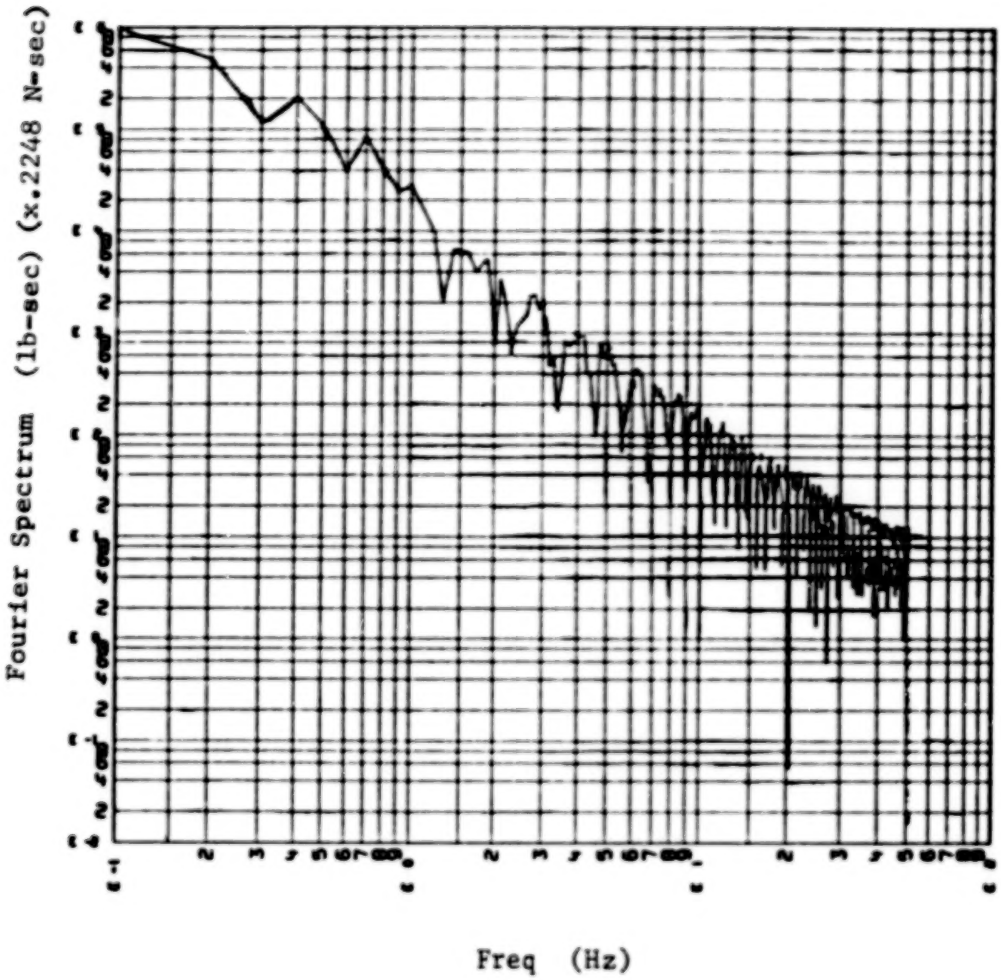

Figure A-2. Typical Fourier Spectrum of Orbiter Engine Thrust Used For Lift-Off Analysis.

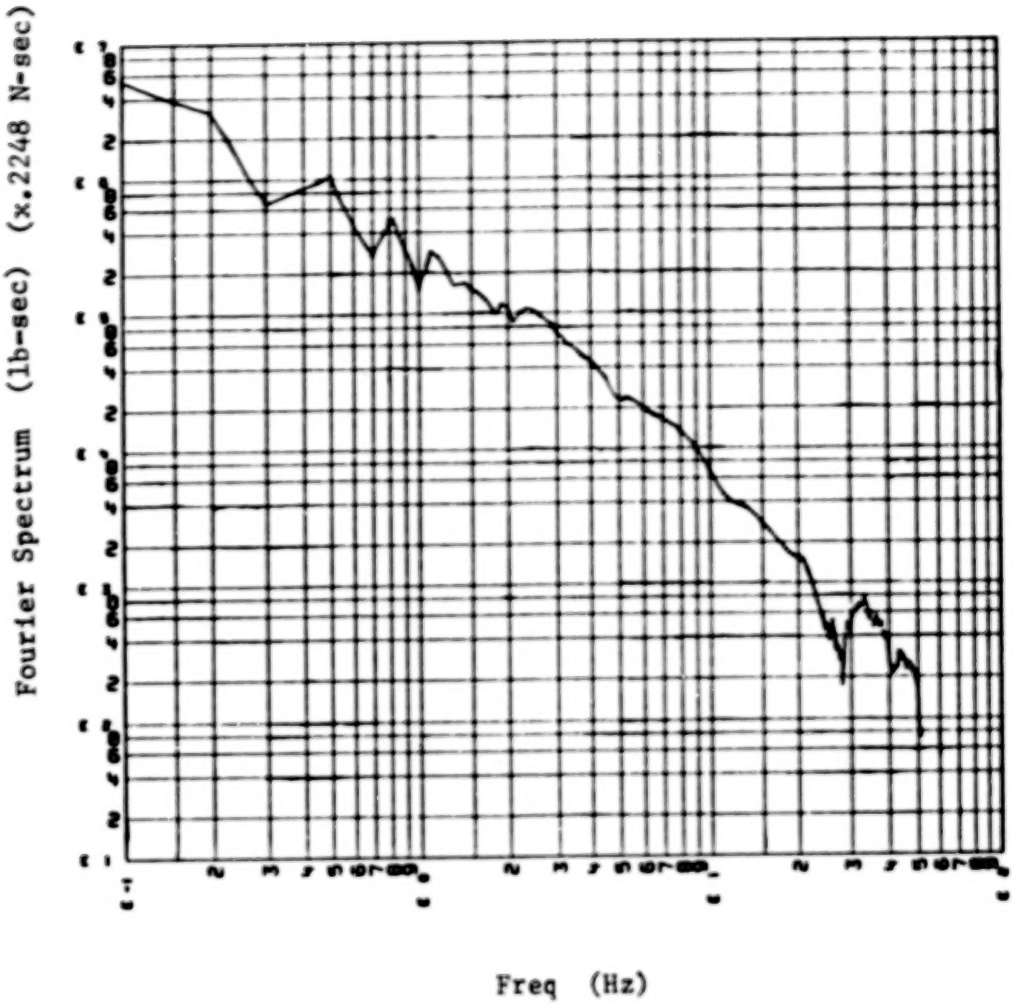

Figure A-3. Typical Fourier Spectrum of Restraining Loads Used For Lift-Off Analysis.

APPENDIX B

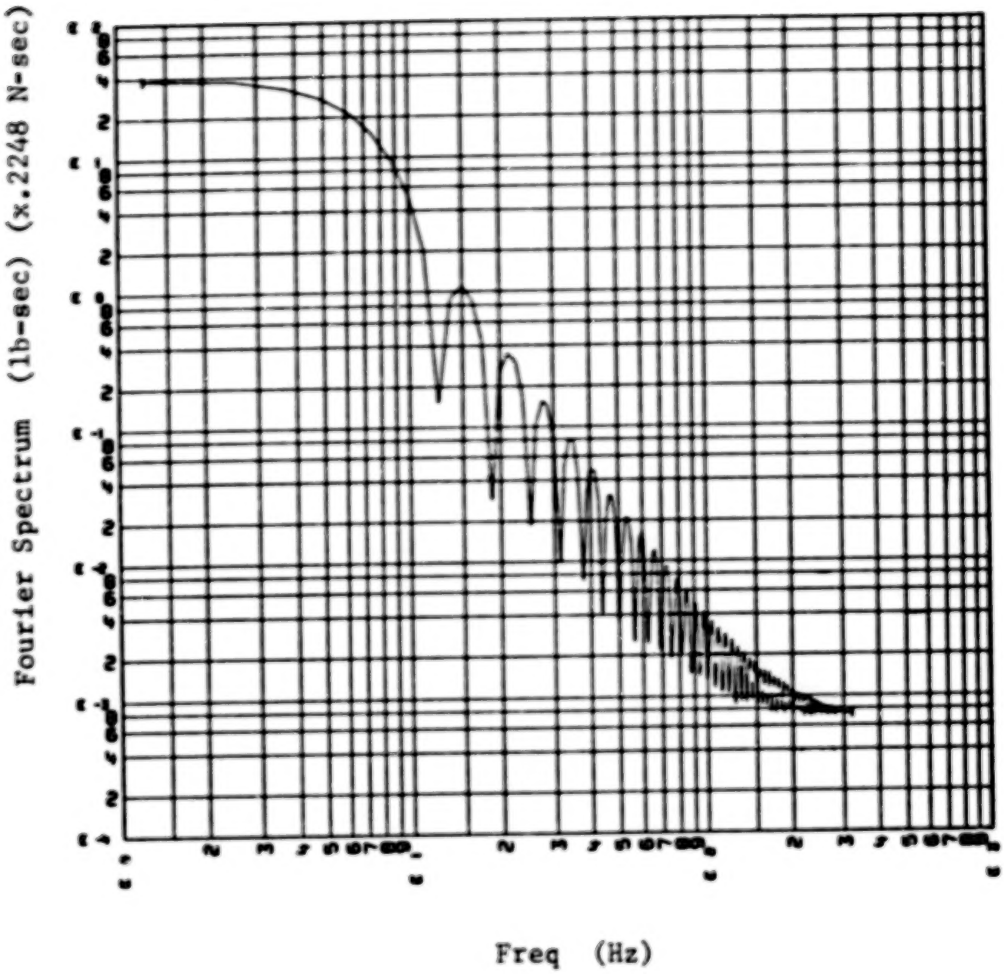

Figure B-1. Typical Fourier Spectrum of Aerodynamic Loads From 0.8 sec Time Histories Used For Landing Analysis.

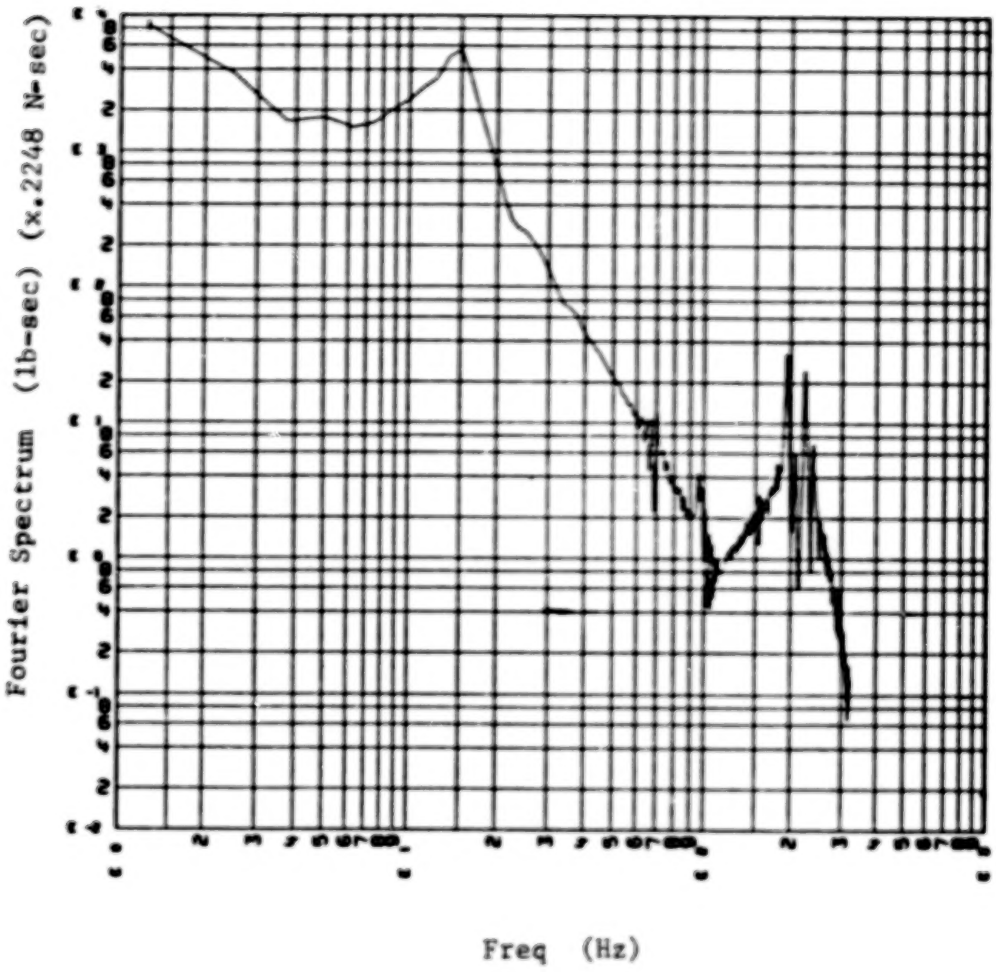

Figure B-2. Typical Fourier Spectrum of Strut Loads From 0.8 sec Time Histories Used For Landing Analysis.

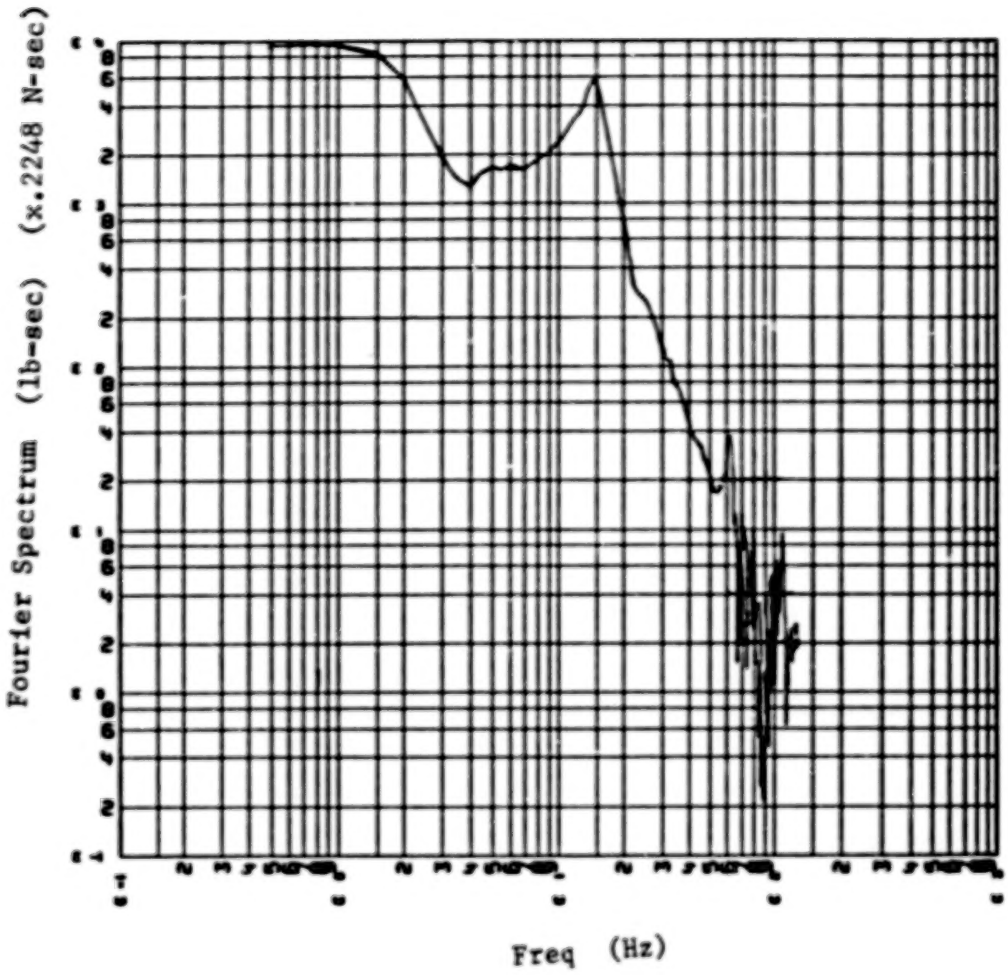

Figure B-3. Typical Fourier Spectrum of Strut Loads From 2.0 sec Time Histories Used for landing Analysis.

REFERENCES

1. Kana, D.D., and Unruk, J. F.: Prediction of Shuttle Vehicle Damping From Component Test Results, NAS8-27569.
2. Otnes, R. K., and Enochson, L.: Digital Time Series Analysis. Wiley - Interscience, New York, 1972.
3. Bendat, J. S., and Piersol, A. G.: Random Data Analysis and Measurement Procedures. Wiley - Interscience, New York, 1971.
4. Childers, D., and Durking A.: Digital Filtering and Signal Processing. West Publishing Col, New York, 1975.
5. Kachadourian, G.: A Summary of Spacecraft Loads Data From Four Titan Centaur Launch Vehicle Flights. NASA CR-2645.

1. Report No.	2. Government Accession No.	3. Recipient's Catalog No.
NASA CR-3143		

4. Title and Subtitle	5. Report Date
An Impedance Technique for Determining Low-Frequency Payload Environments	June 1979
	6. Performing Organization Code
7. Author(s) Kenneth R. Payne	8. Performing Organization Report No. MCR-78-581
9. Performing Organization Name and Address Martin Marietta Corporation P.O. Box 179 Denver, Colorado 80201	10. Work Unit No.
	11. Contract or Grant No. NAS1-14370
12. Sponsoring Agency Name and Address National Aeronautics and Space Administration Washington, D.C. 20546	13. Type of Report and Period Covered Contractor Report
	14. Sponsoring Agency Code

15. Supplementary Notes

Langley Technical Monitor: Brantley R. Hanks
Topical Report

16. Abstract

An impedance technique for calculating payload low-frequency environments was derived and demonstrated. The technique is based on frequency domain analysis and eliminates the necessity of final eigensolution for coupled payload/booster systems. A demonstration of the technique using Titan flight data and a low frequency environment prediction for a Shuttle payload are included. Criteria and philosophy for the technique for future payloads is discussed.

17. Key Words	18. Distribution Statement
Impedance Technique Spectral Analysis Low Frequency Environments Payload Loads	Unclassified - Unlimited Subject Category 39

19. Security Classif. (of this report)	20. Security Classif. (of this page)	21. No. of Pages	22. Price
UNCLASSIFIED	UNCLASSIFIED	143	$7.25

* For sale by the National Technical Information Service, Springfield, Virginia 22161

NASA-Langley, 1979

END

May 29, 1981